POLITECNICO

MILANO 1863

SCUOLA DI INGEGNERIA INDUSTRIALE
E DELL'INFORMAZIONE

Synthesis and Characterization of Manganese Oxides Thin Films

TESI DI LAUREA MAGISTRALE IN
MATERIALS ENGINEERING AND NANOTECHNOLOGY -
INGEGNERIA DEI MATERIALI E DELLE NANOTECNOLOGIE

Author: **Arianna Monforte Ferrario**

Student ID: 966317
Advisor: Prof. Andrea Li Bassi
Co-advisors: Dr. Andrea Macrelli
Academic Year: 2021-22

Abstract

Extensively studied for more than a century for their numerous applications in many different fields, manganese oxides recently became the subject of intense research due to their potential use in energy storage devices. Naturally abundance, low cost and environmental friendliness make them promising materials for the developments of capacitors and supercapacitors, catalysts and "next-generation" battery technologies but some critical aspects still need to be addressed. A plethora of different MnO_x phases arises from the multiple oxidation states of manganese and their proper characterization is still an open challenge. Moreover, the lack of a clear understanding of the fundamental machanisms that governs the rather complex electrochemical behavior of these materials, ruled by the interplay between the nanoscale morphology, the different phases and the different oxidation states, is a major obstacle for their widespread use. Therefore, many efforts have been devoted to the development of new methodologies for the synthesis of pure MnO_x phases and the study of their electrochemical properties.

In my work, thin films of MnO_x with various oxidation states (MnO_2, Mn_2O_3, and Mn_3O_4) were produced by Pulsed Laser Deposition (PLD) at room temperature and subsequent post-deposition annealing treatments to obtain a decoupled control of morphology and phase of the MnO_x films. Deposition conditions were optimized in oxygen atmosphere at different oxygen partial pressures ($1-100$ Pa). The morphology of the films was characterized by Scanning Electron Microscopy (SEM), while for structural and phase characterization, Raman Spectroscopy, Energy Dispersive X-Ray Spectroscopy (EDX), and X-Ray Diffraction (XRD) were employed. High oxygen pressures lead to the formation of nanoporous films characterized by a tree-like structure usually referred to as a "nanoforest". A detailed study on the effect of laser wavelength and power was also conducted in order to justify the reliability of subsequent Raman results. Raman Spectroscopy demonstrated that via PLD depositions two different MnO_x phases can be obtained: amorphous MnO_2 and nanocrystalline Mn_3O_4. To investigate the effect on morphology and whether other phases could be obtained, post-deposition thermal treatments were performed on the samples. I studied how the temperature and atmosphere of the annealing affect both the morphology and phase of the films, and I found that higher temperatures increases the

crystal size and improve the film crystalline quality. The annealing atmosphere was discovered to have more influence on the MnO_x phase of the films rather then their morphology. In particular, two different phases can be obtained by annealing in air and vacuum at the same temperature (i.e., 500°C): Mn_2O_3 from the annealing in air and Mn_3O_4 from the annealing in vacuum. Moreover, I verified that the minimum temperature to obtain the Mn_2O_3 in air is 500°C. Phase assignment was also confirmed by EDX analysis and XRD measurements, which provided additional information about crystallinity and long-range order. In order to obtain also a characterization of the optical properties of the material, some depositions were made on a glass substrate. While a basic characterization could be obtained for the as-deposited samples, the annealed samples were not analyzed since I found that the glass substrate can have some influence in determining the resulting MnO_x phase and this effect is somehow activated by temperature.

The last part of my work was devoted to perform some preliminary investigation on the electrochemical behavior of MnO_x materials using thin films as model systems. Cyclic voltammetry was used to test some selected samples in two different acqueous electrolytes: Na_2SO_4 0.2 M (NS electrolyte) and $ZnSO_4$ 2 M + $MnSO_4$ 0.1 M (ZMS electrolyte). The first was used to characterize the basic electrochemical behavior of the films, and the second to simulate a more realistic situation of a zinc-ion battery, for which MnO_x materials are commonly reported cathodes. Some interesting results were obtained but further extensive studies are needed to draw comprehensive conclusions on the electrochemical behavior of MnO_x materials.

To conclude, the combination of room-temperature PLD and subsequent thermal treatments proved to be a suitable method for the synthesis of different pure MnO_x phases in the form of thin films, with different nanoscale morphologies. The produced films can be used both for the characterization of the material itself and for electrochemical application developments and research. Future developments of this research may focus on the characterization of the material with complementary techniques (e.g., XPS, and FTIR), on the investigation of the effect of the substrate and the temperature during deposition, on the production of films using different deposition parameters, or on the electrochemical side where only preliminary tests have been completed.

Keywords: MnO_x, manganese oxides, PLD, Raman Spectroscopy, Thin-films, ZIB cathodes

Abstract in lingua italiana

Ampiamente studiati per più di un secolo per le loro numerose applicazioni in diversi ambiti, gli ossidi di manganese sono recentemente diventati oggetto di intense ricerche a casua del loro potenziale utilizzo in dispositivi di accumulo di energia. La loro naturale abbondanza, il basso costo e la compatibilità ambientale li rendono materiali promettenti per lo sviluppo di condensatori e supercondensatori, catalizzatori e batterie di "nuova generazione", ma alcuni aspetti critici devono ancora essere affrontati. Una pletora di diverse fasi di MnO_x deriva dai molteplici stati di ossidazione del manganese e la loro corretta caratterizzazione è tutt'ora una sfida aperta. Inoltre, la mancanza di una chiara comprensione del meccanismo fondamentale che governa il comportamento elettrochimico piuttosto complesso di questi materiali, caratterizzato dall'interazione tra le diverse fasi e i diversi stati di ossidazione del manganese, costituisce un grosso ostacolo alla loro diffusione. Pertanto, molteplici sforzi sono stati dedicati allo sviluppo di nuove metodologie per la sintesi di fasi pure di MnO_x e allo studio delle loro proprietà elettrochimiche.

Nel mio lavoro, sono stati prodotti film sottili di MnO_x con diversi stati di ossidazione (MnO_2, Mn_2O_3, e Mn_3O_4) mediante Deposizione Laser Pulsata (PLD) a temperatura ambiente, e successivi trattamenti termici al fine di ottenere un controllo disaccopppiato della morfologia e della fase dei film. Le condizioni di deposizione sono state ottimizzate in atmosfera di ossigeno a diversi pressioni parziali ($1-100$ Pa). La morfologia dei film è stata caratterizzata mediante Microscopia Elettronica a Scansione (SEM), mentre per la caratterizzazione strutturale e di fase, sono state utilizzate tecniche di Spettroscopia Raman, Spettroscopia di Assorbimento di Energia di Raggi-X (EDX), e la Diffrazione dei Raggi-X (RDX). Pressioni elevate di ossigeno portano alla formazione di film nanoporosi caratterizzati da una struttura ad albero comunemente chiamata "nanoforesta". Un'attenta analisi dell'effetto della lunghezza d'onda e della potenza del laser è stata condotta per giustificare l'affidabilità dei risultati successivi. La Spettroscopia Raman ha dimostrato che le deposizioni PLD possono portare alla formazione di due diverse fasi di MnO_x: MnO_2 amorfo e Mn_3O_4 nanocristallino. Trattamenti termici post-deposizione sono stati eseguiti sui campioni con lo scopo di indagarne l'effetto sulla morfologia dei film e di verificare qualora fosse possibile otenere altre fasi di MnO_x. Ho studiato come la temperatura e

l'atmosfera del trattamento termico influenzano sia la morfologia che la fase dei film, e ho scoperto che temperature più elevate aumentano la dimensione dei cristalli e migliorano la qualità cristallina. Ho inoltre scoperto che l'atmosfera del trattamento termico ha un maggiore effetto sulla fase dei film piuttosto che sulla loro morfologia. Infatti, in seguito ai trattamenti termici in aria e in vuoto, condotto alla medesima temperatura (i.e., 500°C) si ottengono due fasi differenti di MnO_x: Mn_2O_3 dal trattamento in aria e Mn_3O_4 dal trattamento in vuoto. Inoltre, ho verificato che la temperatura minima per ottenere Mn_2O_3 dal trattamento in aria è di 500°C. L'assegnazione delle fasi è stata confermata anche dall'analisi EDX e dalle misurazioni XRD, che hanno fornito ulteriori informazioni sulla cristallinità e sull'ordine a lungo raggio. Al fine di ottenere anche una caratterizzazione delle proprietà ottiche del materiale, sono state effettuate delle deposizioni su substrato di vetro. Mentre è stato possibile ottenere una caratterizzazione di base per i campioni "as-deposited", i campioni sottoposti a trattamento termico non sono stati analizzati poiché è stato scoperto che il substrato di vetro può avere una certa influenza nel determinare la fase MnO_x risultante e questo effetto è in qualche modo attivato dalla temperatura. L'ultima parte del mio lavoro intende svolgere alcune indagini preliminari sul comportamento elettrochimico degli ossidi di manganese. La voltammetria ciclica (CV) è stata utilizzata per testare alcuni campioni selezionati in due diversi elettroliti acquosi: Na_2SO_4 0.2 M (elettrolita NS) e $ZnSO_4$ 2 M + $MnSO_4$ 0.1 M (elettrolita ZMS). Il primo utilizzato per caratterizzare il comportamento elettrochimico proprio dei film, e il secondo per simulare una situazione più realistica di una batteria allo zinco, per la quale gli MnO_x sono comunemente riportati come catodi. Alcuni interessanti risultati sono stati ottenuti, tuttavia ulteriori studi approfonditi sono necessari per trarre conclusioni esaustive sul comportamento elettrochimico di questi materiali.

In conclusione, la combinazione di PLD a temperatura ambiente e successivi trattamenti termici si è dimostrata un metodo adatto per la sintesi di diverse fasi pure di MnO_x sotto forma di film sottili. I film prodotti possono essere utilizzati sia per la caratterizzazione del materiale stesso che per sviluppi e ricerche elettrochimiche. Gli sviluppi futuri di questa ricerca possono concentrarsi sulla caratterizzazione del materiale con tecniche complementari (ad es. XPS e FTIR), sullo studio dell'effetto del substrato e della temperatura durante la deposizione, sulla produzione di film utilizzando diversi parametri di deposizione, o sul lato elettrochimico dove sono stati completati solamente test preliminari.

Parole chiave: MnO_x, ossidi di manganese, PLD, Spettroscopia Raman, Film sottili, catodi per ZIB

Contents

Introduction

Manganese oxides (MnO_x) have been used for thousands of years for various applications ranging from pigments to environmental applications and steelmaking [1]. Recently they have become very attractive for other technological applications such as electrochemical capacitors and supercapacitors [2, 3], electrocatalysts [4–6] and various types of batteries [6–14]. In particular, MnO_x are promising cathode materials for the "beyond lithium-ion" battery technologies among which zinc-ion batteries (ZIBs) are the most attractive [8]. However, even though manganese oxides materials are naturally abundant, low cost and environmental friendly but they also present numerous critical aspects. The many different oxidation states of manganese ($+2$, $+3$, $+4$, $+6$, and $+7$) give rise to the formation of many different MnO_x phases which are not always easy to be characterized and to be controlled during synthesis. Therefore, the synthesis of pure MnO_x phases constitutes a particularly attractive research area. Moreover, this complexity is reflected in the electrochemical behavior of these materials which involves numerous complex phase transitions and ranges over all the oxidation states of manganese. This thesis is focused on the synthesis and characterization of manganese oxides thin films by pulsed laser deposition (PLD) combined with post-annealing treatments in order to obtain a decoupled control on the nanoscale morphology and phase of the films. Moreover, the production of thin films may be interesting for applications in the field of thin film microbatteries. This physical vapour deposition (PVD) technique was already implemented in many other literature works [15–26] for depositions of MnO_x films at high temperatures (i.e., $\geq 300°C$). The innovative aspects of this thesis project consist in a detailed study of the deposition of MnO_x thin films at room temperature and of the effect of the post-deposition annealing treatments in different environments (air or vacuum). Moreover, the characterization of the films phase is obtained through detailed Raman spectroscopy analysis and particular attention is also paid to the morphology of the PLD-grown films which is usually hardly mentioned in previous literature and may be relevant for MnO_x application in the battery field. At the end of the work, early electrochemical tests are performed on the films in two different aqueous electrolytes in order to evaluate their electrochemical response.

The present work will be organised in six chapters as follows:

1. *Chapter 1* provides a general overview of manganese oxides materials. In particular, the main structures of natural MnO_x are described and the complex situation regarding their phase characterization is presented. The following sections are devoted to the applications of manganese oxide with particular attention to the battery field. The last section of this chapter presents the objectives of the thesis.

2. *Chapter 2* describes the experimental techniques, starting from the pulsed laser deposition (PLD) used for the synthesis of the films and the ovens used for the post-deposition annealing treatments. The following sections are devoted to the description of the characterization techniques: Scanning Electron Microscope (SEM), Energy Dispersive X-ray Spectroscopy (EDXS), X-ray diffraction (XRD), Raman spectroscopy and UV/Vis Spectroscopy, used to study the morphology, chemical composition, structural/vibrational and optical properties of the films. The last section presents the Ciclic Voltammetry technique used for preliminary electrochemical tests.

3. *Chapter 3* describes the synthesis of MnO_x thin films. The optimization of the PLD parameters is presented in the first section. Then, investigation on the effect of the O_2 pressure on the morphology of the as-deposited MnO_x films is performed by SEM analysis. In the following, phase characterization of as-deposited films is achieved by means of Raman, EDX and XRD analysis. In the last section, also a simple optical characterization of as-deposited MnO_x films is presented.

4. *Chapter 4* describes the effect of the post-deposition annealing treatments on the morphology and phase of the films. After the description of the optimization of the annealing parameters, the morphology of the films is investigated by SEM analysis. The following sections are devoted to the phase characterization of the films by means of Raman, EDX and XRD analysis. The peculiar case of the annealing conducted on glass substrate is also presented before a summary of the final results.

5. *Chapter 5* describes the preliminary electrochemical tests performed on selected films. In the first part a brief introduction on the current research situation on the electrochemistry of MnO_x is presented. The subsequent section is devoted to the description of the electrochemical cell used for the tests. Then, the electrochemical response of the films is investigated by means of Cyclic Voltammetry (CV) in two different electrolytes. The characterization of the films after the CV tests is performed by means of Raman spectroscopy and SEM analysis.

6. *Chapter 6* concludes the thesis with a summary of the results obtained and a discussion on the future perspectives.

1 | Overview of Manganese oxides

Manganese (Mn) is the 10th most abundant element in the Earth's crust and it is the most common heavy metal second only to iron (Fe) [1]. Mn is a redox-sensitive element and exist in several oxidation states, such as +2, +3, +4, +6, and +7. Of these Mn oxidation states, only Mn^{4+}, together with Mn^{3+} and Mn^{2+}, are present in nature and forming minerals in the form of MnO_2, Mn_2O_3 and Mn_3O_4 [27]. As a result, more than 30 Mn oxide/hydroxide minerals can be found in a variety of geological systems and are nearly ubiquitous in soils and sediments. Most Mn oxide minerals are brown-black and typically occur as fine-grained mixtures of different Mn phases plus additional minerals such as carbonates, silicates, and Fe oxides/hydroxides.[1, 28].

1.1. Manganese oxides (MnOx)

Manganese oxides and hydroxides (hereafter MnO_x) are natural cryptocrystalline nano-materials characterized by extreme short-range order and long-range disorder [28]. The basic building block for most MnO_x atomic structures (expecially MnO_2) is the MnO_6 octahedron which can give rise to a large variety of different structural arrangements by sharing edges and/or corners. These structures can be grouped into two categories [1]:

1. *Tunnel structures*. The tunnel MnO_x are constructed of single, double, or triple chains of edge-sharing MnO_6 octahedra, and the chains share corners with each other to produce frameworks that have tunnels with square or rectangular cross sections. The larger tunnels are partially filled with water molecules and/or cations.

2. *Layer structures*. The layered MnO_x (sometimes called *phyllomanganates*) consist of stacks of sheets, or layers, of edge-sharing MnO_6 octahedra. The interlayer regions can host water molecules and a wide range of cations.

Although manganese oxides exist with a continuous range of compositions between MnO and MnO_2, it is MnO_2 which is by far the most important oxide in this group [29]. For this reason, among the great variety of MnO_x, the form MnO_2 is the one for which we have more information. In fact, despite MnO_x have been extensively studied for the past

several decades, details of many of their atomic structures are poorly understood, and there are several phases for which even the basic crystal structures are not known [1].

1.1.1. Manganese Dioxide (MnO$_2$)

Manganese dioxide (MnO$_2$) crystallizes with various morphologies and crystallographic forms including the $\alpha-$, $\beta-$, $\gamma-$, $\delta-$, $\epsilon-$, $\lambda-$, $R-$ and $T-$polymorphs, which are naturally occurring minerals such as hollandite, pyrolusite, nsutite, birnessite, akhtenkite, spinel, ramsdellite, and todorokite respectively. The polymorphism is due to the different ways of linking the MnO$_6$ octahedra through corner- or edge-sharing that lead to variations in the chain and tunnel structures (see figure 1.1) [8, 13].
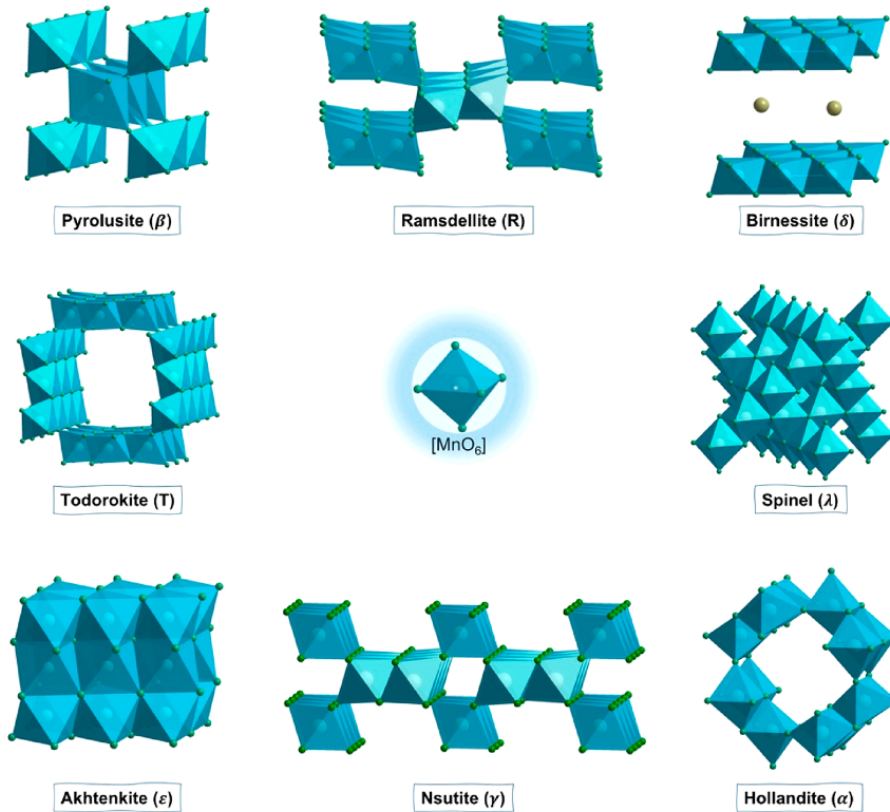

Figure 1.1: Representation of different MnO$_2$ polymorphs. Taken from [8].

Among these, the most thermodinamically stable and abundant is the *pyrolusite* ($\beta-$MnO$_2$) which has a rutile-type structure consisting of single chains of MnO$_6$ octahedra sharing corners to form a 1×1 tunnel framework [1, 28]. The tunnels in pyrolusite are too small to accommodate other chemical species, and chemical analyses indicate that the composition deviates at most only slightly from pure MnO$_2$ [1].

Other polymorphs with tunnel structure are [1, 8, 27, 28]:

- *Ramsdellite* ($R-MnO_2$). The ramsdellite structure consists of double chains of MnO_6 octahedra sharing edges, which are in turn linked each other by octahedra sharing corners to form a framework having tunnels with rectangular shaped cross sections (1×2). Tunnels are generally empty but chemical analyses commonly reveal minor amounts of water, Na, and Ca that presumably are located in the channels.

- *Nsutite* ($\gamma-MnO_2$). The nsutite structure is usually explained by a random intergrowth of pyrolusite layers in a ramsdellite matrix which results in a framework of randomly distributed 1×1 and 1×2 tunnels. Chemical analyses of nsutite typically show small quantities of Na, Ca, Mg, K, Zn, Ni, Fe, Al, Si, and water that probably are accommodated in the larger tunnels or along grain boundaries. Charge balance is maintained by substituting Mn^{3+} for some of the Mn^{4+}.

- *Hollandite* ($\alpha-MnO_2$). As in ramsdellite, the hollandite structure is constructed of double chains of edge-sharing MnO_6 octahedra, but they are linked in such a way as to form tunnels with square cross sections (2×2). The tunnels are partially filled with large uni- or divalent cations (Ba^{2+}, Na^+ and K^+, etc.) and, in some cases, water molecules. The charge balance is once again obtained by substitution of Mn^{4+} with lower valence cations (Mn^{3+} or eventually Fe^{3+}, Al^{3+}, etc.).

- *Todorokite* ($T-MnO_2$). The todorokite structure consists of triple chains of edge-sharing MnO_6 octahedra linked to form square shaped 3×3 tunnels occupied by water and a large variety of cations, such as Ca^{2+}, Mg^{2+}, Ba^{2+}, K^+, and Na^+. Lower valence cations such as Mn^{3+}, Ni^{2+}, and Mg^{2+}, which substitute for Mn^{4+} to offset charges on the tunnel cations, appear to be concentrated into the sites at the edges of the triple chains.

For what concerns the polymorphs with layered structure we mention the *Birnessite* ($\delta-MnO_2$). The basic structural unit of birnessite is a sheet of MnO_6 octahedra which alternates with interlayer cations such as K^+, Na^+, Ca^{2+} and Mg^{2+}. Water molecules are also present in the interlayer sites. Once again lower valence cations (Mn^{3+}) are necessary to compensate the charges. Other polymorphs are the *Akhtenkite* ($\epsilon-MnO_2$), whose structure consists in a dense packing of MnO_6 octahedra which makes unfavorable any kind of intercalation of cations, and the $\lambda-MnO_2$ polymorph which is a metastable form of manganese dioxide with a three-dimensional spinel structure [8].

1.1.2.   Other Manganese Oxides

As already mentioned, MnO_x does not exist only in the form of MnO_2 but other minerals are present in nature (even if in smaller amounts) and can also be synthesized using a variety of physical and chemical methods. Among these we mention hausmannite (Mn_3O_4), manganese sesquioxide (Mn_2O_3), manganosite (MnO) and other metastable forms (e.g., Mn_5O_8). *Hausmannite* is a mixed-valence ($+2$, $+3$) [27] oxide which exibits a tetragonally distorted spinel structure in which Mn^{3+} are in octahedral coordination whereas Mn^{2+} are in tetrahedral coordination (see Figure 3.8a) [28, 29]. Mn_3O_4 is formed when any MnO_x is heated to about 1000°C in air [29, 30]. A related structure to Mn_3O_4 is the $\gamma-Mn_2O_3$ which can be obtained by oxidation and subsequent dehydration of the hydroxide precipitated from aqueous Mn^{2+} solutions. By heating MnO_2 at temperatures less severe than the one required to obtain Mn_3O_4 the more stable $\alpha-$form of Mn_2O_3 results. The $\alpha-Mn_2O_3$ has a *bixbyite* cubic structure [11, 27] which involves six-coordinate Mn^{3+} but with two $Mn-O$ bonding longer than the other four (see Figure 1.2a). These two forms of Mn_2O_3 are usually grouped under the name of *manganese sesquioxide.* To conclude, reduction with hydrogen of any oxide of manganese produces the lowest oxide (Mn^{2+}), the grey to green *manganosite* (MnO) which has a closely packed rock-salt structure [28, 29].

The following table summarizes all the MnO_x compounds just discussed:

Compound	Mineral	Crystal symmetry	Features
$\alpha-MnO_2$	Hollandite	Tetragonal	(2×2) Tunnel
$\beta-MnO_2$	Pyrolusite	Tetragonal	(1×1) Tunnel
$\gamma-MnO_2$	Nsutite	Hexagonal	(1×1)/(1×2) Tunnel
$\delta-MnO_2$	Birnessite	Rhombohedral	($1 \times \infty$) Layer
$\epsilon-MnO_2$	Akhtenkite	Hexagonal	Dense stack
$\lambda-MnO_2$	Spinel	Cubic	(1×1) Tunnel
$R-MnO_2$	Ramsdellite	Orthorhombic	(1×2) Tunnel
$T-MnO_2$	Todorokite	Monoclinic	(3×3) Tunnel
$\alpha-Mn_2O_3$	Bixbyite	Cubic	C-type
$\gamma-Mn_2O_3$		Tetragonal	
Mn_3O_4	Hausmannite	Tetragonal	Spinel-like
MnO	Manganosite	Cubic	Rock-salt

Table 1.1: Summary of crystallographic data of some MnO_x. Data taken from [13, 31]
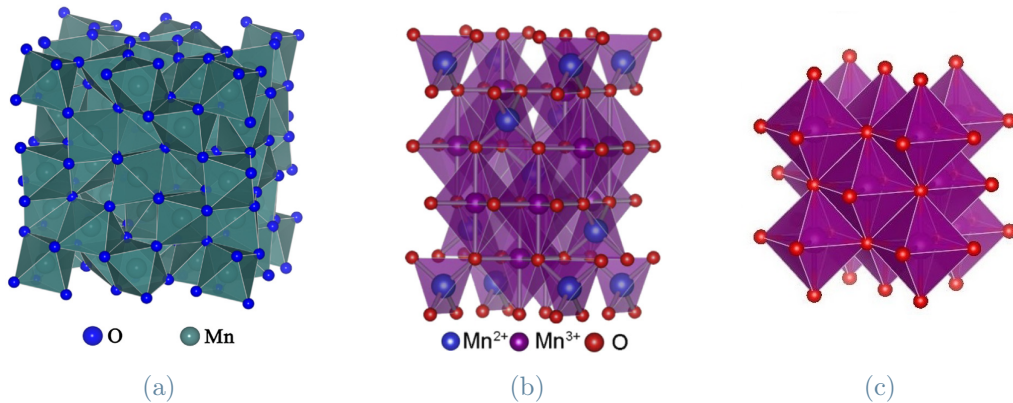
Figure 1.2: Representation of Mn_2O_3 (a), Mn_3O_4 (b) and MnO (c) crystal structures. Images taken from [11], [12] and [32] respectively.

1.2. Raman Spectroscopy of MnO_x: state of the art

The poor crystallinity of MnO_x, the size of the crystallites typically limited to the nanoscale, and the presence of associated phases make the identification and proper characterization of natural MnO_x a real challenge by standard methods such as X-ray powder diffraction (XRPD). Spectroscopic techniques provide a valuable tool for studying these minerals, being sensitive to short-range metal-oxygen arrangements. Fourier-transform infrared spectroscopy (FT-IR) in particular is a very powerful technique to characterize MnO_x. Unfortunately, both XRPD and FT-IR do not provide satisfactory data: X-ray patterns are characterized by broad and weak Bragg reflections and FT-IR spectra usually show broad and overlapping bands that do not always allow simple and unique identification. To overcome these difficulties, Raman spectroscopy can be a valuable complementary technique for the investigation of these materials, being a fast, non destructive method that can provide information about local atomic coordination environments as well as longer-range structure, and therefore can be a useful identification technique even for highly disordered materials [28, 33].

Although this technique was widely used for the recognition of MnO_x, reliable literature reference data are missing due to strong discrepancies between the different authors. Literature data are often conflicting and contradictory both for the spectra collected on natural and on synthetic phases, and usually they do not allow a proper identification of the Mn species. These disagreements can be due to many factors such as the experimental condition, the incorrect identification of the examined cryptocrystalline materials, and the wide variety of possible mixtures between different MnO_x. Moreover, MnO_x have a low Raman activity and they are very sensitive to the laser heating. In fact, the interaction

between the laser beam and the manganese minerals may lead to the degradation of the sample, as a function of the laser power and irradiation time: the strong absorption of photon energy by the blackish MnO_x produce a local heating that can cause shifts and broadening of the Raman peaks due to photo-induced or thermal-induced chemical reactions. A study conducted by Bernard et al. [34] shows that each MnO_x has its own resistance to the laser heating and relates it to the different oxidation state of the Mn and to their Raman activity. Furthermore, the thermal stability of MnO_x depends on the structural frameworks, the type of the tunnel/layer cations or molecules, the grain size and crystallinity [28]. The correct analysis boundary condition is a real challenge, so much so that even studies that emphasize the use of 'low laser power' are inconsistent in their determinations of the instrumental conditions required to maintain specimen integrity. This issue is complicated by the effects of different laser wavelengths, power densities, and optics used for data collection [33]. Lastly, some MnO_x have characteristic Raman spectra and can be easily recognized by using Raman spectroscopy alone, but in order to characterize different MnO_x phases that show very similar Raman spectrum, integration of Raman data with other techniques is mandatory [28].

As far as possible, a general overview of the main features of the Raman spectra for different MnO_x will be presented in the following. Raman peaks are mainly attributed to the fundamental vibrational modes from the MnO_6 octahedra which contains six normal vibrational modes. Among these modes only three are Raman active while the other three are IR active but can be activated when the MnO_6 octahedra form the characteristic layered and/or tunnel structures of MnO_x [27]. In the MnO_x Raman spectra, three main regions can be distinguished [28]: one ranging from 200 to 450 cm^{-1} related to skeletal vibrations; one ranging from 450 to 550 cm^{-1} associated to the deformation modes of the $Mn-O-Mn$ chains in the octahedral lattice and one ranging from 550 to 750 cm^{-1} related to the stretching modes of the $Mn-O$ bonds in the MnO_6 octahedra. A study conducted by Xin et al. [27] reported that «there are no obviously characteristic Raman spectra in the range of $1000-5000$ cm^{-1}».

In the spectral range $550-750$ cm^{-1} the double Raman peaks that appear in the range from 550 to 600 cm^{-1} and from 630 to 670 cm^{-1} (see Figure 1.3) can be used to distinguish between the different polymorphs of MnO_2 and other MnO_x. These Raman peaks are common features of all the MnO_x and are strictly related to the oxidation state of Mn [27].
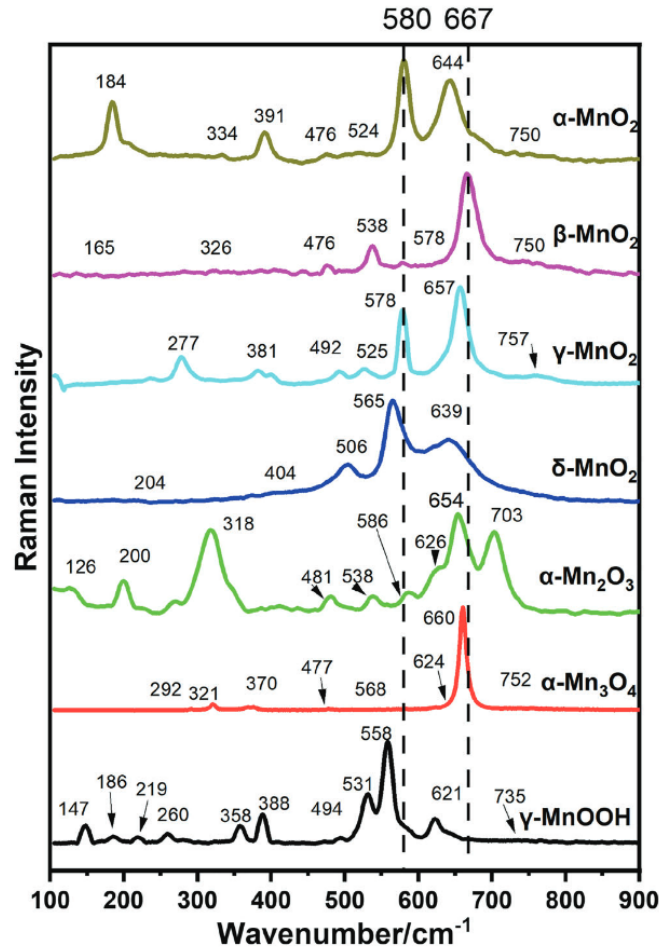
Figure 1.3: Raman spectra of MnO_x in the range of $100-900$ cm^{-1}. Major Raman peaks in the range $550-700$ cm^{-1} exhibit the variations for different MnO_x and are designated with two black dotted lines. Taken from [27]

The peaks width indicates the degree of crystallinity of the specimen: sharp Raman peaks indicate relatively good crystallinity while broad peaks are linked to poor crystallinity or amorphous materials. Consistent with its highest crystallinity, Mn_3O_4 Ramans spectra exhibits the sharpest peaks among all samples: the sharpest and strongest peak at 660 cm^{-1} and two other weak peaks at 321 and 370 cm^{-1} [27] (see Figure 1.3).

Since the tunnels in pyrolusite are too small to accomodate other chemical species, the Raman spectra of $\beta-MnO_2$ can be used as a standard to discriminate other MnO_2 by comparing their Raman spectra. Refering to the $\beta-MnO_2$ Raman spectra reported in Figure 1.3, two sharp peaks are located at 667 and 538 cm^{-1}, indicative of a rutile-type MnO_2 structure (see section 1.1.1: 'Manganese Dioxide (MnO_2)'); other peaks are too weak to be observed [27]. Similar data are reported also by Bernardini et al. [28] who report strong band at $\sim$ 661 cm^{-1} and weak bands at $\sim$ 532 and $\sim$ 755 cm^{-1} for

pyrolusite. These data are confirmed by many other works [35–37] but they are not in agreement with those reported in other studies by Buciuman et al. [38] and Bernard et al. [34] who report a strong band at ~ 580 cm^{-1} in the $\beta-MnO_2$ spectra. Bernardini et al. [28] justify this discrepancy by saying that the band at 580 cm^{-1}, occasionally reported in the $\beta-MnO_2$ spectra, is due to thermal degradation during data collection since pyrolusite is very sensitive to the heating and at $\sim 450°$C it trasforms into bixbyite ($\alpha-Mn_2O_3$) [39] «whose spectrum is characterized by a strong peak at 580 cm^{-1}». However, the attribution of the peak at ~ 580 cm^{-1} to the bixbyite formation is not confirmed by Post et al. [33] which report: «Our Raman spectra for bixbyite (Figure 1.4a), however, did not exhibit any strong features near 585 cm^{-1}».

According to Xin et al. [27] the $\alpha-Mn_2O_3$ Raman spectra exhibits three major peaks at 703, 654 and 318 cm^{-1} and several weak bands (126, 200, 481, 586 and 626 cm^{-1}) as depicted in Figure 1.3. In particular, the 703 cm^{-1} and 318 cm^{-1} peaks may be due to the unique bixbyite structure (see section 1.1.2: 'Other Manganese Oxides') with two Mn sites. These considerations are consistent with works conducted by Post et al. [33] (see Figure 1.4a) and Julien et al. [31] but they are in disagreement with data provided by Bernard et al. [34] which report, in accordance with Bernardini et al. [28], the presence of a main peak at 581 cm^{-1}, a broad peak at 509 cm^{-1} and a shoulder at about 630 cm^{-1} (see Figure 1.4b).
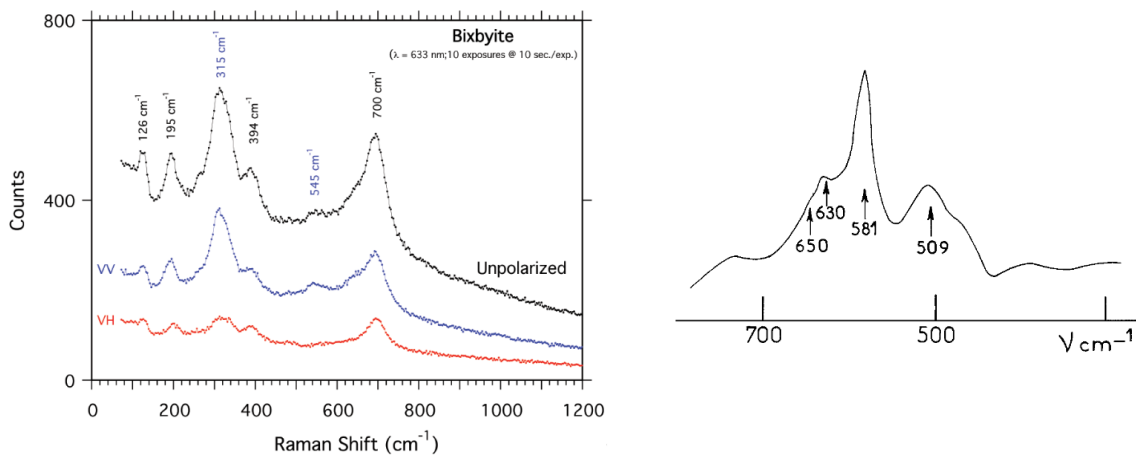
(a) Raman spectra (633 nm) for bixbyite according to Post et al. [33]

(b) Raman spectra of bixbyite Mn_2O_3 (514.5 nm, 12.5 mW) according to Bernard et al. [34].

Figure 1.4: Comparison between the Raman spectra for bixbyite reported by Post et al. [33] (a) and the one reported by Bernard et al. [34] (b). Discrepancy between data is clearly evident.

What has just been discussed, is only one of the possible examples that confirms the great confusion present in literature about the characterization of these materials, but many others could be reported.

1.3.   Applications of MnO$_x$

MnO$_x$ materials have been widely used in various applications over the millennia. Since ancient times pyrolusite was used in art works as pigment for pottery, mural paintings, and stained glass. By the mid-19th century Mn was an essential component in steel making, as a deoxidizer and desulfurizer and for making hard-steel alloys (approximately 80–90% of the world production of Mn ore is consumed by the steel industry). Moreover, MnO$_x$ are important geomaterials that could play a key role in environmental applications, by controlling the partitioning of arsenic and heavy metals between rocks, soils, and aqueous systems [1, 28]. Today MnO$_2$ is an important functional metal oxide, which is technologically attractive for applications in different fields such as catalyst, absorbent of toxic metals, water-purifying agent, ion/molecular-sieves, artificial oxidase, component of the dry cell (Leclanché cell), inorganic pigment in ceramics. MnO$_2$ has also been widely used in Duracell (alkaline) based barriers, photocatalytic activities, and electrolysis [13].

Extensively used in industry for more than a century, MnO$_x$ now find great renewal of interest as nanostructured materials with very attractive physicochemical properties for storage and conversion of energy applications [13, 28]. In the field of energy storage, the excellent electrochemical properties of several MnO$_x$ phases are attracting much attention for positive electrode materials for Lithium- (Li) and Zinc- (Zn) ion-batteries. This application generates an important activity in the field of Solid State Chemistry to synthesise new phases of MnO$_x$ with improved electrochemical properties such as stability during cycling and large reversible capacity under fast discharge rate [31].

1.3.1.   Lithium-ion batteries

The history of the battery, today, has not yet been fully elucidated. We know the voltaic pile was introduced by A. Volta (1745−1827) around 1800, around the 1866 G. Leclanché (1839−1882) was awarded a patent for the so-called Leclanché element afterwards developed by C. Gassner (1855−1942) and in 1901 P. Schmidt (1868−1948) succeeded in inventing the first galvanic dry element based on zinc and carbon. A further development of batteries mainly regards only technical and chemical properties of the elements rather than increase in specific energy or specific power. A new era began when, in the early 70s, at the Technical University of Munich, Germany, the first ideas for a new system

was born: lithium batteries with reversible alkaline-metal-ion intercalation in the carbon anode and an oxidic cathode [40].

The first Li-based battery, introduced in the market by Sanyo in 1972, was a battery that could not be recharged after the initial discharging (primary battery). The materials were lithium for the negative electrode and manganese dioxide for the positive electrode. The first rechargeable battery (secondary battery) was developed by Moli Energy in 1985, and it was based on lithium (anode) and molybdenum sulfide (cathode). The next step toward a lithium-ion-battery (LIB) was the use of materials, for both electrodes, that enable an intercalation and deintercalation of lithium and also have a high voltage potential. Some years after, the first commercial LIB was launched on the market by Sony in 1991; the active materials for the positive and negative electrodes were lithium cobalt oxide ($LiCoO_2$) and carbon, respectively [40]. Since their introduction in 1991, energy storage has more than doubled and today LIBs are dominating in the portable electronics market due to their highest energy storage capability compared to any rechargeable battery system [40, 41]. LIBs have also begun to enter the electric vehicle market and are being intensively pursued for grid energy storage [41].
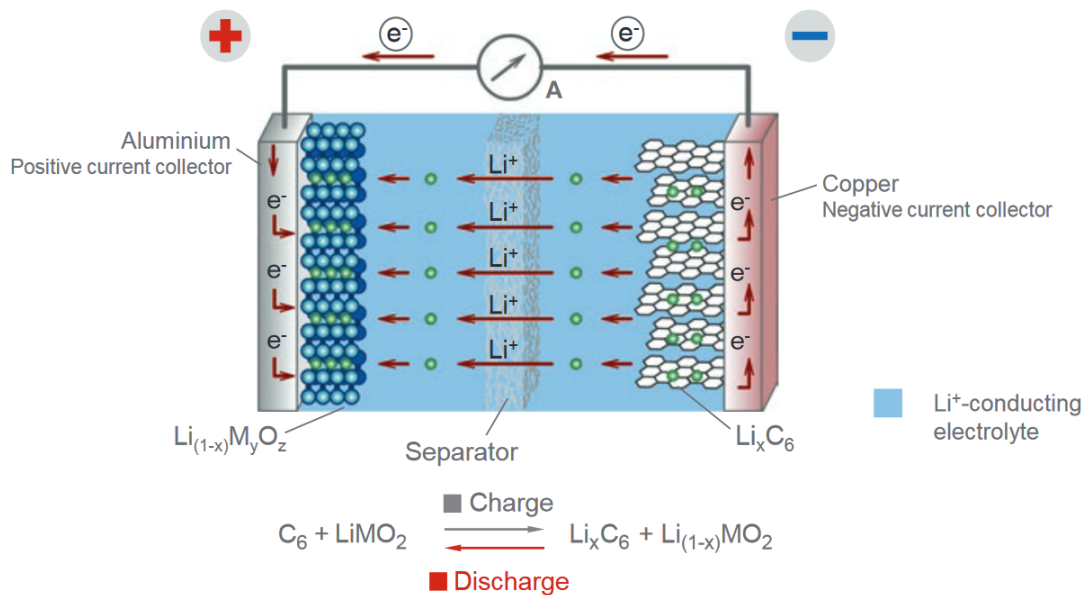
Figure 1.5: Set-up of a Li-ion-battery shown during discharging process. Taken from [40]

Figure 1.5 shows the basic principle and the set-up of a rechargeable LIB. An ion-conducting electrolyte, containing a dissociated lithium conducting salt, is situated between the two electrodes which are separated and electrically isolated by means of a porous membrane. Both the anode and the cathode are lithium intercalation materials [42]. The

positive electrode contains active materials such as mixed oxides, while the active materials for the negative electrode are mainly graphite and amorphous carbon compounds. During discharging, lithium is deintercalated from the anode and lithium ions migrate from the negative electrode, through the electrolyte and the separator, to the positive one. At the same time, electrons migrate from the anode via an outer electrical cable to the cathode. During charging, the process is reversed: Li ions migrate from the positive electrode, through the electrolyte and the separator, to the negative electrode [40].

The parameters that need to be considered in adopting LIBs for various applications are: energy, power, charge-discharge rate, cost, cycle life, safety, and environmental impact. These parameters are largely determined by the properties and characteristics of the component materials as well as the cell engineering and system integration involved. The current Li-ion technology is based on insertion-compound cathodes and anodes and organic liquid electrolytes (e.g., $LiPF_6$ salt dissolved in a mixture of organic solvents). While graphite has dominated as anode material in commerical LIBs, for the cathode there are three possible choices [41]: layered $LiMO_2$ (M = Mn, Co, and Ni), spinel $LiMn_2O_4$, and olivine $LiFePO_4$. Crystal structures of these materials are depicted in Figure 1.6.
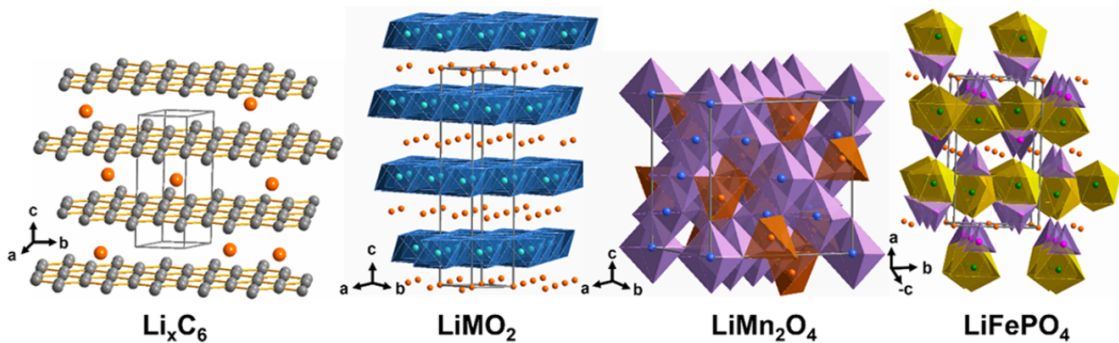
Figure 1.6: Crystal structures of Li_xC_6, layered $LiMO_2$ (M = Mn, Co, and Ni), spinel $LiMn_2O_4$, and olivine $LiFePO_4$ used as anode and cathode materials for LIBs. Taken from [41]

Each of these three cathodes has its advantages and disadvantages. The layered structure gives the highest practical capacity (currently up to $\sim$180 Ah kg^{-1}) among the three, but suffers from structural and/or chemical instabilities during cycling depending on the chemical composition and state of charge. The $LiMn_2O_4$ spinel cathode with a three-dimensional structure and lithium ion diffusion paths offers high rate capability and good structural stability without phase transformations but suffers from a limited practical capacity (< 120 Ah kg^{-1}) and manganese dissolution. The olivine $LiFeO_4$ cathode, on the other hand, offers good thermal stability and safety without oxygen release, but suffers

from limited practical capacity (< 160 Ah kg^{-1}), particularly limited volumetric capacity, lower operating voltage of ~ 3.4 V, and poor electronic and lithium ion conductivity [41].

The growing energy consumption and environmental concerns have been driving an ever-increasing demand for reliable electrical energy storage (EES) systems for the utilization of renewable and clean energy resources. EES systems can be divided into two categories: one works via the charge accumulation at the interfaces between electrodes and electrolyte (generally termed as a *capacitor*), the other depends on the redox reactions accompanied by ion transportation (defined as *battery*). Among battery systems, LIBs have long been the most attractive and widely used EES system. Although LIBs benefit of high gravimetric energy density (> 250 Wh Kg^{-1}), long cycle life and light weight, their application as large-scale energy storage systems is impeded by their high cost and safety and environmental issues. In LIBs, highly toxic and combustible organic electrolytes are used and the possible reactions between electrodes and electrolytes pose additional risks. Moreover, the energy efficiency and gravimetric power density of LIBs are unsatisfactory due to the low ionic conductivity of organic electrolytes and the formation of solid electrolyte interphases. In addition, the cost of LIBs is relatively high due to not only the high price of materials but also the stringent cell assembly requirements. Considerable research efforts have been made in an attempt to address the above concerns: development of solid-state electrolytes for all-solid-state LIBs; design of ionic liquids as alternative electrolytes; recent research activities have been conducted on bringing lithium metal back as the anode through surface passivation and morphology design in combination with the tailored electrolyte chemistry; and search for cobalt-free cathodes with large capacity and high voltage is also making steady progress. There is no doubt that new progress is going to be made on the development of LIBs with better performance, reduced cost, and higher safety [8].

1.3.2.   Zinc-ion batteries

In spite of the great interest on Li-based rechargeable batteries, increased attention has also been paid to the exploration of other promising EES systems. The most essential criteria for developing the ideal large-scale EES systems are low cost, high reliability, good safety, environmental friendliness, high energy efficiency, long cycle life, and high gravimetric energy and power densities. Responding to the green and safe requirements, exploration of multivalent, metal-ion (Mg^{2+}, Ca^{2+}, Zn^{2+}, Al^{3+},) batteries based on safe, nontoxic, and low-cost aqueous electrolytes also becomes desirable. Compared to organic electrolytes, aqueous electrolytes are non-flammable and have a higher ionic conductivity (aqueous electrolytes: ~ 1 S cm^{-1}, organic electrolytes: $\sim 1-10$ mS cm^{-1}) which allows

fast charge-discharge rates. Moreover, compared to organic LIBs, aqueous rechargeable batteries are more cost-effective and easier to be assembled as they do not require strict control of manufacturing environment. Among the "beyond lithium-ion" battery technologies, aqueous Zn-ion-batteries (ZIBs) are particularly attractive owing to the following attractive features [8, 10, 43]:

1. the low cost arising from Zn natural abundance and massive production. ZIBs also have the potential to use lower-cost manufacturing techniques since they do not require special dry room conditions;

2. Zn and ZnO are easy to recycle and the recycling of Zn-based batteries is already established and commercialised for primary Zn batteries [6];

3. the low redox potential of Zn (-0.76 V vs. SHE) is responsible for the high electrochemical stability in aqueous electrolytes due to a high overpotential for hydrogen evolution;

4. the diversity of potential electrolytes, including aqueous ad non-aqueous electrolytes;

5. the improved safety and reduced toxicity;

6. the use of near-neutral or slightly acidic electrolyte (e.g., pH = 3.6–6.0) can avoid the formation of zinc dendrites and ZnO byproducts usually occurring in alkaline Zn batteries. This leads to the reversibility of the Zn plating/stripping process which in turn allows to achieve long cycle life;

7. higher volumetric energy density (i.e., 5851 mAh cm^{-3} compared to 2061 mAh cm^{-3} for LIBs) can be achieved due to the high density of Zn and the fact that two electrons are involved in the electrochemical reactions;

8. high theoretical anode capacity (820 mAh g^{-1}).

Therefore, the aqueous ZIBs are compelling alternative battery systems for large scale application. The relatively high gravimetric energy and power density of aqueous ZIBs as compared with those of other EES systems are shown by the Ragone plot in Figure 1.7: the aqueous ZIBs probably possess the highest gravimetric energy and power density combination owing to their fast reaction kinetics endowed by the smaller working ions and the open frameworks of the cathode materials employed [8].
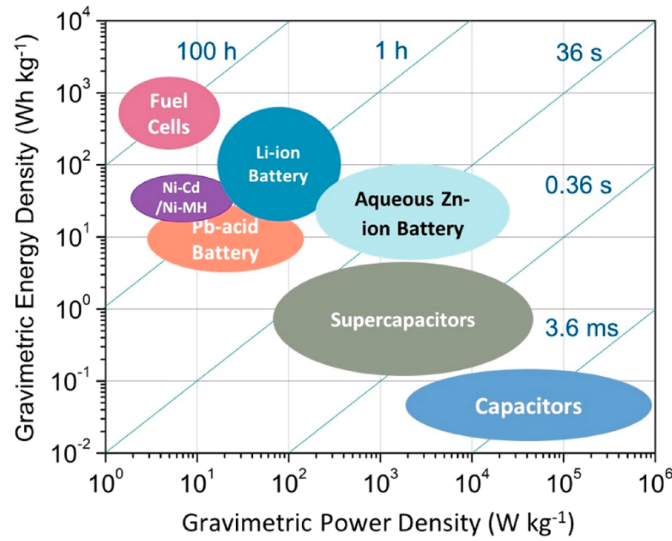
Figure 1.7: Ragone plot of several EES systems. Taken from [8]

Rechargeable ZIBs can be considered the evolution of primary alkaline Zn batteries which have been first commercialized in the 1960s and still play an essential role in today's battery landscape. Despite the apparent similarity to alkaline batteries, the modern ZIBs feature a distinctly different cell reaction [6]. The basic principle and the device structure are shown in Figure 1.8. The two electrodes are separated by a glass fiber or a cellulose filter, and a water-based Zn^{2+}-containing salt solution (electrolyte). The working principle is similar to that of LIBs. During discharge, Zn^{2+} ions strip from the metallic anode and insert into the cathode material generating electrons; while during the charge process Zn^{2+} ions extract from the cathode material and plate on the metallic anode [8].
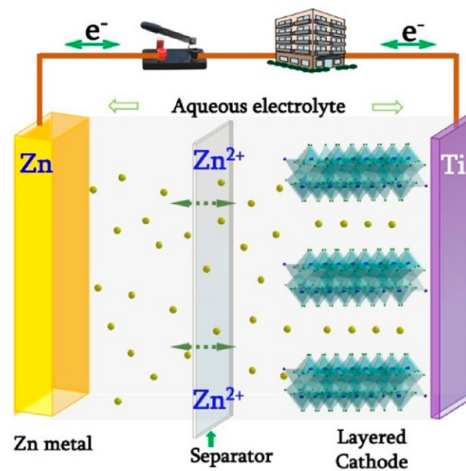
Figure 1.8: Schematic illustration of the ZIB cionfiguration. Taken from [8]

Given zinc metal as the anode, the main obstacle to the commercialization of ZIBs as grid-scale renewable energy storage systems, is the lack of an appropriate intercalation cathode material [43]. Moreover, different reaction mechanisms are observed for the same cathode material in literature [6]. Unfortunately, electrode materials suitable for Li^+-ion insertion/extraction turned out to be incompatible for aqueous ZIBs owing to the larger atomic mass and high positive polarity on Zn^{2+} ions. To resolve this issue, significant efforts and investigations have been carried out on various cathode materials for ZIBs [43]. The main objective for cathode design is the reversible intercalation of the charge carrier into the host structure. For Zn ions, the host structure must be a material with vacancy sites and stable structures that remain intact upon the intercalation of Zn^{2+} ions. For this purpose, the layered, tunnel, or spinel structures found in metal oxides are the most suitable. Several materials have successfully demonstrated intercalation of zinc. Among them, manganese and vanadium (V) oxides currently receive most interest. The polymorphs of MnO_2 are the most researched material for ZIB as they offer a good compromise between cycling stability and capacity [6]. Electrodeposited MnO_2 cathodes were successfully recharged in near-neutral electrolytes in 1980s but limited cyclability and phase change after cycles cause research to stagnate [6]. Nevertheless, in 2012 Kang et al. [44] presented «a safe and ecofriendly power-type battery, which composes of an $\alpha-MnO_2$ cathode, a zinc anode, and a mild $ZnSO_4$ or $Zn(NO_3)_2$ aqueous electrolyte» (shown in Figure 1.9) which had revived research interest and led to a rapid growth in publications.
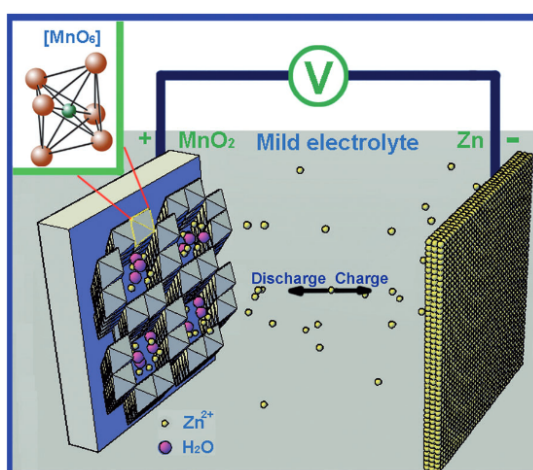
Figure 1.9: Schematic illustration of the first ZIB presented by Kang et al. [44]

Performance and stability of a MnO_2 cathode have been found to strongly depend on the crystal structure and morphology [8–10, 43]. A summary of the comparative performance of the various crystalline structures of MnO_x cathodes in ZIBs is presented in Figure 1.10.

Theoretical capacity of MnO_2 can be calculated according to the step-wise reactions [10]:

$$Mn^{4+}O_2 + Zn^{2+} + 2e^- \longrightarrow ZnMn_2^{3+}O_4, \quad 308mAh\ g^{-1} \tag{1.1}$$

$$ZnMn_2^{3+}O_4 + Zn^{2+} + 2e^- \longrightarrow 2ZnMn^{2+}O_2, \quad 308mAh\ g^{-1} \tag{1.2}$$
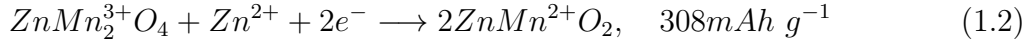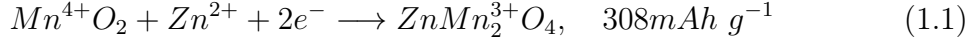
These results demonstrate that MnO_2 can, in principle, deliver a capacity of 308 mAh g^{-1} and 616 mAh g^{-1} in the redox reaction Mn^{4+}/Mn^{3+} and Mn^{4+}/Mn^{2+}, respectively, (Fig. 1.10a), regardless of where the Zn^{2+} is finally located. Based on these two reactions and their corresponding capacities, one can understand the behavior of other MnO_2 cathodes with varying crystalline structures [10].

(a)

(b)
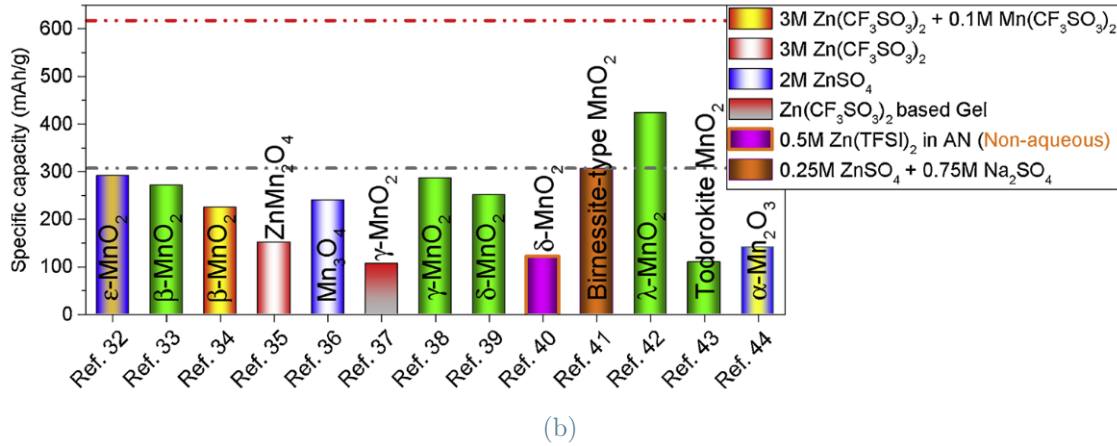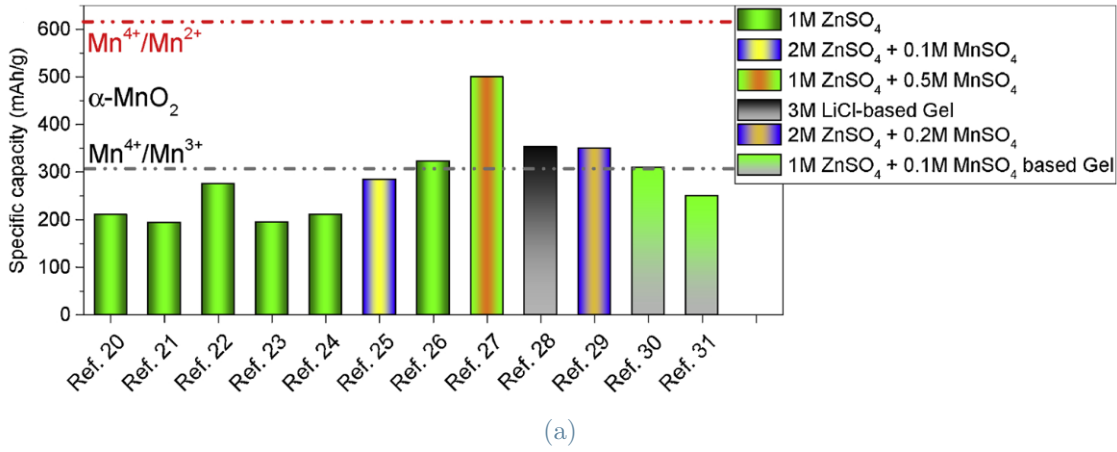
Figure 1.10: Specific capacity of MnO_x with different crystal structures and different electrolytes: $\alpha-MnO_2$ (a), other MnO_x crystal structures (b). For references, go to [10].

Each polymorph has its own merits and issues. The most commonly studied among the various polymorphs is the α-MnO_2 due to its large tunnel size (~ 4.6 Å). Benefiting from this structural advantage, α-MnO_2 could deliver a large specific capacity (> 200 mAh g^{-1})

with a moderate discharge voltage (~ 1.3 V). However, it suffers from rapid capacity fading upon cycling and poor high rate performance [8]. Another appealing cathode candidate for ZIBs is the layered-structured δ-MnO$_2$ which exhibits a wide interlayer distance (~ 7.0 Å) suitable for Zn^{2+} ion accommodation. However, upon long-term cycling, also the δ-MnO$_2$ electrode generally suffers from rapid capacity fading [8]. Nsutite-type MnO$_2$ (γ-MnO$_2$) is the first example of manganese oxide to be used in ZIBs in 2003 [45]. High capacity of 285 mAh g^{-1} can be achieved but the cycle performance was not so optimal [10]. Among all the MnO$_2$ polymorphs, β-MnO$_2$, is regarded as the most thermodynamically stable structure, although its narrow 1×1 tunnels are usually not conductive to the diffusion of Zn^{2+} cations [9, 43]. More detailed discussion of MnO$_x$ polymorphs for ZIBs are extensively reviewed in these papers [8–10, 43].

MnO$_x$ exhibit complicated electrochemical behaviours with structural and phase transformations from tunnel-like to spinel-like and layered structure, or precipitation of Zn-containing phases (e.g., ZHS: Zn-hydroxide sulfate) [10, 43]. Although Zn intercalation is the mainly reported charge storage mechanism, there is an ongoing debate about the contribution of other processes. For example, many works [7, 8, 10, 43] reported the co-intercalation of Zn^{2+} and H$^+$ supported by the verified formation of Zn-birnessite (Zn$-\delta$-MnO$_2$) and MnOOH. Anyway, according to the current research, energy storage mechanism of ZIBs can involve one or a combinations of the following mechanisms [46]:

1. Zn^{2+} insertion/extraction;

2. H$^+$/Zn^{2+} co-insertion/extraction;

3. H$_2$O and Zn^{2+} co-insertion/extraction;

4. conversion reaction;

5. dissolution and deposition reaction.

Finally, the phase transformations of most types of manganese oxide are summarized in Figure 1.11. As we have seen, reactions and conversion processes are complex, and more studies are needed to understand the intercalation processes in manganese oxides.
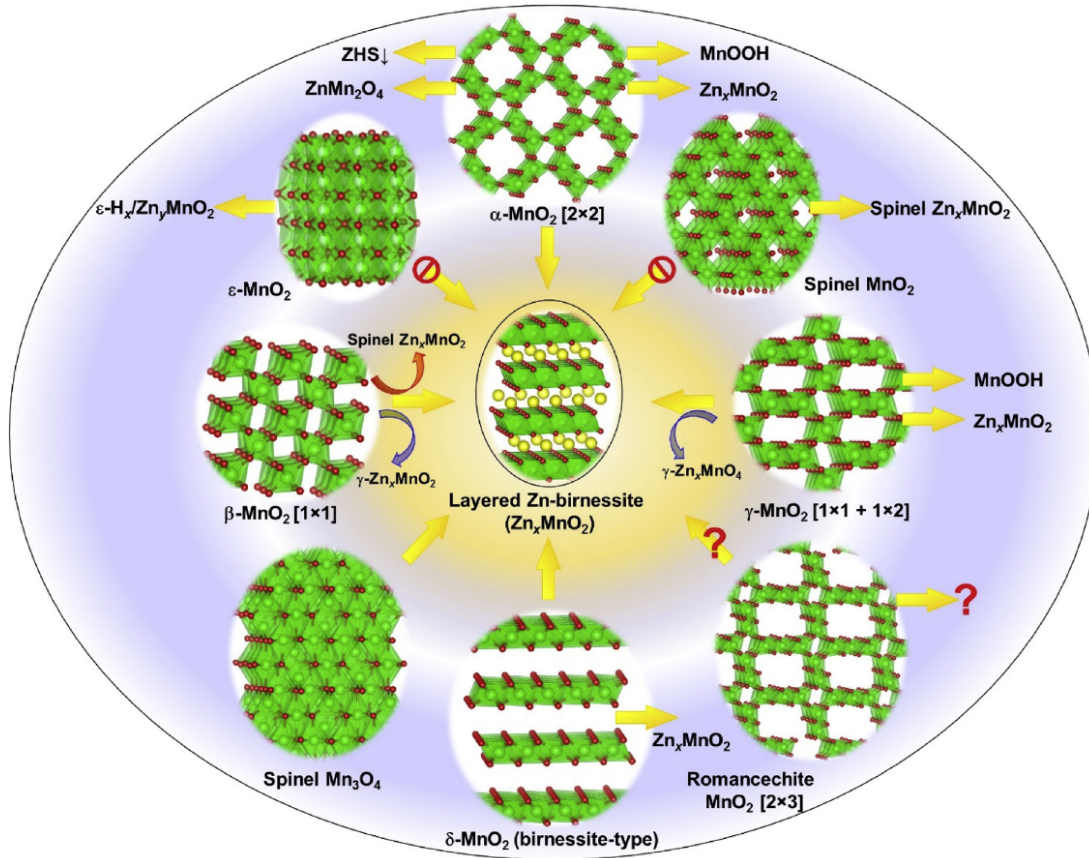
Figure 1.11: Summary of phase transition and conversion of most manganese oxides. The green octahedron is MnO_6, in which the red and yellow dots represent oxygen and zinc atoms, respectively. Image taken from [10]

1.4.   Thesis objectives

In this work, different MnO_x phases (MnO_2, Mn_2O_3, and Mn_3O_4) are produced in the form of thin films by Pulsed Laser Deposition (PLD) and post-deposition annealing treatments. This powerful combination allows to obtain a decoupled control on the phase and morphology of the films. Moreover, the characterization of the films by Raman Spectroscopy and X-Ray Diffraction (XRD) helps to better clarify the controversial situation surrounding the assignment of different MnO_x phases. Although the electrochemical characterization of the films is not the main focus of this work, some early attempts are made in order to try to understand the electrochemical behaviour of the films, which can be employed as model systems to study the complex response of MnOx materials in simple conditions. The exploratory character of this work makes it a good starting point for further future development of MnO_x materials. The focus of the thesis is the characterization of the different MnO_x phases which is not only useful at research level but allows

also to optimize processes for specific application.

Summarizing, the objectives of this thesis are:

1. The production of MnO_x thin films by PLD and post-deposition annealing treatments, and the optimization of parameters to obtain a separately control of the phase and morphology of the films;

2. The characterization of the produced MnO_x films by Raman Spectroscopy, Scanning Electron Microscopy (SEM), Energy Dispersive X-Ray Spectroscopy (EDX), X-Ray Diffraction (XRD) and UV-Vis optical spectroscopy, and the correlation of material properties with the parameters used for the sysnthesis;

3. Conducting some prelyminary electrochemical tests using phase-pure MnO_x films as model systems to provide the foundation for future studies of the electrochemical behavior of these materials.

2 | Experimental techniques

The following chapter will be devoted to the presentation of the synthesis and characterization methods adopted in this work. Starting from the PLD technique and furnaces used for the synthesis of the MnO_x films, the morphology, stoichiometry, structural, vibrational and optical characterization methods will be presented in the following.

2.1. Pulsed Laser Deposition

Pulsed Laser Deposition (PLD) is a physical vapor deposition (PVD) technique that exploits the ablation of a target by a pulsed laser source to deposit a wide range of materials in the form of thin films and multilayers even with complex stoichiometry [47, 48]. The versatility of the process relies also on the great number of parameters that can be set such as geometry (position and movement of the substrate with respect to the target), temperature, pressure, target material and background gas. Deposition is also affected by laser properties such as wavelength, fluence (energy density at the target) and pulses duration [49]. Different lasers with different pulse durations ranging from nano to femtosecond can be used and the main difference is related to the physical mechanism of ablation. The most used systems for material deposition are nanosecond lasers, for which the ablation substantially consists in a thermal process [47]. By tuning properly the PLD parameters, films with a great variety of morphologies, thicknesses and densities can be obtained under controlled deposition regimes [49].

The typical PLD apparatus, shown in Figure 2.1, is composed by a laser source and a vacuum chamber hosting the target material and the substrate. The scheme also includes a pumping system, consisting of a primary scroll pump and a turbomolecular pump connected in series, and a gas inlet system with mass flow controllers and pressure gauges that allows pressure control from 10^{-7} Pa to atmospheric pressure [47]. The laser pulses are focused onto the target material inside the chamber by means of an optical path constituted by mirrors, lenses and a viewport. For sufficiently high laser energy density, which depends on the target material, each laser pulse vaporizes a small amount of material which is then ejected from the target and creates a highly forward-directed plasma

plume that provides the material flux for film growth [48].
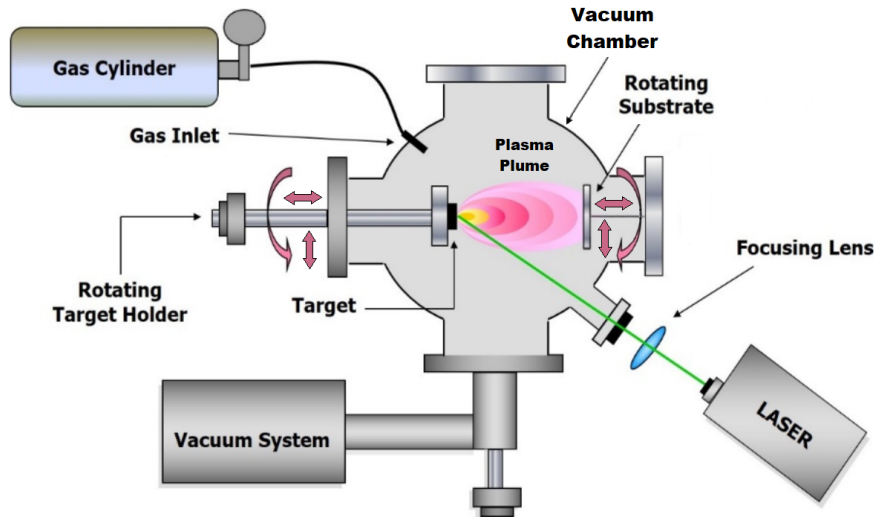
Figure 2.1: Pulsed Laser Deposition scheme with indication of main components and movimentations of target and substrate. Modified from [50].

Typically, the laser incidence angle is of 40-50° with respect to the normal direction to the target surface while the substrate is placed in front of the target. By target manipulation it is possible to optimize the position of the laser spot on the target in order to maintain a uniform ablation of the target surface and to avoid surface roughening. [47]

The characteristics of the plume (temperature, density, velocity, composition and shape) depend on laser and target parameters and on the medium whereby its expansion takes place [50]. PLD processes can be performed both in vacuum and in the presence of an inert or reactive gas, usually exploited to favour nucleation in clusters and/or nanostructures [47, 50]. In addition, the use of reactive gases such as oxygen permits to deposit oxidized species starting from metallic targets and, together with proper post-deposition annealing treatments, opens the way for the production of materials with tailored morphology, crystalline structure and composition [47].

Three distinct conditions can be identified:

1. Under *vacuum* conditions the plasma plume is strongly forward directed and it is characterized by an almost collisionless propagation regime and weak light emission. In such conditions, deposition occurs atom-by-atom leading to compact films formation with high adhesion improved by the high energy of the species impinging the substrate (see Figure 5.8b).

2. When an *inert background gas* is present, at sufficiently high pressure (≥ 10 Pa), a confinement effect is shown: the plume become more spatially confined and its light emission increases due to collisions producing radiative de-excitation of the ablated species. The spatial confinement favours nucleation of clusters in the gas phase which may then diffuse in the background gas thus decreasing their kinetic energy leading to the possibility to deposit nanoporous films. As a result, low energy deposition occurs and a porous cluster-assembled material is formed (see Figure 2.2b).

3. If a *reactive gas* is used as a background atmosphere, chemical interactions between the gas and the ablated species may occur. This allows to deposit clusters with controlled composition and opens the possibility to deposit metal oxide clusters by ablating a metallic target in the presence of oxygen (see Figure 2.2c).

(a) Vacuum   (b) Inert gas   (c) Reactive gas
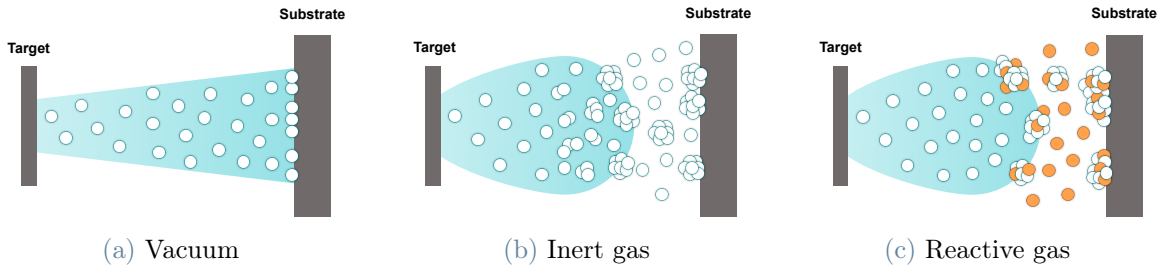
Figure 2.2: Schematic representations of the deposition process in vacuum (a), inert gas (b) and reactive gas (c).

Another important parameter to be considered is the pressure of the background gas. The main effect of an increasing pressure is a confinement effect of the plasma plume, whose maximum extension from the target surface is l_b (see Figure 2.3). A sufficiently high background pressure can slow down the motion of the ablated species toward the substrate causing possible effects on the film morphology. A dimensionless parameter L, defined as the ratio between the target-to-substrate distance ($d_{T\text{-}S}$) and l_b, can be introduced in order to model the influences of these variables on morphology [51]. According to the characteristic length L, if an inert gas is present, three deposition regimes can be defined:

1. $L < 1$: *substrate inside the plume.* No clusters formation occurs, the particles arrive on the substrate with high kinetic energy leading to a very compact, smooth and well adherent film.

2. $L \sim 1$: *substrate at the plume edge.* The kinetic energy of the ablated species reduces due to the interactions with the background gas. Especially when metal

oxides/nitrides are deposited, this regime favours the growth of peculiar tree-like hierarchical nanostructures.

3. $L > 1$: *substrate outside the plume.* Cluster formation is favored due to interactions among ablated species. The kinetic energy of travelling species is further reduced and the production of cluster-assembled nanostructured and nanoporous films occurs.
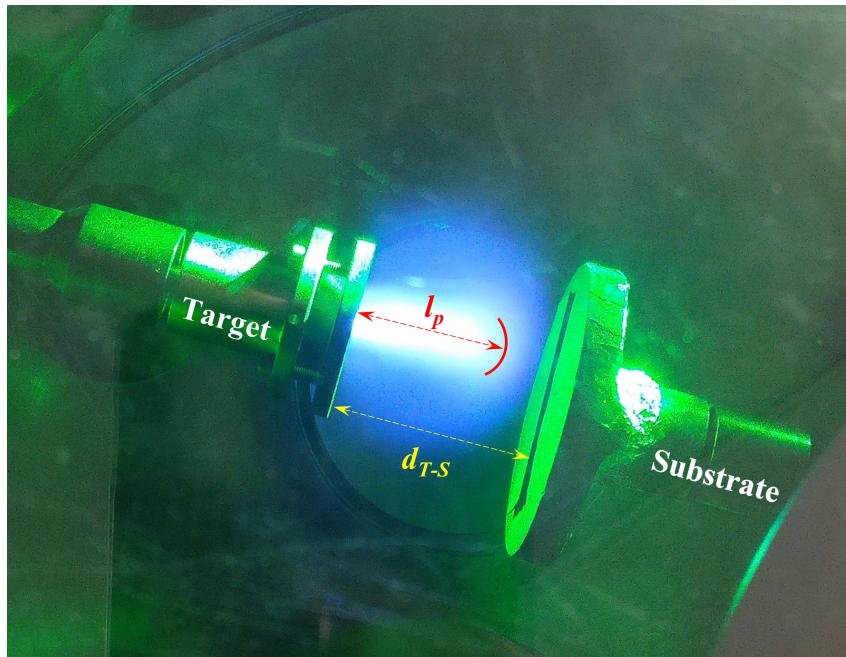
Figure 2.3: Plasma plume during deposition of MnO_x at 100 Pa of oxygen background gas. Visible plasma plume length l_b and target-to-substrate distance $d_{T\text{-}S}$ are reported.

As already mentioned, laser ablation for thin film growth has many advantages linked mainly to the high flexibility and controllability of the process but PLD has also some technical and fundamental drawbacks [52], in particular:

- the production of macroscopic particles called "droplets" during the ablation process;

- the presence of impurities in the target material;

- the presence of crystallographic defects in the film caused by bombardment by high kinetic energy ablation particles;

- deposition on a non-planar sample is not always possible with PLD as a shadowing effect takes place [53];

- inhomogeneous flux distributions within the ablation plume leads to a restricted area onto which an homogeneous deposition is obtained (~ 1 cm^2). This issue can be partially overcome by misaligning the roto-translation of the substrate with respect to the target.

The PLD system used in this work consists of a solid state Q-switched Nd:YAG nanosecond-pulsed laser (second harmonic at $\lambda = 532$ nm, repetition rate $f_p = 10$ Hz and pulse duration 5-7 ns). All films were grown in oxygen atmosphere at room temperature on Si (100) (Siegert Wafer), soda-lime glass (Marienfeld) and FTO-coated glass (Sigma-Aldrich) by ablating a MnO 99.99% purity target supplied by Testbourne B.V. Both the target-to-substrate distance and the laser fluence were fixed, respectively at $d_{T\text{-}S} = 5$ cm and $F \sim 2$ J/cm^2, while the background O$_2$ pressure was varied between 1 Pa to 100 Pa.

2.2. Thermal treatments

As already mentioned in the previous section about PLD, the possibility to perform post-deposition annealing treatments opens the way to the production of materials with tailored morphology and phase.

In this work different conditions of annealing (temperature, time and atmosphere) were investigated, therefore two different systems were employed. A Lenton Muffle furnace (ECF type, maximum operating temperature of 1200°) was employed for air annealing (Figure 2.4a). The treatments were performed in a temperature range $300 - 900°$ for times ranging from 2 to 4h (4°C/min heating ramp); annealing temperature, dwell and heating ramp were set up with a PID controller (Lenton type 3216). Two side wall-heating elements manufactured from high temperature resistance wire spirals embedded into cast refractory slabs provide temperature uniformity while an insulating door separates the annealing chamber from the outside environment [54].

Annealing in vacuum was carried out at 500°C for 1h in a home-made furnace (Figure 2.4b), equipped with a high-vacuum chamber (base pressure $\sim 4.5 \times 10^{-5}$ Pa, 10°C/min heating ramp) connected to a pumping system, and a heater stage connected to a PID controller (Yudian AI-518P). The temperature is simultaneously measured by a thermocouple directly inserted in the heating stage and by an IR pyrometer. A molybdenum shield, covering the heating element, can be installed to reduce the irradiated power, keeping the other components safe and to ensure a more uniform temperature distribution. This system can reach very high temperatures (i.e. maximum operating temperature is 1200°C) with heating ramps up to 100°C/min [54].

(a)

(b)
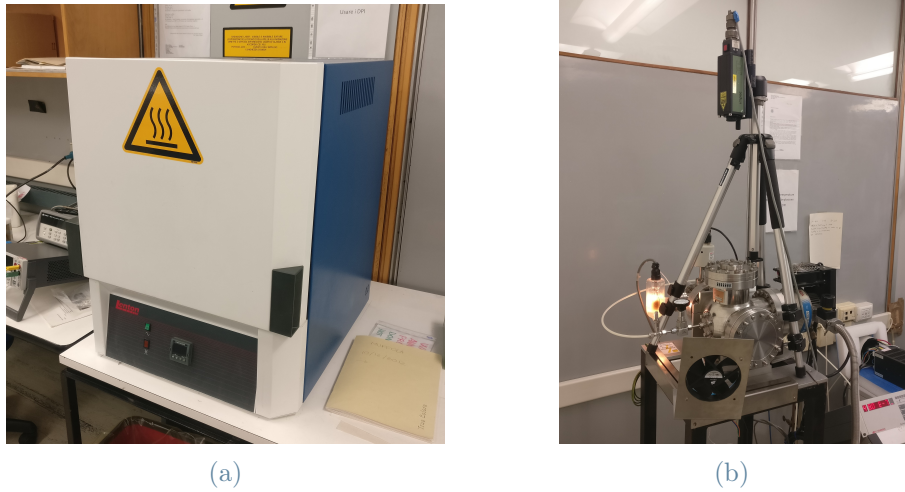
Figure 2.4: Experimental setup used for annealing treatments. Lenton Muffle furnace for annealing in air (a); home-made furnace for annealing in vacuum (b).

2.3.   SEM and EDXS

2.3.1.   Scanning Electron Microscopy

For the purpose of a detailed microstructure and morphology characterization of the deposited films , Scanning Electron Microscopy (SEM) was used. This kind of microscope can provide highly magnified (from 10x to $300\,000$x) images with high spatial resolution ($1-10$ nm) and large depth of focus (4 mm-0.4 μm) [55].

A schematic representation of the instrument is shown in Figure 2.5 while the working principle is presented in the following. Under vacuum conditions (about 10^{-5} mbar), a monochromatic electron beam, generated by thermoionic effect or field emission, is accelerated by a potential (0.2 - 30 kV) and focused onto the surface of the sample by means of electromagnetic focusing lenses. Here, incident electrons penetrate within the solid sample and are subjected to elastic and inelastic scattering or induce emission of photons. These interactions produce emission of secondary electrons (SE), backscattered electrons (BSEs) and X-Rays respectively, which are then collected by appropriate detectors and converted into electrical signals to produce a greyscale image of the sample. Therefore, SEM allows the acquisition of three types of images: 3D secondary electron images, 2D backscattered electron images, and elemental X-ray maps which can be obtained by Energy Dispersive X-Ray Spectroscopy (EDXS) presented in the following [51, 53, 55] (see subsection 2.3.2).
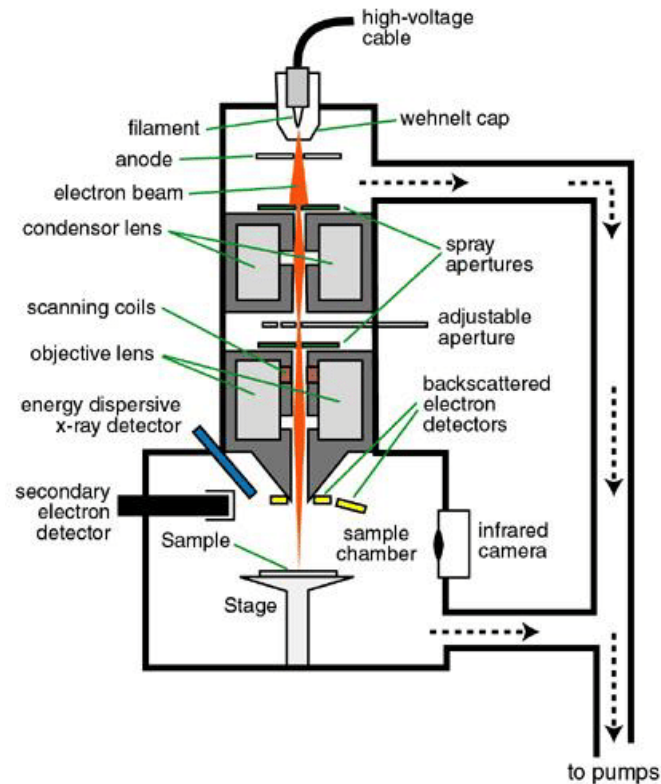
Figure 2.5: Schematic representation of a SEM apparatus. Taken from [56]

In this study, two types of detectors for secondary electrons were used: the "In-lens" SE detector placed in the upper part of the electromagnetic collimator, and the traditional SE detector (Everhart-Thornley (ET)) positioned outside the lens system. The former is able to detect electrons which are emitted with high angle from the upper range of the interaction volume and therefore contain direct information on the sample surface (SE1). As a result, high resolution images can be obtained. On the other hand, the traditional ET SE detector picks up not only SE1 electrons, but also electrons emitted at low angle and generated in a wider and deeper volume (SE2), which carry depth and surface morphology information. Images acquired from ET SE detector have less resolution, but carry more information about the topography of the surface [57]. Figure 2.6 shows a schematic illustration of the detection principle just discussed.

In conclusion, SEM analysis requires little sample preparation: the sample must be conductive, vacuum compatible and have a proper size to enter the specimen chamber and fit onto the stage [55].

For this project a Field Emission Zeiss SEM SUPRA 40 based on a GEMINI column was used to obtain nanometric resolution images both of the top surface and cross-section of the samples.
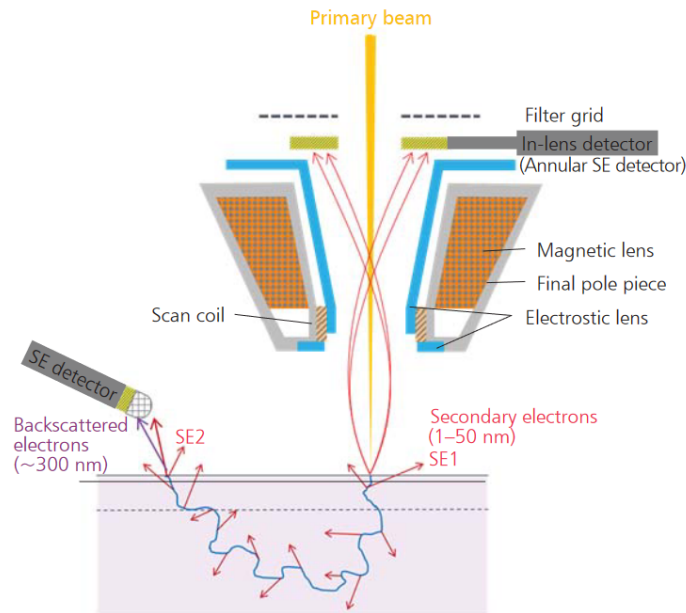
Figure 2.6: Principle of SE signal detection. Taken from [57]

2.3.2. Energy Dispersive X-Ray Spectroscopy

The SEM apparatus previously discussed is also equipped with an X-Ray detector for microanalysis. Energy Dispersive X-Rays Spectroscopy (EDXS) is an established technique used to characterise the elemental composition of a sample by exploiting the X-Ray emission generated by the interaction between the electron beam and the sample [58].

The detector for EDXS analysis, depicted in Figure 2.7, is composed by [58]:

- a *collimator* which ensures that only X-Rays coming from the area being excited by the electron beam are detected;

- an *electron trap* aimed to deflects any passing electrons which are cause of background noise;

- a *window* that provides a barrier to maintain vacuum within the detector while being as transparent as possible to low energy X-rays. Two main types of window materials can be used. Beryllium (Be) is highly robust but strongly absorb low energy X-rays limiting the analysis range of the detector to elements having atomic number $Z > 10$. To overcome this problem polymer-based thin windows can be used;

- a *sensor* which is a semiconductor device that trough ionization converts X-rays into electrical signals. Two main types of sensors are used for X-rays detection:

traditional silicon crystal drifted with lithium ('Si(Li)'), and Silicon Drift Detectors (SDD) which have largely replaced them;

- a *Field Effect Transistor* (FET) directly connected to the sensor that measures the charges present in the crystal after the interaction with an incident X-ray and converts it to a voltage output;

- a *cooling system* made by a Peltier cooling thermoelectric device aimed to maintain the detector at a few tens of degrees below zero.
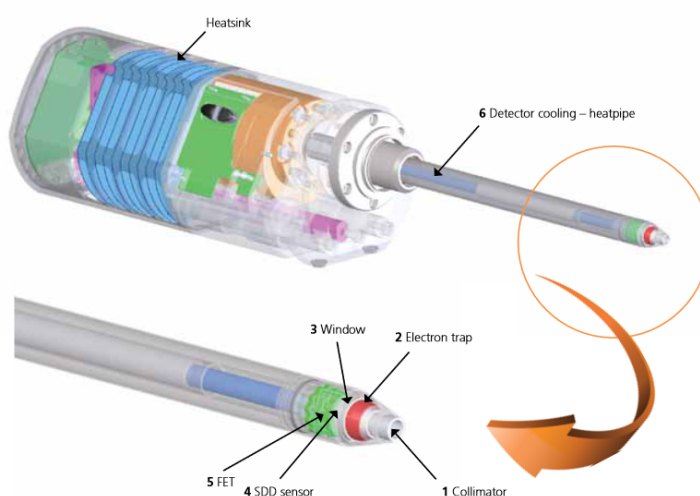
Figure 2.7: Schematic representation of a SDD X-Rays detector. Taken from [58].

The working principle is the following. When a bias is applied and the detector is exposed to X-rays coming from the sample, an ionization process occurs and each X-ray is converted into an electron cloud with a charge proportional to the characteristic energy of that X-ray. This charge is then collected at the anode and converted into a voltage signal by the FET and finally input into the pulse processor for measurement [58].

Three modes of analysis are commonly used [59]:

1. *Spectrum acquisition.* The probe is fixed in the spot mode at high magnification and a complete spectrum is acquired. The output is an energy histogram;

2. *Spatial distribution/Dot mapping of the elements.* Data from more than 15 elements can be collected simultaneously and used to generate X-ray dot maps displaying the spatial distribution of the elements in the sample. Long data collection time is often required to collect enough data points for a high-resolution dot map;

3. *Elemental line scans.* For reasons of time, it is often more useful to scan one line on

a sample. This mode of display will usually show minor concentration differences much better than the brightness modulation technique used in mapping.

The energy resolution is defined as the full width at half maximum (FWHM) of the peak obtained. Ideally this width would be very small but due to the statistical nature of the process and background noise [58], fluctuations will occur in the measured energy of the X-rays. From this poor resolution follows one of the major problem in EDXS called peak overlap (two peaks of about the same amplitude are separated by less than half of the FWHM of the peaks). This presents problems not only for the identification of the individuals peaks but also for the determination of the amplitudes for quantification [59]. For this reasons, the accuracy of the composition measurements is not so high (some %), especially in the case of element with low atomic number ($Z < 10$) (e.g. oxygen). Almost any size solid sample can be studied but a highly polished surface is required for accurate quantitative analysis since surface roughness will cause undue absorption of the generated X-Ray signal [59].

For EDXS analysis of this work, an Xplore EDS detector (Oxford Instruments) and the AZtecLive software tool were used.

2.4.   X-Ray Diffraction

X-ray Diffraction (XRD) is a powerful non-destructive technique for uniquely identify crystalline phases and measure structural properties (strain state, grain size, epitaxy, phase composition, preferred orientation and defect structure) of materials. XRD also provide quantitative, accurate information on the atomic arrangements in amorphous materials (including polymers) and at interfaces. Sensitivity of XRD depends on the material (most sensitive to high-Z elements due to the higher diffracted intensity) but in principle materials composed of any element can be successfully studied [60].

The basic principle of XRD relies on elastic scattering of X-ray photons by the periodic arrangement of atoms within a crystal and on their constructive interference. X-rays are generated by collision of high-speed electrons, usually coming from a hot W filament, and a metal target (e.g., Cu, Co). When the X-ray beam impinges the surface of the sample, diffraction may occur. Because of the interaction with the electromagnetic radiation, atoms within the crystal become secondary sources of spherical waves that come out from the sample in all directions. For specific values of the incident angle θ the scattered waves interfere constructively and the signal is recorded by an X-ray detector which move along a semicircle around the sample [61]. This configuration is typically used for single-crystals and powders.
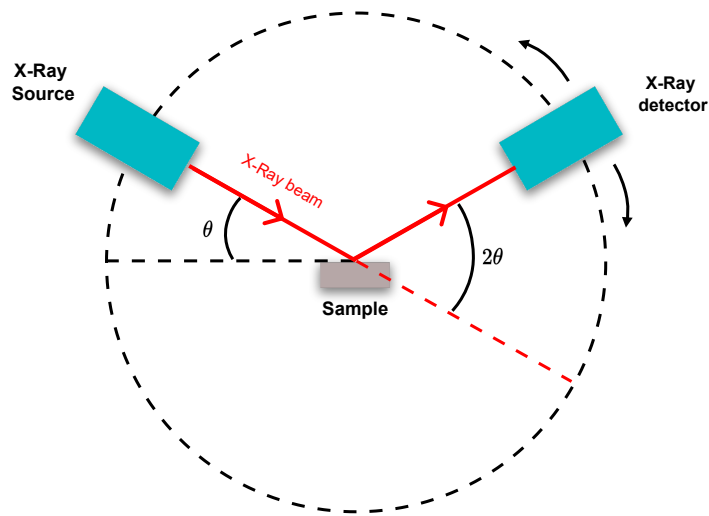
Figure 2.8: Scheme of the XRD geometric configuration.

The position of the detector is determined by the angle 2θ (*diffraction angle* [60]) and the condition for constructive interference is given by the *Bragg's law*:

$$n\lambda = 2d_{hkl}\sin\theta \qquad (2.1)$$

where n is an integer number also called *order of reflection*, λ is the wavelength of the incident radiation and d_{hkl} is the characteristic distance between crystal planes of the same family defined by the Miller indices hkl.
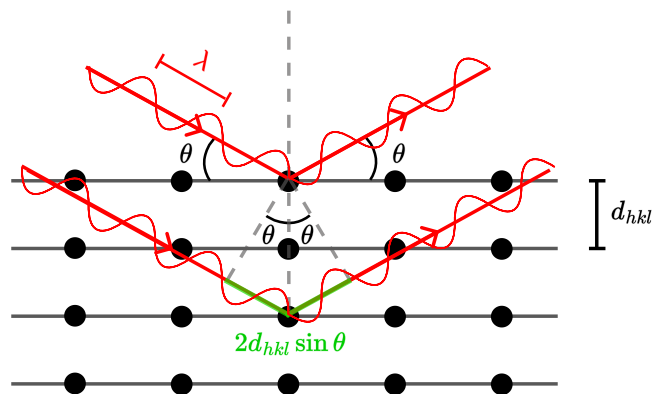
Figure 2.9: Schematic representation of the XRD principle. Bragg's law: *constructive interference occurs when the optical path difference is an integer multiple of the wavelength.*

The X-rays energy is around ten KeV, which corresponds to wavelength in the order of few Å so as the interatomic distance [60]; this condition is required in order to have

interference. The use of a synchrotron radiation allows the characterization of much thinner films, and for many materials, monoatomic layers can be analyzed [60].

The diffraction pattern is a product of the unique crystal structure of the material. Therefore, by comparing the diffraction pattern to a database of known patterns, chemical identification can be performed. Amorphous materials are not characterized by a long-range atomic order and so they do not produce a diffraction pattern.; their X-ray scattering pattern features broad and poorly defined "humps". The presence and position of diffraction peaks are mainly determined by crystal structure, lattice parameters and symmetry, while their intensity is related to the atomic arrangement within the unit cell, and so to the amount of radiation reflected at each diffraction angle. Therefore, since each diffraction peak is attributed to the scattering from a specific set of parallel crystallographic planes, XRD is frequently used to identify and quantify the different phases present in a sample [61].

Thin films can consist of many grains or crystallites (small crystalline regions) having an often random distribution of orientations. Therefore, they form a class of materials intermediate between single crystals and powders. However, the orientation of crystallites in a thin film can vary from epitaxial (single crystalline), to complete texture, to preferred orientation (incomplete fiber texture), to randomly distributed (powder). The degree of orientation not only influences the thin-film properties but also has important consequences on the method of measurement and on the difficulty of identifying the phases present in films having multiple phases [60].

Since the diffracting power of thin films is small, instrumentation and techniques for thin-film XRD are designed to maximize diffracted intensities and to minimize background noises. The preferred method for the characterization of thin films is the Grazing Incidence X-ray Diffraction (GIXRD) configuration. Here the incidence angle is small ($\sim 0.5-2°$) to increase the path travelled by the incident X-rays in the film [60].

In this work, the XRD measurements have been carried out in the Laboratory of IMM Agrate UNIT belonging to the Physics and Matter Technologies Department of CNR (National Research Council of Italy), with a A HRD3000 diffractometer (Ital Structures, Riva del Garda, Italy). Measurements were performed in grazing incidence configuration (GIXRD) with an incidence angle of $\omega = 2°$ and a radiation source made of Cu Kα (λ = 0.1541 nm). Data were acquired by a curved position-sensitive multichannel gas-filled detector (2θ range $0 - 120°$, resolution 0.029°, Inel CPS-120).

2.5.   Raman Spectroscopy

Raman Spectroscopy is a widely used non-destructive technique for characterization of materials. Used to investigate the vibrational dynamics of molecules or lattice cells constituting the material, it provides a fingerprint of the molecule or crystal analysed [62]. The technique is based on the *Raman effect* discovered by the Indian physicist Chandrasekhara Venkata Raman (*Nobel Prize in Physics*, 1930) in 1921 which basically consists in inelastic scattering of light: when monochromatic light interacts with a sample, most of the radiation is scattered elastically (Rayleigh scattering: constant energy and frequency) but a small fraction of photons with different energy (Raman scattering) can be visible. This difference in energy, known as *Raman Shift*, is due to inelastic scattering of photons by phonons [63] and for this reason strongly depends on the position of vibrational levels which in turn is determined by the crystalline structure of the sample [64]. Among the advantages of Raman Spectroscopy we include not only high versatility (almost any material can be investigated [64]) but also high sensitivity to the local bonding between atoms and local order which allows to distinguish crystalline materials from nano-crystalline or amorphous materials.

From the point of view of quantum theory the Raman scattering process in a crystal can be seen as a scattering event between quanta of energy: photons and phonons. The incident photon has an energy $\hbar\omega_L$ while the quantum of vibrational energy is $\hbar\omega_j$. When inelastic scattering occurs, the photon can acquire or lose the vibrational energy $\hbar\omega_j$, so the scattered photon will have energy:

$$\hbar\omega_{sc} = \hbar\omega_L \pm \hbar\omega_j \tag{2.2}$$

If the incident photon loses energy we speak about Raman *Stokes* scattering process, while, if the incident photon acquires energy from the sample, a Raman *anti-Stokes* scattering process takes place. A schematic representation of the process is presented in Figure 2.10: in the Stokes process a phonon $(\omega_j,\mathbf{q})$ is created, while in the anti-Stokes process the phonon $(\omega_j,\mathbf{q})$ is annihilated [63].

The simple quantum model described here accounts for the higher intensity of the Stokes lines with respect to the anti-Stokes lines. This comes from the fact that phonons are bosons and therefore they obey to the Bose-Einstein distribution:

$$n(\omega_j, T) = \frac{1}{e^{\frac{\hbar\omega_j(\mathbf{q})}{k_B T}} - 1} \tag{2.3}$$
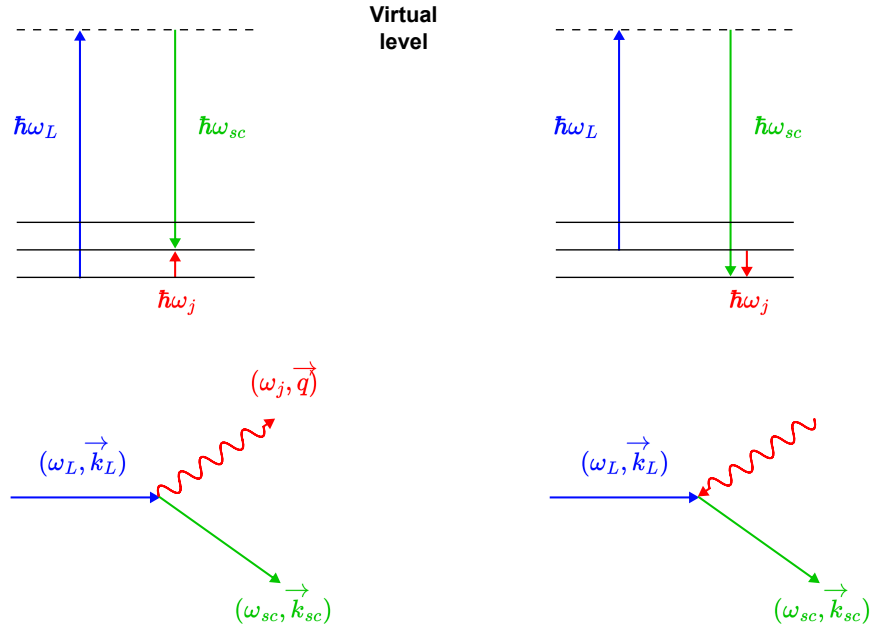
Figure 2.10: Stokes process (left) and Anti-Stokes process (rigth).

This means that tipically, with respect to the temperature, the lower vibrational levels are more populated than the higher ones: the Stokes process is more favored than the anti-Stokes because it starts from more populated states (see Figure 2.10). As a result, the Stokes lines in the Raman spectrum will be always more intense than the anti-Stokes ones (see Figure 2.11); in fact:

$$\frac{I_{Stokes}}{I_{anti-Stokes}} = \frac{(\omega_L - \omega_j)^4}{(\omega_L + \omega_j)^4} exp(\frac{\hbar\omega_j}{k_B T}) > 1 \qquad (2.4)$$
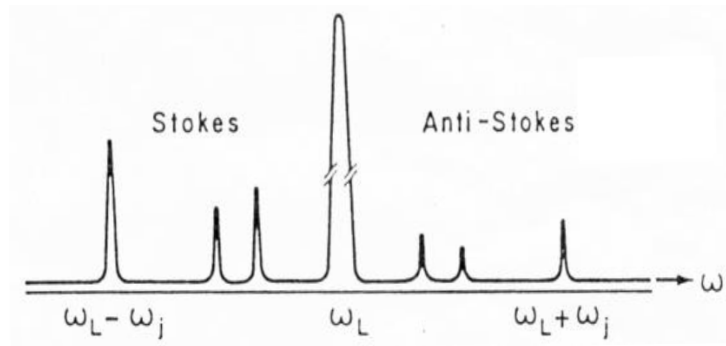
Figure 2.11: Schematic Stokes and anti-Stokes Raman spectrum. The strong line at ω_L is due to Rayleigh scattering. Taken from [63].

In *first-order* Raman scattering only one photon and one phonon are involved. Energy and momentum must be conserved during the process [63]:

$$\hbar\omega_L = \hbar\omega_{sc} \pm \hbar\omega_j(\mathbf{q}), \tag{2.5}$$

$$\mathbf{k}_L = \mathbf{k}_{sc} \pm \mathbf{q}. \tag{2.6}$$

Since the typical light source used for Raman spectroscopy is a laser in the visible range, it follows, from equation (2.5), that the scattered photon will have a frequency comparable with the incident one:

$$\omega_L \gg \omega_j \quad \Rightarrow \quad \omega_L \cong \omega_{sc} \tag{2.7}$$

From this approximation follows also that $\mathbf{k}_L \cong \mathbf{k}_{sc}$, meaning that in first-order Raman scattering only $\mathbf{q} \cong 0$ optical modes at the center of the Brillouin zone can be excited [62, 63]. This selection rule is relaxed for *higher-order* Raman scattering (multi-phonon processes): phonons can be from the entire Brillouin zone, provided that the vector sum of their wavevectors is close to zero (energy and momentum must be conserved) [62].

The Raman apparatus is schematically presented in Figure 2.12. The laser is focused on the sample by some optics (microscope, macroscopic optical paths, ...). After the interaction with the sample, the scattered light is collected by lenses onto the entrance slit of the double-grating spectrometer which acts as a tunable filter of extremely high contrast. Its tandem mode of operation is required to prevent the internally scattered intense Rayleigh light from overpowering the weak Raman lines [63]. Typically the output spectrum represents the Stokes part of the Raman spectrum, even if we plot it with positive frequency.
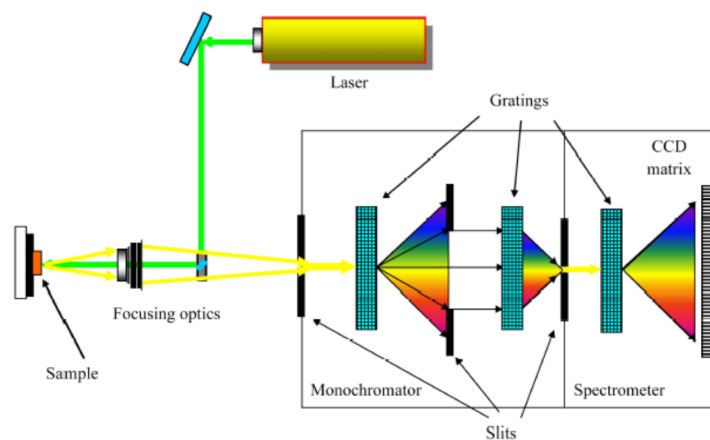
Figure 2.12: Schematic representation of a Raman spectrometer. Image taken from Prof. C. Casari's lecture notes.

In this work, different Raman spectrometers were used:

1. Renishaw InVia micro-Raman spectrometer, equipped with optical microscope. An argon ion source emitting green (514 nm) and blue (457 nm) was employed. The Raman spectra were collected using the 1800 l/mm and 2400 l/mm gratings, respectively, for the green and blue lasers, and with the 50x optical objective.

2. Renishaw InVia micro-Raman spectrometer equipped with a remote Raman probe and optical microscope (50x objective). Two diode-pumped solid-state lasers were employed: 532 nm (green) and 660 nm (red), with 1800 l/mm grating.

2.6.   UV/Vis Spectroscopy

Ultraviolet-visible spectroscopy is an analytical technique that exploits absorption of radiation in the UV-VIS range to provide information about electronic transitions occurring in the material. Selection rules can help one predict which transitions are allowed or forbidden and information about the electronic structure of a compound can be obtained [64, 65]. A spectrophotometer is employed, meaning an instrument able to measure the intensity of light at different wavelengths.
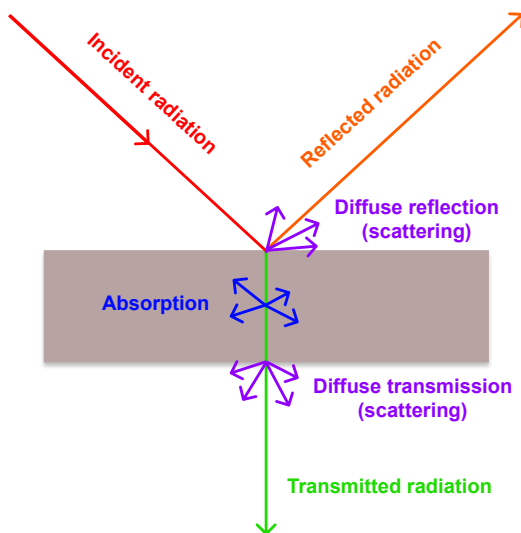
Figure 2.13: Schematic representation of light-matter interaction.

After the interaction with the sample (Figure 2.13), the electromagnetic radiation beam will suffer from:

- *Transmisson*: part of the radiation passes through the sample without interacting;

- *Reflection*: part of the light can be reflected back from the top surface of the sample;

- *Absorption*: due to electronic transitions some light may be absorbed by the sample;

- *Scattering*: radiation losses due to scattering events at the surface and volume imperfections.

The sum of the intensities of all these contributions should be equal to the intensity of the total radiation:

$$T + R + A + S = 1 \tag{2.8}$$

Several UV-Vis configurations are available. In this work transmission, both with and without integrating sphere, and diffusive reflectance were measured. The experimental setups are schematically shown in Figure 2.14.
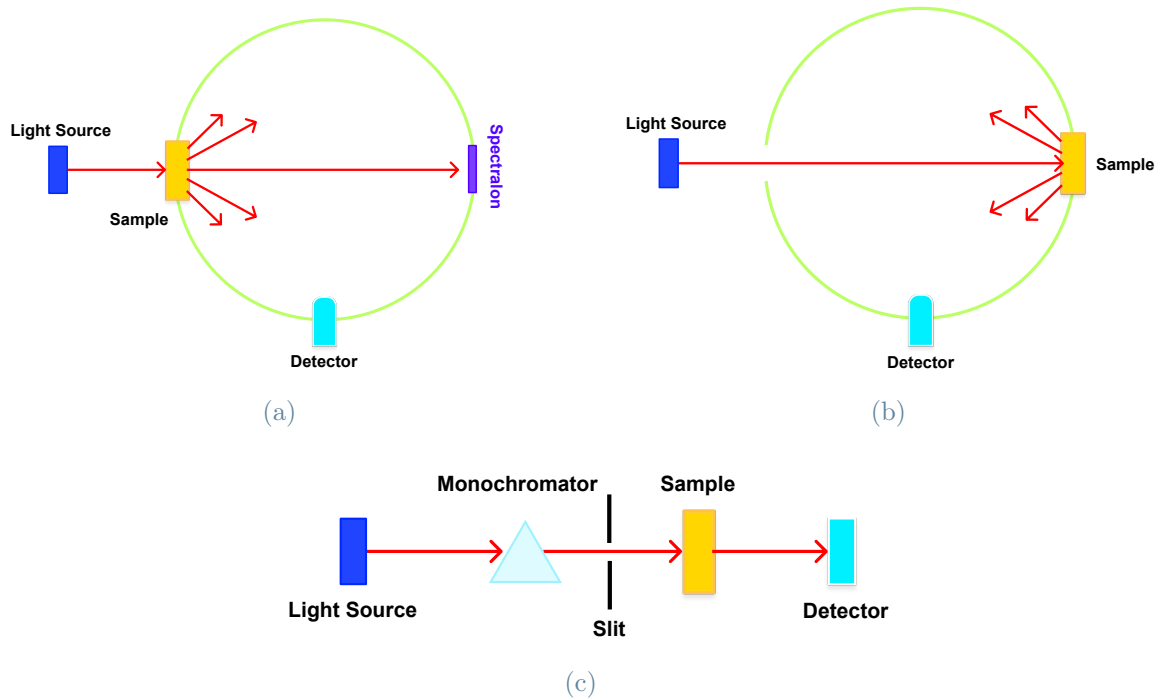
Figure 2.14: Schematic representation of experimental setup for optical measurements. Diffuse transmission with the presence of an integrating sphere (a); diffuse reflectance with integrating sphere (b); direct transmission (c).

In general, transmission mode is used for samples that have some degree of transparency, namely, often thin films supported on transparent substrates. For opaque samples a diffuse reflectance configuration is used. Diffuse reflectance is also the configuration of choice for powders and grains, since the larger acceptance angle of the integrating sphere can potentially provide greater signal compared to transmission measurements where much of the signal will be scattered off-axis [65].

Most of the transmittance measurements of MnO_x thin films have been performed at the Micro- and Nanostructured Materials Lab (NanoLab) at the Department of Energy of Politecnico di Milano with a UV-1800 UV-VIS Shimadzu spectrophotometer within the wavelength range 190-1100 nm and with data scanned every 0.2 nm. The absence of the integrating sphere may contribute to an underestimation of transmittance values: just light reaching the detector, placed behind and perpendicular to the sample surface, can be collected (Figure 2.14c) and the diffused transmittance contribution is lost [51]. More accurate measurements have been performed, both in transmittance and in reflectance configuration, at the Centre for Nanoscience and Technology (CNST) of the Italian Institute of Technology (IIT) in Milan using a LAMBDA 1050 UV/Vis/NIR spectrophotometer with Perkin Elmer 150 mm integrating sphere coated by Spectralon (250-2000 nm range, 2nm interval). Here the sample, with the film facing inside, is placed at the entrance of the integrating sphere while the opposite side of the sphere is closed (or not) by a Spectralon disk, a material able to completely reflect light at any wavelength (R $\sim$ 100%). If the hole is closed, all the light passing through the sample is collected by the sphere and total transmittance is measured, Figure 2.14a. In the same configuration but with the hole left open, only diffusive transmittance can be measured, since the radiation that is not diffused goes straight out of the sphere and it is lost. To measure diffuse reflectance, the setup shown in Figure 2.14b is used.

In any case, the effect of the substrate must be taken into account: both transmittance and reflectance values are normalised with respect to the substrate optical response according to the following relations.

$$T_{film} = \frac{T_{film}}{T_{substrate}} \tag{2.9}$$

$$R_{film} = R_{tot} - (R_{substrate} * T_{film}^2). \tag{2.10}$$

2.7.   Cyclic Voltammetry

The Ciclic Voltammetry (CV) technique was adopted for preliminary electrochemical studies of the MnO_x films produced during this work, in order to try to understand the basic operating principles and the redox mechanism of the material. Ciclic Voltammetry is the most important potential technique for electrochemical measurements, in which the current response at different applied potentials is recorded and information on the redox response of the material in the selected potential range can be obtained. It should be noted that, since the applied perturbation (voltage or current) is high, data collection in the CV is usually done in a non-equilibrium state [66].

CV tests were performed within the Solid-Liquid Interface Nanomicroscopy and Spectroscopy Lab (SoLINano-Σ) at the Physics Department of Politecnico di Milano using a PalmSens4 potentiostat/galvanostat/impedance analyzer. A typical half-cell three-electrode configuration was used: the external potentiostat imposes the potential with respect to the reference electrode (Pt-QRef wire, +445mV vs. Ag/AgCl) and measures the current circulating between the working electrode (the MnO_x film) and the counter electrode (another Pt wire). The potential is linearly scanned forward and backward within a voltage range between E_1 and E_2, giving a triangular potential cycle as shown in Figure 2.15a.

<table>
<tr><td>(a)</td><td>(b)</td></tr>
</table>
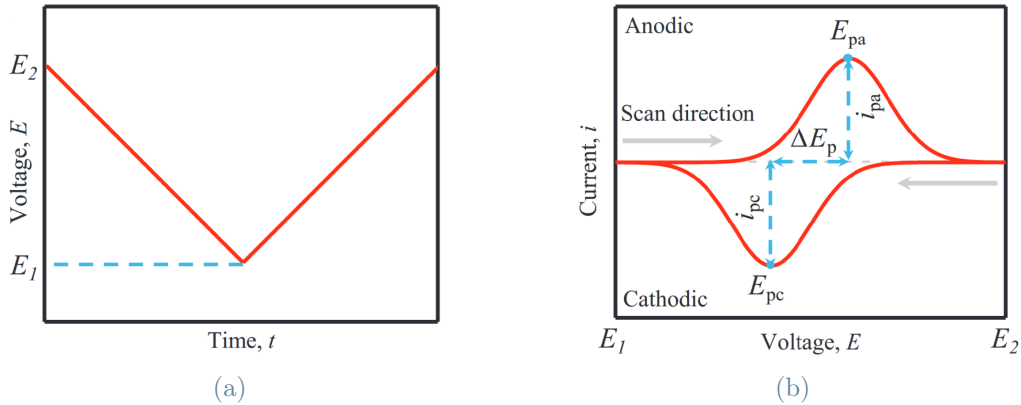
Figure 2.15: CV measurement: voltage profile applied (a) and current response versus voltage curves (b). Taken from [66]

The actual process involves solid-liquid interface phenomena, ion diffusion and multiple reactions [66] which are far from this thesis objectives. In practice we can just identify some specific values collected from CV curves that, in addition to the overall CV shape, are useful to understand the electrode reactions [66]. To perfom a CV measurement we need to determine the terminal potentials (E_1 and E_2) and the scan rate (ν). The terminal potentials define the *electrochemical window* in which the potentiostat spans and they are set with respect to the reference electrode, while the scan rate refers to the velocity at which the imposed voltage goes from one extreme to the other [53]. These two parameters are typically chosen according to the following criteria [66]:

1. the electrochemical window chosen should be the one in which the electrode reactions occur, and current should drops to almost zero at ending points;

2. the integral capacity at the selected scan rate should be close to the theoretical capacity of the electrode materials.

Due to the latter criterion, not too fast scan rates should be chosen, otherwise the reaction will not occur. The scan rate is usually in the range of $0.1 - 10$ mV/s which is quite slow. However, in practice, the scan rate cannot be too slow because of equipment detection limit, limited measurement time and the fact that, under condition of very slow scan rate, charge carriers diffusion is not the limiting factor [66].

A typical CV output plot is shown in Figure 5.4. When the current is positive, oxidation occurs and anodic peaks appear (upper part of the plot in Figure 5.4). For negative current instead, reduction occurs and cathodic peaks become evident (bottom part of the plot in Figure 5.4) [67]. For each reaction we obtain one Gauss-type peaks from which we can easily identify voltage peak (E_p) and current peak (i_p). The ratio of peak currents and the difference of peak voltage (ΔE_p) in cathodic (denoted by the subscript c) and anodic (denoted by the subscript a) segments can be used to judge whether the electrochemical system is reversible [66]. For a reversible process, the cathodic and anodic peak currents are equal in magnitude ($|i_{pc}| = |i_{pa}|$) and the cathodic peak potential (E_{pc}) is ($58/n$) mV more negative than the anodic peak potential (E_{pa}). If the difference between the two peak potentials increases, the reversibility of the process decreases and if the process is completely irreversible, the anodic peak does not appear in the measurable potential region [67]. However, when the electrochemical behaviour is more complex and involves multiple redox reactions coupled with phase changes, intercalation, and chemical reaction, the overall CV shape can differ significantly from the ideal case.

3 | Synthesis and characterization of as-deposited MnO$_x$ films

In this chapter, after a brief introduction on the optimization of PLD parameters used for the synthesis, characterization of as-deposited MnO$_x$ thin films will be discussed. Morphology and phase characterization will be obtained by SEM, EDX, XRD and Raman spectroscopy analysis. Correlation between the PLD parameters used and the phase and morphology of the deposited films will also be discussed.

3.1. Optimization of PLD parameters

The first section of this chapter is devoted to the optimization of the PLD parameters used for the synthesis. By varying the deposition pressure and the misalignment between the target and the substrate, their influence on the deposition rate, thickness uniformity and morphology of the MnO$_x$ films can be evaluated in order to establish the trends to follow to deposit films with specific thickness and morphology. The average thickness and the thickness uniformity of the deposited films can be evaluated by means of cross section SEM analysis. Since the flux distribution within the ablation plume is not homogeneous, the thickness of the deposited film will be characterized by a "bell-shaped" profile (see Figure 3.1a): higher thickness in the center of the plume and lower thickness in the lateral regions. To obtain films with larger thickness uniformity, it is necessary to offset the target and the substrate in order to obtain a convolution of two bell profiles which corresponds to a larger uniform deposition area (see Figure 3.1b). However, care must be taken not to increase too much the misalignment as this can lead to a thickness profile characterized by hills and valleys (see Figure 3.1c). By our analysis we can state that by increasing the misalignment from 0 mm to 6 mm, and from 6 mm to 9 mm, the thickness uniformity also increases and issues related to non uniform profiles did not occur.

The deposition rate can be easily obtained on the basis of deposition tests done at arbitrary deposition time: once the average thickness is measured, it is sufficient to divide this value by the deposition time. Oxygen pressure values equal to 1 Pa, 10 Pa, 50 Pa and

(a)   (b)   (c)
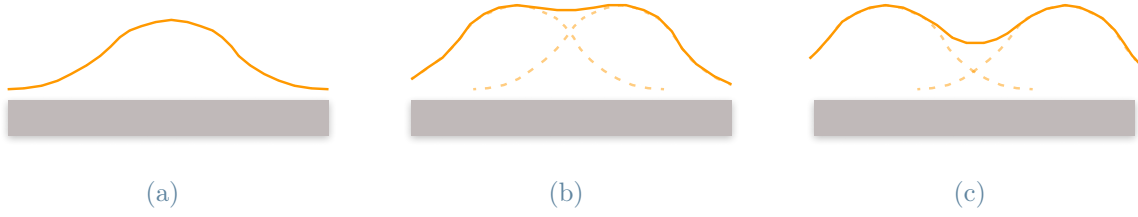
Figure 3.1: Schematic representation of three different thickness profile conditions as a function of the target-substrate misalignment: no misalignment (a), good misalignment (b), and too much misalignment (c).

100 Pa were chosen and the target-substrate misalignment was varied between 6 mm and 9 mm. Deposition rates calculated for each combination of pressure and misalignment are reported in Table 3.1. As we can clearly see from the graph in Figure 3.2, by increasing the deposition pressure, the deposition rate also increases; while increasing the misalignment from 6 mm to 9 mm the deposition rate decreases.

O$_2$ Pressure [Pa]	Misalignment [mm]	Deposition rate [nm/min]
1	6	25
		22
	9	16
10	6	28
	9	21
50	6	53
		65
	9	43
100	6	98
		82

Table 3.1: Deposition rate data for different conditions of O$_2$ pressure (1 Pa, 10 Pa, 50 Pa, and 100 Pa) and misalignment (6 mm and 9 mm).

Based on the deposition rates estimated before, we can grow films with the desired thickness (e.g., 500 nm, as in the following tests) by simply setting the proper deposition time under equal deposition conditions in terms of pressure and misalignment. Other parameters to be mentioned are the laser wavelength, the fluence and the target-to-substrate distance, which were kept constant in all sessions at values of $\lambda = 532$ nm, $F \sim 2$ J/cm^2

and $d_{T-S} = 5$ cm respectively. The fluence value, set by considering a pulse energy $E \cong 118$ mJ and an ablation spot size $S \cong 6$ mm^2, is reasonable with respect to previous literature works [15–20] which report fluence values into the range $2-3$ J/cm^2.
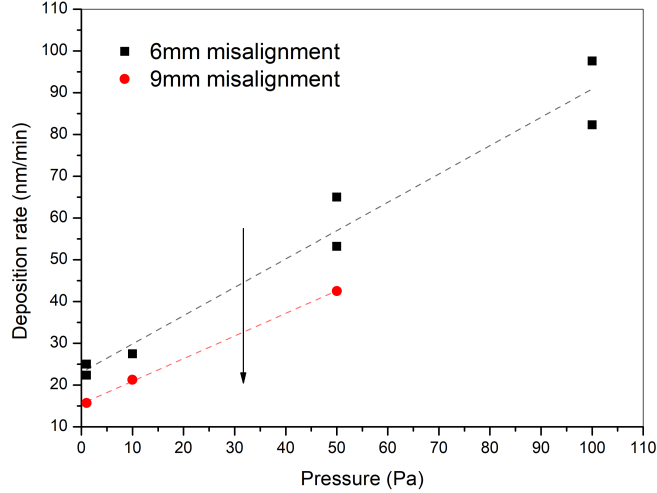
Figure 3.2: Deposition rate trends for different conditions of O$_2$ pressure and target-substrate misalignment.

Finally, it should be emphasized that different types of substrates were used: deposition on glass substrate was required for the optical measurements, while for the electrochemical measurements it was necessary to deposit on conductive FTO-coated glass. Characterization of phases and investigation on the morphology of the MnO$_x$ films was instead conducted on samples deposited on Silicon (100). All samples were deposited starting from a MnO 99.99% purity target supplied by Testbourne B.V.

3.2.   Effect of oxygen pressure on films morphology

In this section, analysis on the effect of O$_2$ deposition pressure on film morphology will be presented. As it can be seen from the cross-sectional SEM images shown in Figure 3.3, as the oxygen pressure increases, the morphology of the deposited film becomes less and less compact, and the nanoporosity gradually increases. Starting from a highly compact structure for the sample deposited at 1 Pa (Figure 3.3a), the morphology of the film evolves in a more "columnar-like" structure by increasing the pressure to 10 Pa (Figure 3.3b). By increasing further the O$_2$ pressure, as we can see from the sample deposited at 50 Pa (Figure 3.3c), the film acquires the tendency to develop "tree-like" structures. Depositions conducted at higher O$_2$ pressures (i.e., 100 Pa, Figure 3.3d) therefore, show an overall structure similar to a "nano-forest" typical of PLD-grown oxides [47, 53, 68–73].
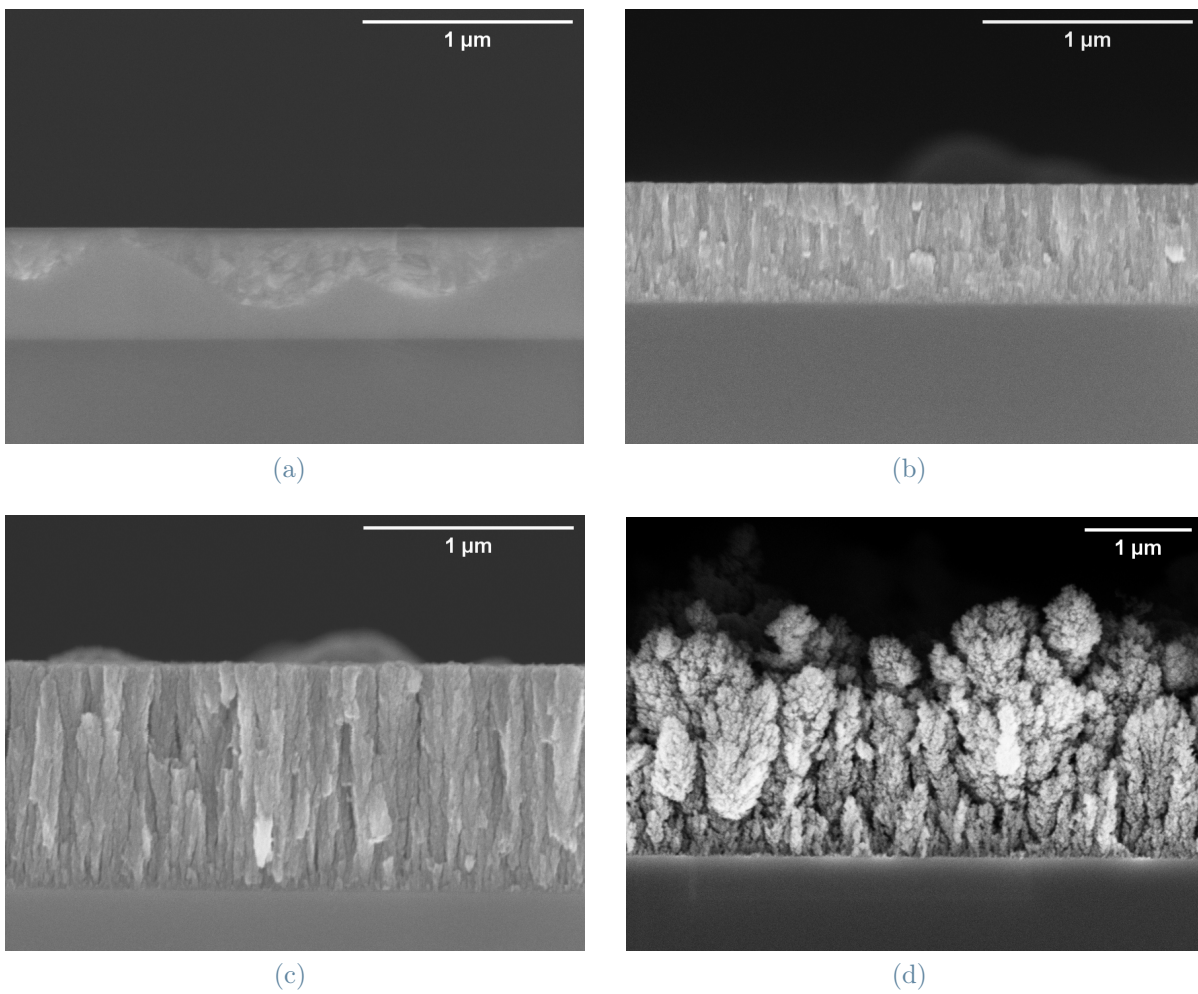
Figure 3.3: Cross-sectional SEM images of MnO$_x$ as-deposited films by increasing background O$_2$ pressure. 1 Pa (a), 10 Pa (b), 50 Pa (c) and 100 Pa (d).

Another important point to be mentioned is the influence of the background O$_2$ pressure on the deposited film thickness. Indeed, all films reported in Figure 3.3 are obtained by deposition sessions at fixed deposition time (i.e., 20 min) and the result is that by increasing the O$_2$ pressure, also the film thickness increases.

The typical "nano-tree" structure can be also seen by the top view SEM images (see Figure 3.4) which show clearly how the evolution of the "tree-like" structure also leads to the onset of many fractures on the film surface.

(a)

(b)

(c)

(d)
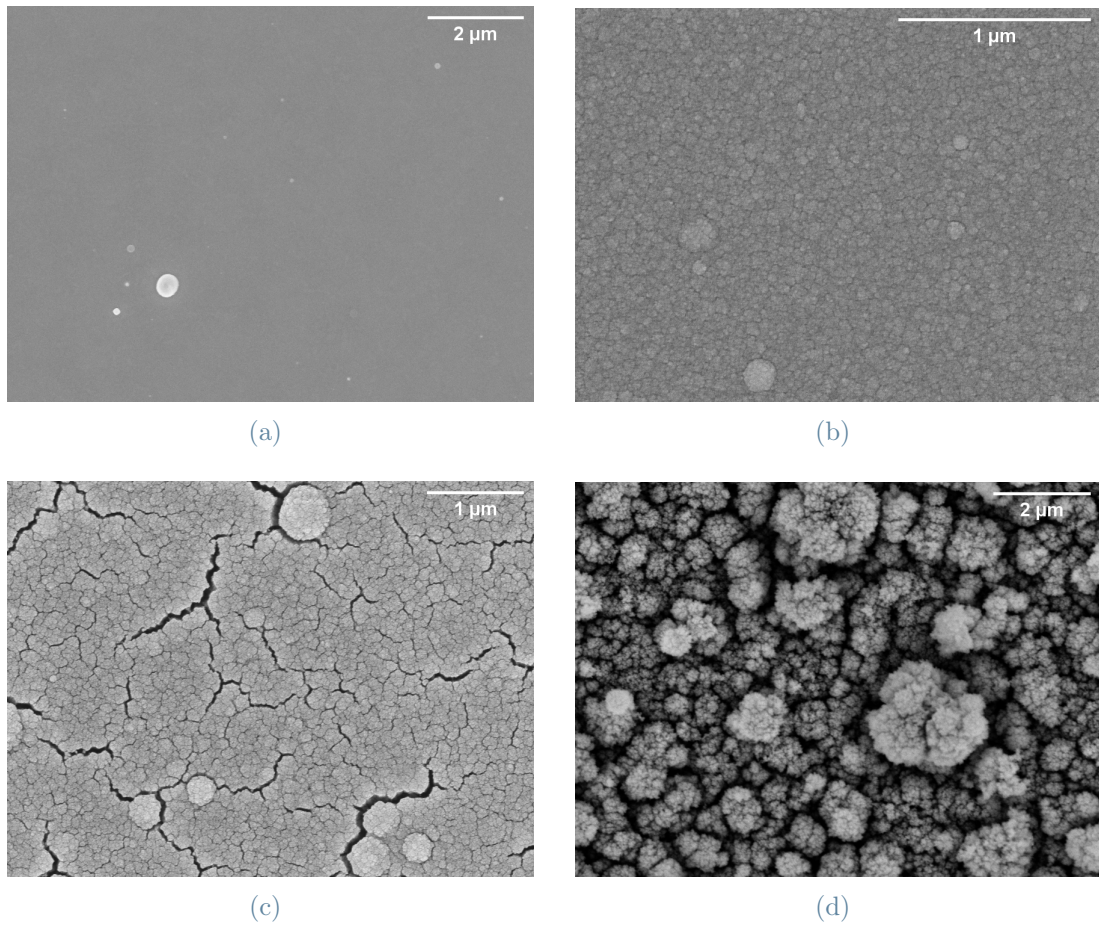
Figure 3.4: Top view SEM images of MnO$_x$ as-deposited films by increasing background O$_2$ pressure. 1 Pa (a), 10 Pa (b), 50 Pa (c) and 100 Pa (d).

3.3. Effect of oxygen pressure on films phase

Given the great variety of existing MnO$_x$ phases, after the discussion on the effect of O$_2$ pressure on film morphology, it is interesting to investigate whether the background gas pressure could also affect the growth of one phase rather than the other.

3.3.1.   Raman analysis

As already mentioned in the section 1.2, Mno$_x$ materials have a rather precarious stability when subjected to the Raman laser beam. The choice of the laser wavelength and power is strictly connected to the reliability of the data obtained: for example, if a too high laser power (or energy) is chosen, the possibility to induce a transformation of the material is extremely high and the correct identification of the MnO$_x$ phase can't be perfomed. Therefore, to be sure our spectra are actually related to the material we want to analyse, and not a result of a wrong choice of the Raman parameters, we conducted detailed investigation of the effect of laser power and wavelength on our MnO$_x$ samples. What resulted is that, in order to obtain satisfactory and reliable data, the correct laser wavelength is the λ = 532 nm. If this type of green laser is chosen, the laser power is not a great issue since material modifications occur at very high powers (i.e., $\sim$ 50mW). The effect of power for the 532 nm green laser is shown in Figure 3.5.
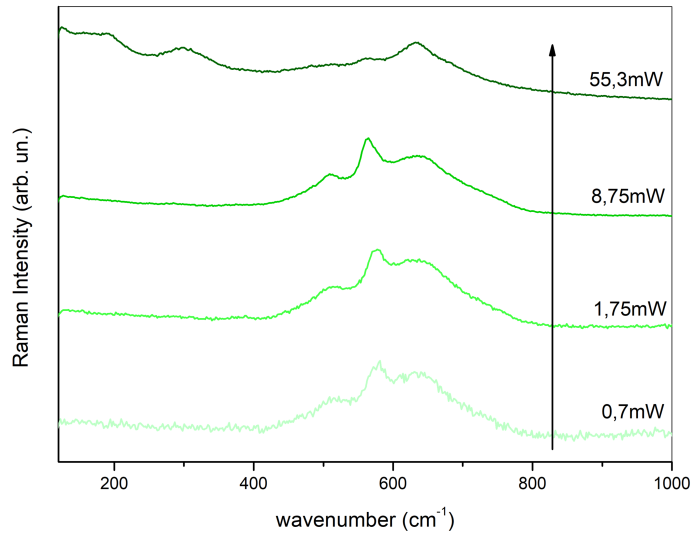
Figure 3.5: Effect of green laser (532 nm) power on as-deposited (50 Pa) MnO$_x$.

Issues related to other investigated laser wavelengths are listed in the following:

1. the red (λ = 660 nm) laser does not allow obtaining satisfactory spectra due to the strong signal coming from the substrate (Figure 3.6). In fact, this laser, poorly absorbed by the MnO$_x$ material due to its small energy, is able to penetrate the thin film and reach the underlying substrate. However, it must be noticed that this is only a technical issue related to the fact that we are analysing thin films with thichknesses of up to 1 μm; if we wanted to analyze bulk samples, powders or films with greater thicknesses (i.e., 100 μm), such problems would not arise;

2. with the green ($\lambda = 514$ nm) laser we encountered problems of visible sample damaging (Figure 3.7b) and material transformation (Figure 3.7a) even for very low powers (i.e., 0.2 mW and 0.39 mW). For this reason this laser was almost immediately rejected;

3. the blue ($\lambda = 457$ nm) laser results to be too energetic, so much so that even at low powers (i.e., 0.67 mW) the sample suffers visible damage (Figure 3.7d). Moreover, spectra acquired with this type of laser are very noisy and trying to overcome this issue by using higher powers is not a good strategy since material transformation occurs (Figure 3.7c).
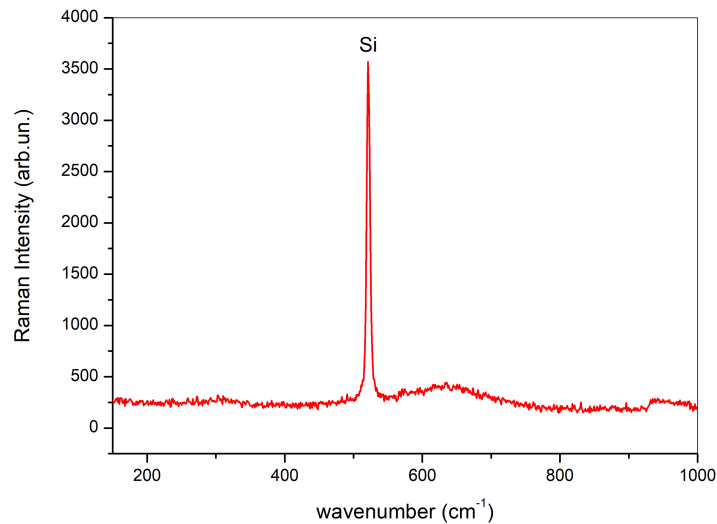
Figure 3.6: Raman spectra of a MnO$_x$ sample deposited at 10 Pa acquired with the red laser (660 nm, 0.754 mW). The strong signal of the substrate (Si) completely overwhelms the MnO$_x$ signal making impossible its phase characterization.

Raman spectra of as-deposited MnO$_x$ films produced at various O$_2$ pressures are shown in Figure 3.8. The spectra shown correspond to the films deposited on silicon and analysed with the green laser (532 nm). All samples, except for the one deposited at 1 Pa O$_2$ pressure, consist in a broad band centered at about 600-650 cm^{-1}, and extending between 400 and 800 cm^{-1}, typical of amorphous manganese oxides (see Figure 3.8b). However, by looking more carefully into these spectra we note that, expecially for the samples deposited at 50 Pa and 100 Pa, this band is actually structured into three peaks. In fact, by performing a multi-peak fitting (see Figure 3.9) using lorentzian curves, three peaks arise at $\sim 501-502$ cm^{-1}, $\sim 564-575$ cm^{-1}, and $\sim 537-538$ cm^{-1} typical of the $\delta-$MnO$_2$ phase according to [27].
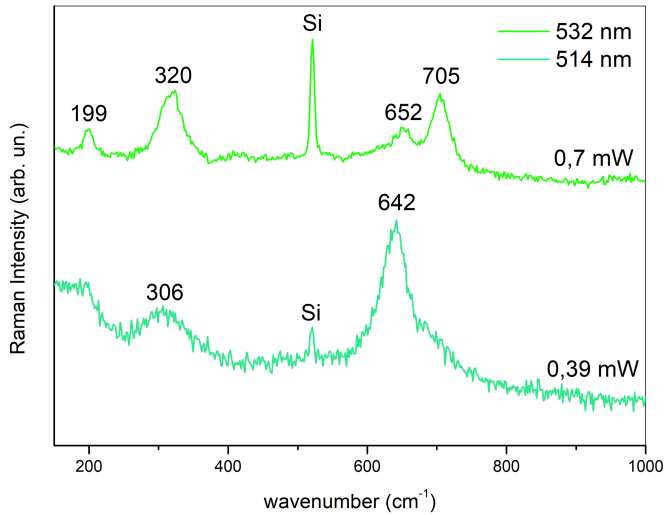
(a) Comparison between spectra acquired with the 532 nm and 514 nm lasers for the same MnO$_x$ sample deposited at 100 Pa and annealed in air at 500°C. The effect of the damage results in a very intense peak at $\sim$ 642 cm^{-1}.
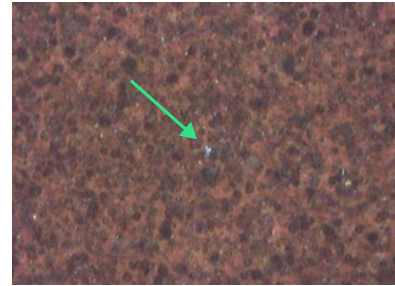
(b) Damaged MnO$_x$ (100 Pa, annealed in air at 500°C) after interaction with 514 nm laser (0.39 mW).
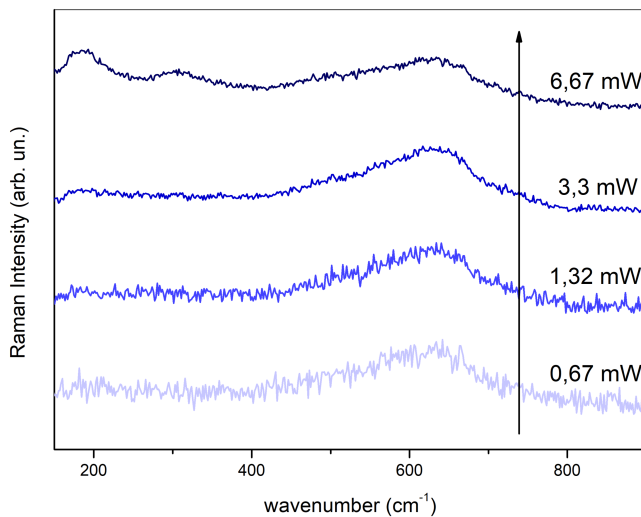
(c) Effect of blu (457 nm) laser power on a MnO$_x$ sample deposited at 10 Pa.
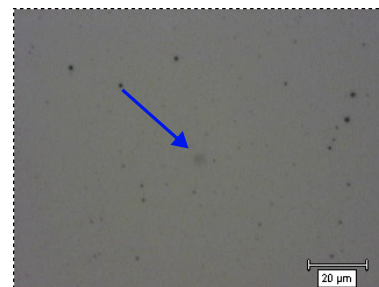
(d) Damaged MnO$_x$ (10 Pa) after interaction with 457 nm laser (0.67 mW).

Figure 3.7: Effect of Raman laser power and wavelength.
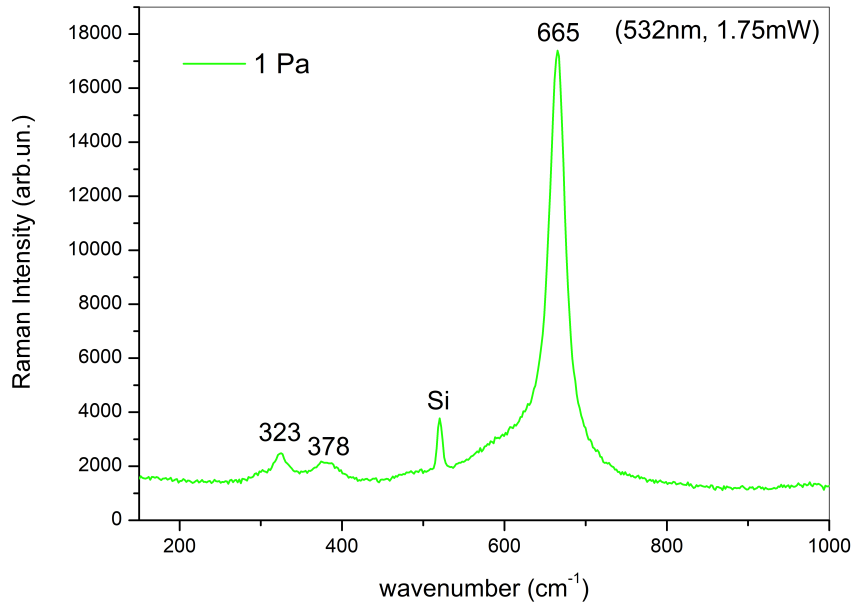
(a)
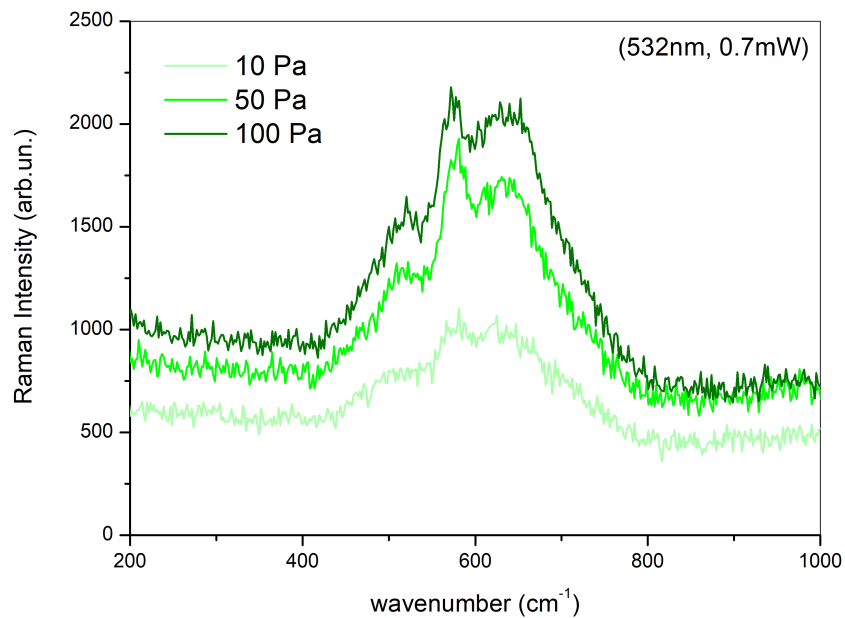
(b)

Figure 3.8: Raman spectra of as-deposited MnO$_x$ (substrate: Si) at different O$_2$ pressures: 1 Pa (a), 10 Pa, 50 Pa, and 100 Pa (b).
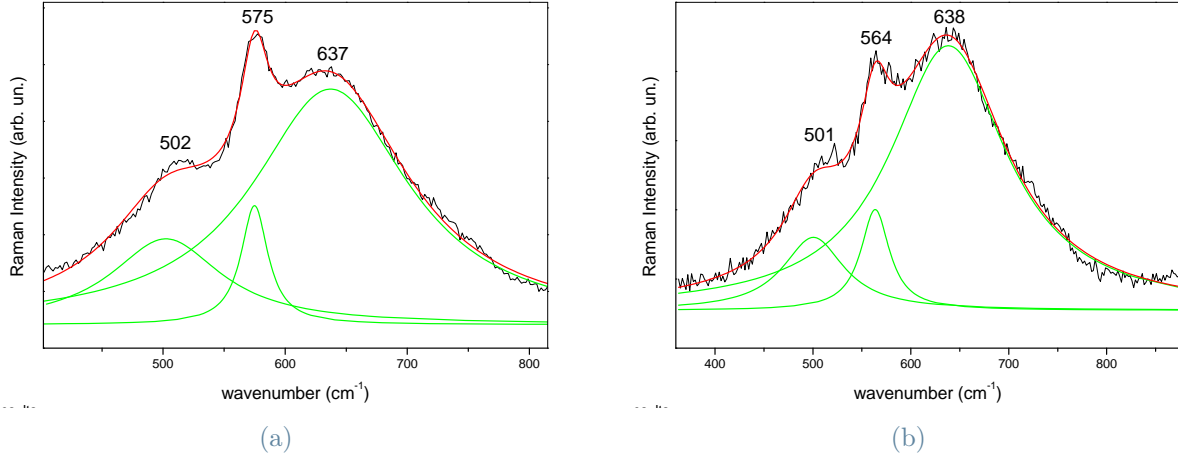
Figure 3.9: Lorentzian fitting of the Raman spectra (532 nm, 1.75 mW) of MnO$_x$ films deposited at 50 Pa (a) and 100 Pa (b).

Therefore, it could be reasonable to assign the amorphous $\delta-\mathrm{MnO_2}$ phase to the samples deposited at 10 Pa, 50 Pa and 100 Pa. Regarding the spectrum of the sample deposited at 1 Pa, reported in Figure 3.8a, it exhibits three peaks at ~ 323 cm^{-1}, ~ 378 cm^{-1}, and ~ 665 cm^{-1}. These well defined (especially the one at ~ 665 cm^{-1}) peaks, are index of a crystalline phase and close to the peaks of Mn$_3$O$_4$ [27].

3.3.2.   EDX analysis

To confirm our assumptions on the basis of Raman analysis, EDX measurements were performed. For each sample five EDX spectra were recorded over several zones and then averaged between them to get a statistical indication. Moreover, to have more reliable data, the manganese-oxygen ratio (Mn/O) of the target was measured, resulting equal to 1.05 and, since the target is known to be stoichiometric (i.e., the Mn/O should be 1), the Mn/O ratio for the samples was normalized to 1.05. The results of EDX measurements are reported in Figure 3.10. As we can see, also EDX data confirm the results from Raman analysis: the element composition of the sample deposited at 1 Pa O$_2$ pressure is compatible with the Mn$_3$O$_4$ phase, while for higher pressures, an element composition in agreement with the MnO$_2$ phase results. It must be emphasised that, given the poor accuracy of EDX measurements, especially in the case of light elements such as oxygen, what is useful to note is the general trend rather than the absolute quantitative data. Further complications come then from the fact that in many spectra the silicon signal was not negligible; this can affect data analysis.
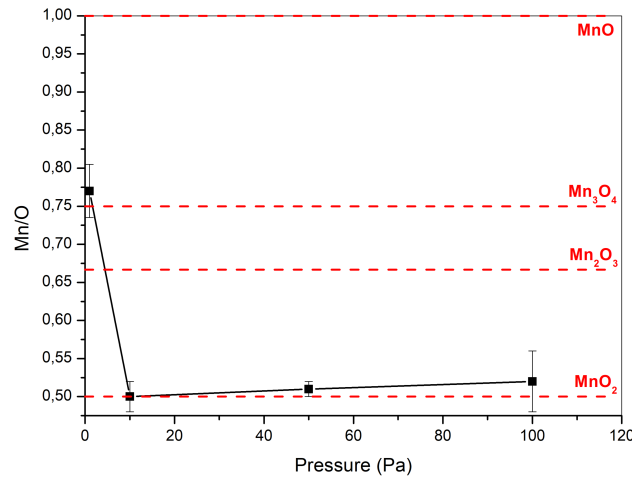
Figure 3.10: Mn/O ratio of as-deposited MnO$_x$ films at different O$_2$ pressures, normalized to the target Mn/O ratio.

3.3.3.   GI-XRD analysis

Further confirmation of results from Raman analysis and EDX measurements, comes from XRD analysis. The diffraction patterns of MnO$_x$ samples, deposited at 1 Pa and 10 Pa, compared with the powder reference patterns of Mn$_3$O$_4$ (card n° 1876, Mincryst database [74]) and $\delta-$MnO$_2$ (AMCSD 0001302, American Mineralogist Crystal Structure Database [75]) are shown in Figure 3.11. In particular, the latter reference pattern corresponds to K-birnessite, i.e., the $\delta-$MnO$_2$ phase containing K$^+$ cations in the interlayer spacing.

The XRD patterns do not produce a clear information about the phase of as-deposited MnO$_x$ films. For the sample deposited at 10 Pa, although the acquisition time was double with respect to the other sample (i.e., 4 hours vs. 2 hours), it is even difficult to speak about a clear pattern, since the resulting curve is highly noisy: no defined peaks are visible, except for a wide peak around 17°. It must be noticed that I was not able to find a XRD pattern for pure $\delta-$MnO$_2$, since the diffraction patterns available are always referred to minerals which contains, by definition, also many other elements (e.g., K, Na, Ca and water) besides manganese and oxygen. On the other hand, the 1 Pa as-deposited sample shows three main broad and asymmetric peaks, that could be assigned to the (101), (112) and (103) reflections of the Mn$_3$O$_4$ phase. However, also in this case the signal-to-noise ratio of the XRD pattern is poor and not all peaks related to the Mn$_3$O$_4$ phase are present (e.g., the one related to the direction (211), which should be also the most intense). Anyway, the bad quality of XRD patterns could be index of low crystalline quality (i.e., poorly crystallized or amorphous material) or of very small crystals. It is worth mentioning that the angular position of the XRD peaks depends only on the
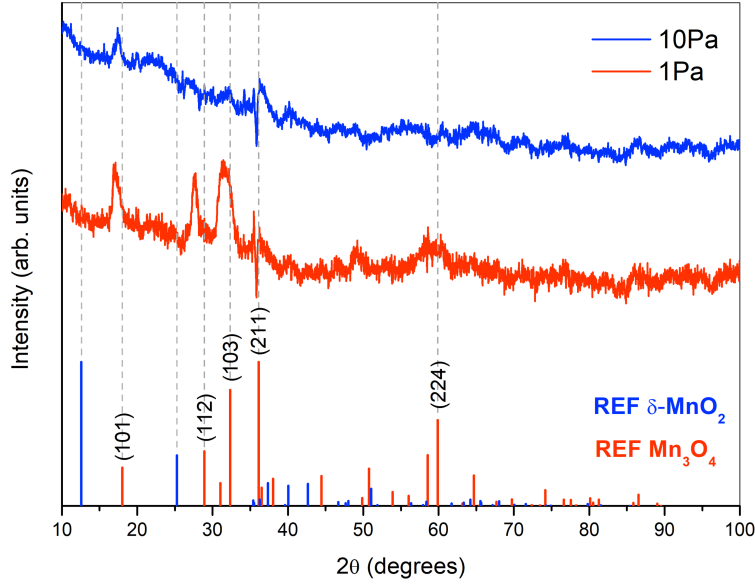
Figure 3.11: XRD patterns of as-deposited MnO$_x$ films at 1 Pa and 10 Pa O$_2$ pressure compared with the reference.

interplanar distance and on the incident wavelength (see Bragg's law in subsection 2.4). Therefore, since the wavelength is fixed, and problems related to the instrument setup are excluded, the angular position of the experimental patterns is influenced only by the lattice parameters. This may mean that the Mn$_3$O$_4$ phase formed is highly distorted or very unordered; this hypothesis is partially confirmed also at short range by the Raman spectrum which, indeed, exhibits a wider and slightly shifted main peak with respect to the one reported by Xin et al. [27]. Moreover, we need to stress that XRD measurements are sensitive to the long range order, while Raman analysis gives information about the short range order. Therefore, the comparison between results obtained with these two techniques can be used to have an idea of how well the material is globally ordered. As last comment, I precise that the artefacts located at ∼36° (present in all patterns) are to be attributed to some technical problems related to the instrument used and not to particular features of the samples.

To conclude, considering the results of Raman, EDX and XRD analysis, we can state that, via PLD depositions in O$_2$ atmosphere, we are able to obtain two different MnO$_x$ phases: nanocrystalline Mn$_3$O$_4$ and some form of amorphous MnO$_2$. Indeed, the hypothesis is that at 1 Pa O$_2$ pressure what we actually obtain is an amorphous matrix in which small crystals of Mn$_3$O$_4$ are dispersed. This would explain the bad quality of the diffraction pattern and it would also be more in agreement with what one would expect from a PLD deposition. Lastly, I observe that, among all the MnO$_x$, the Mn$_3$O$_4$ phase is the one with

the most intense Raman signal. Therefore it is reasonable to think that, even if present in the form of small crystals, its signal dominates on that of the matrix.

3.4. Optical characterization of as-deposited films

To complete the characterization of as-deposited samples, optical measurements conducted on MnO$_x$ films deposited on a glass substrate at different O$_2$ pressures will be presented in this section. Deposition time at any oxygen pressure was set in order to obtain film thickness of $\sim 500-550$ nm. Figure 3.12 shows the direct transmittance results (i.e., neglecting the diffuse component) for the films deposited at 1 Pa, 10 Pa, 50 Pa, and 100 Pa O$_2$ pressure, normalized to the glass substrate.
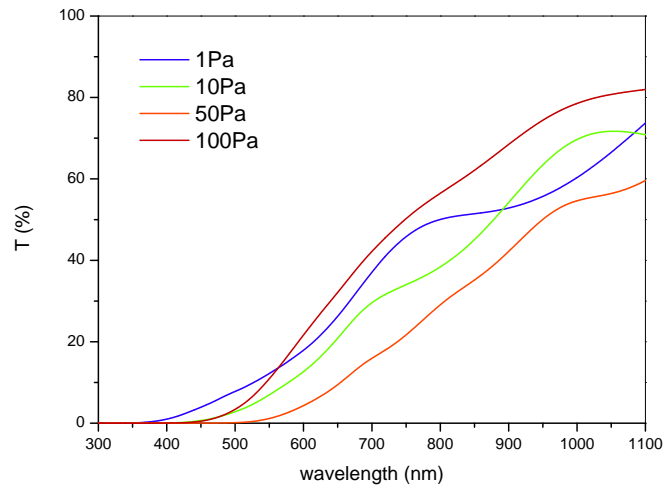
Figure 3.12: Direct transmittance curves for as-deposited MnO$_x$ films at different O$_2$ pressures.

Although we observe that by increasing the O$_2$ pressure from 1 Pa to 50 Pa, the transmittance generally decreases, we cannot find a precise trend for the transmittance of as-deposited films as a function of the deposition oxygen pressure. In particular, the transmittance of the film deposited at 100 Pa of O$_2$ is the highest among all the samples at almost any wavelenght.

To obtain more reliable data, more accurate measurements were performed by means of a spectrometer equipped with an integrating sphere coated by Spectralon. For such detailed analysis, only selected samples (i.e., samples deposited at 1 Pa and 10 Pa), representative of all the phases obtainable via PLD depositions, were chosen. Figure 3.13 shows the transmittance, reflectance, and absorbance optical curves, normalized with respect to the glass substrate and to instrumental corrections, related to the MnO$_x$ films deposited at

1 Pa and 10 Pa oxygen pressure. What we can observe is that these materials exhibits a significant absorbance in the visible region (i.e., from $400-800$ nm), while they are almost transparent in the IR region (i.e., for wavelenghts higher than 800 nm). In particular, the film deposited at 10 Pa shows a wider absorbance tail, as indeed one would expect from an amorphous material.

(a)

(b)

(c)
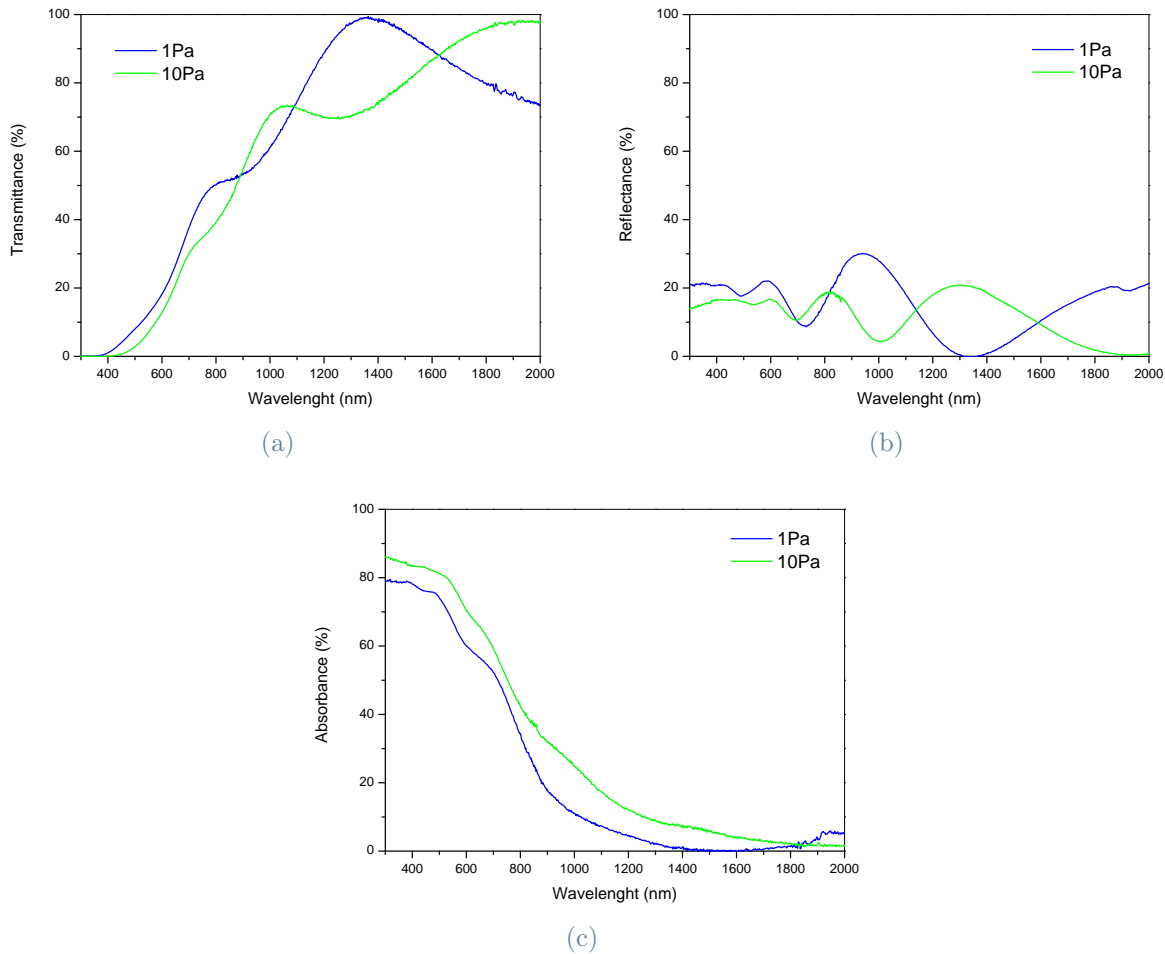
Figure 3.13: Transmittance (a), reflectance (b), and absorbance (c) normalized optical curves related to the as-deposited MnO$_x$ films at 1 Pa, and 10 Pa oxygen pressure.

Since the optical characterization is beyond the scope of this work, our analysis is limited to no more than a qualitative observation of the optical curves. Bandgap of as-deposited MnO$_x$ films has been also tentatively assessed using the Tauc method [76]; however, the amorphous/nanocrystalline nature of the samples led to uncertain results. As regard the optical properties of MnO$_x$ thin films, further extensive analysis are needed but they will not be part of this thesis project.

4 | Characterization of annealed MnO$_x$ films

This chapter will be devoted to the characterization of annealed samples. Since, as discussed in the previous chapter, MnO$_x$ films obtained via PLD are mainly amorphous, thermal treatments were performed in order to obtain crystalline films and try to obtain a decoupled control of the phase and nanoscale morphology/porosity of the films. In particular, the choice of the annealing temperature and atmosphere was discovered to be a key parameter to obtain different MnO$_x$ phases.

4.1. Optimization of annealing conditions

In this first section, annealing parameters and motivations that ruled the choice of such conditions will be presented. Based on previous investigations on this material, we know that the minimum temperature for crystallization is 500°C for 2 hours in air and 1 hours in vacuum. To be sure, also annealing at 300°C for 4 hours in air was performed in order to try to improve the criystalline quality of as-deposited MnO$_2$ films without promoting a phase transition. Finally, thermal treatment at much higher temperature, namely 900°C, for 2 hours in air was also used to check if there could be a phase change. It must be noticed that glass and FTO-coated glass used for optical and electrochemical measurements cannot resist at such a high temperature, since the maximum temperature they can sustain before loosing their mechanical properties is only 550°C. However, I can anticipate that no phase change occurs at a temperature of 900°C and, besides morphological variations, the same MnO$_x$ phase is obtained at both 500°C and 900°C in air. These annealing conditions were tested on samples deposited at 1 Pa, 10 Pa, 50 Pa, and 100 Pa of O$_2$. Table 4.1 shows all combinations of temperatures and times of annealing used for each substrate.

Atmosphere	Temperature [°C]	Time [h]	Substrate
Air	300	4	Si
	500	2	Si glass FTO
	900	2	Si
Vacuum	500	1	Si glass FTO

Table 4.1: Annealing conditions used for each substrate.

4.2. Morphology of annealed films

After annealing, the morphology of the films was studied by SEM analysis. As it would be reasonable to think, the morphology of the MnO$_x$ film changes during the annealing process. Considering the annealing in air, the first noticeable point is the progressive formation of nano-sized grains since from the thermal treatment conducted at lower temperature (i.e., 300°C). Then, by further increasing the annealing temperature, the grains size progressively increases and at the temperature of 900°C a strong sintering effect and coalescence of grains occurs, transforming the original "tree-like" structure into a "knotted mesh" of small crystallites with dimension of 100−200 nm. In Figure 4.1 the progressive increase of the grain size and the transformation of the original structure can be seen for the case of the MnO$_x$ film deposited at 50 Pa of O$_2$. Referring to the Figure 4.1, we can also notice that, related to the increase of grains size, there is also an increase in the film porosity: by increasing the annealing temperature the film becomes less and less compact and many voids arise. Similar trends are also visible in samples deposited at other pressures (i.e., 1 Pa, 10 Pa, and 100 Pa), even though the overall nanoporosity is different.

On the other hand, annealing in vacuum, compared with the thermal treatment conducted in air at the same temperature (i.e., 500°C), leads to the formation of coarse grains and a more disordered overall structure. The cross-sectional SEM images of the films annealed at 500°C in air and in vacuum are shown in Figure 4.2. As we can see, this effect of enlargement of the crystalline grains is more evident in the films deposited at lower pressure (i.e., 1 Pa and 10 Pa).

Table 4.2 shows the SEM images of film's cross-sections for the various oxygen pressures and annealing conditions.
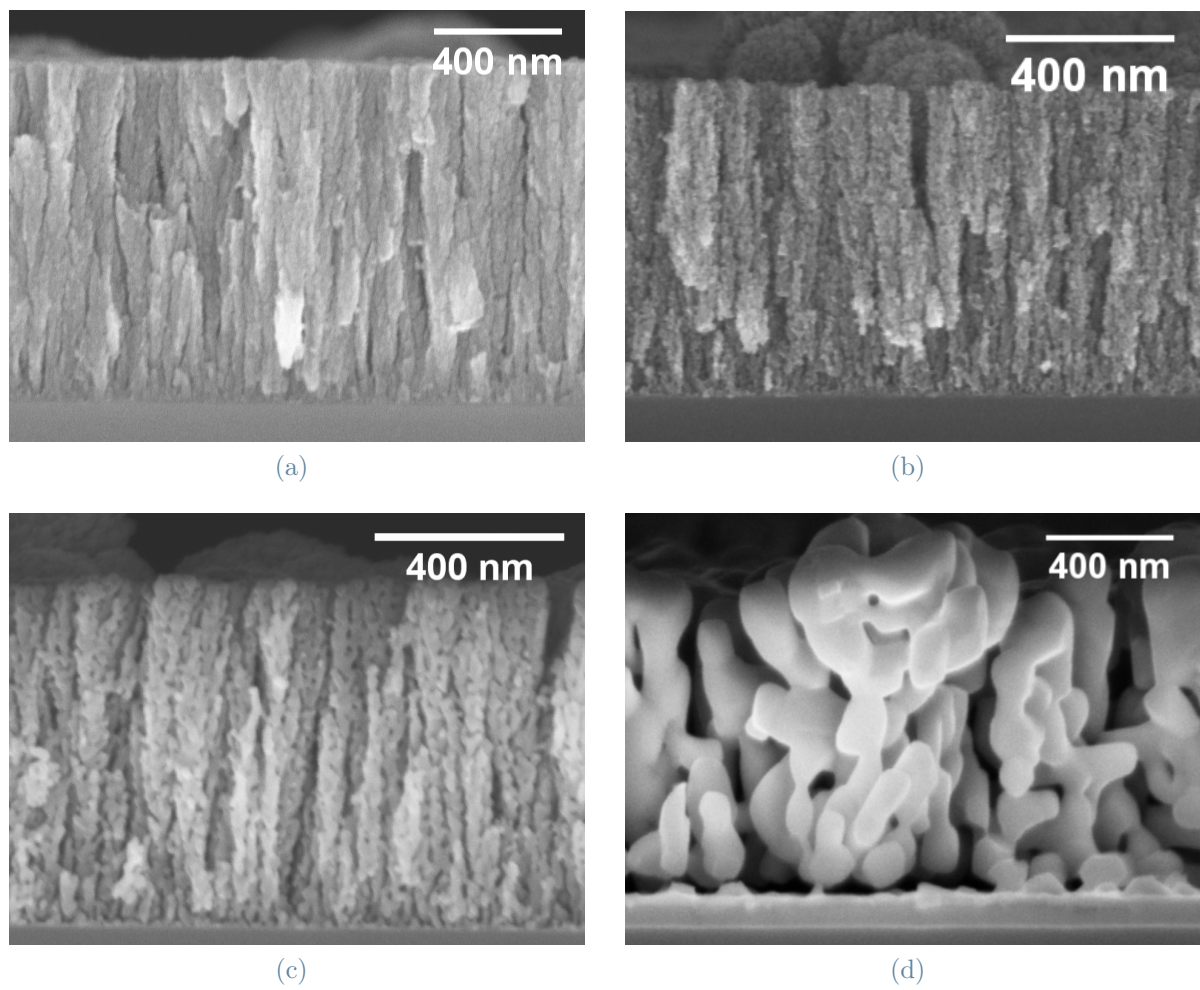
Figure 4.1: Cross-sectional SEM images of the MnO$_x$ film deposited at 50 Pa O$_2$: as deposited (a) and after air-annealing at 300°C (b), 500°C (c), and 900°C (d).

(a)   (b)

(c)   (d)

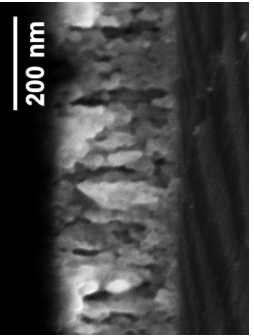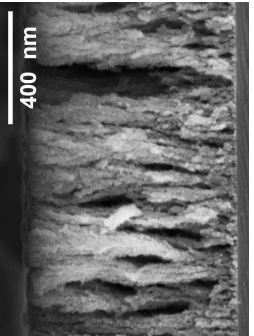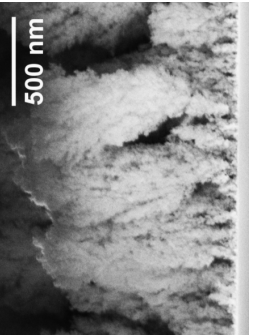(e)   (f)

(g)   (h)
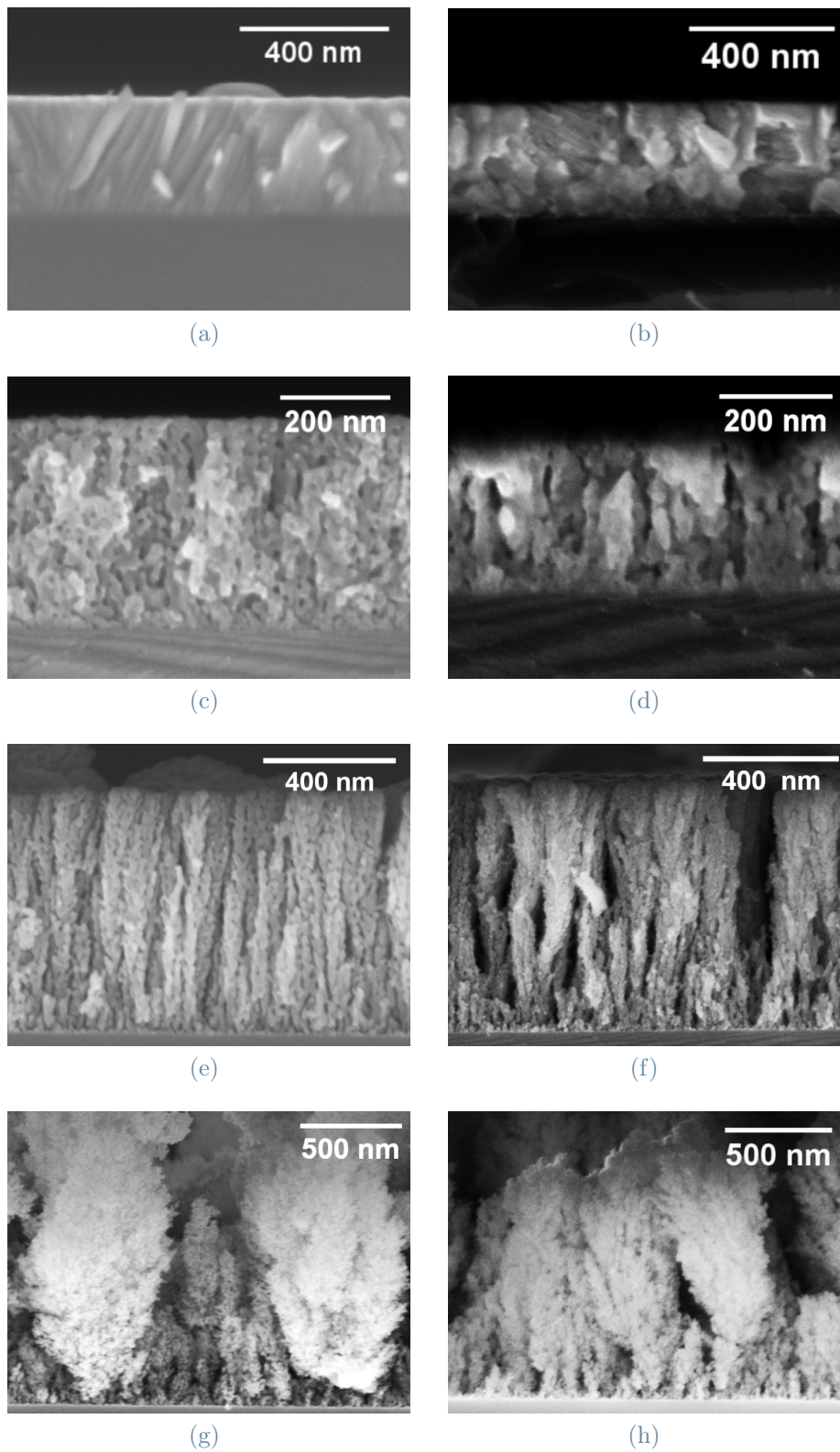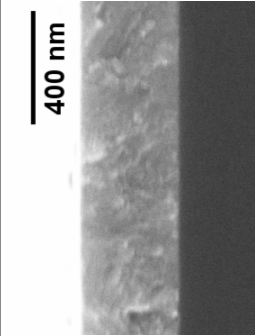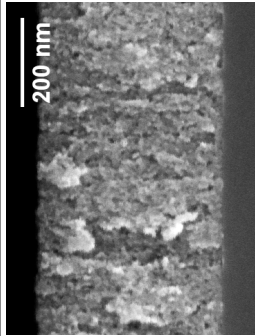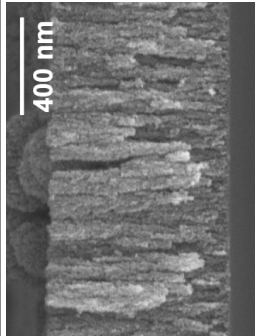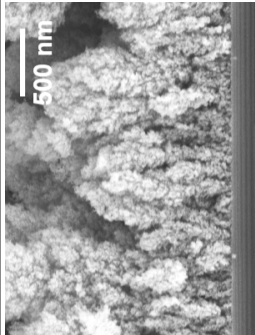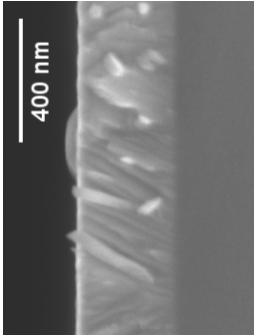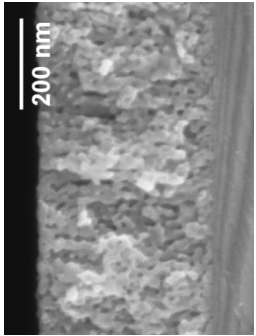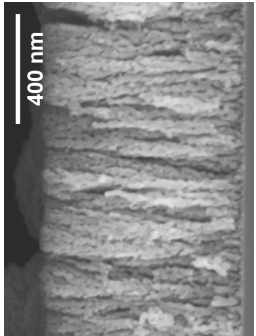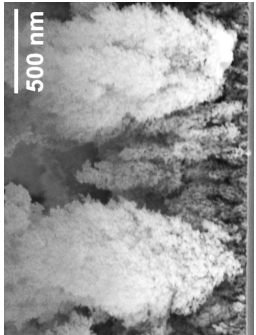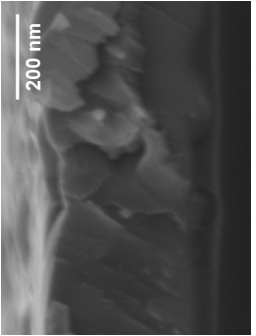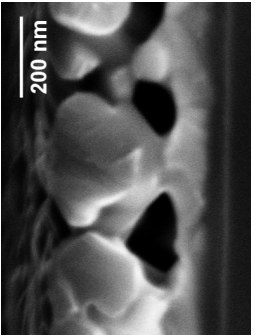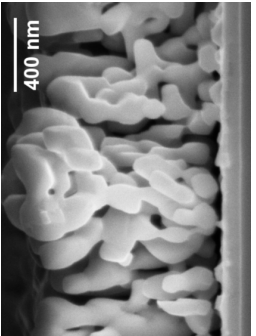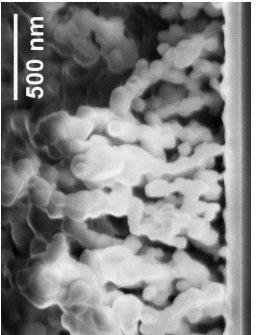
Figure 4.2: Cross-sectional SEM images of the MnO$_x$ film annealed at 500°C in air (on the left) and in vacuum (on the right). Deposited at 1 Pa (a-b), 10 Pa (c-d), 50 Pa (e-f), and 100 Pa (g-h) O$_2$ pressure.

Table 4.2: Cross-sectional SEM images of annealed samples. All investigated conditions are reported.

4.3.   Crystalline structure of annealed films

As for the case of as-deposited films, characterization of MnO$_x$ phases were performed by means of Raman, EDX and XRD analysis. As we will see, the annealing treatments carried out on as-deposited films will expand the range of phases that can be obtained.

4.3.1.   Raman analysis

First of all, Raman analysis shows that no phase change occurs after annealing in air at 300°C; in fact, the films annealed at 300°C and the as-deposited ones, show completely similar Raman spectra. In order to see a phase change, the temperature of the thermal treatment must be raised. This is evidenced by the appearance of new peaks in the Raman spectra of the samples annealed in air at 500°C shown in Figure 4.3a. The new spectra exhibit four main peaks at ~ 200 cm^{-1}, ~ 318 cm^{-1}, ~ 353 cm^{-1}, and ~ 704 cm^{-1} (not affected by pressure), which are a fingerprint of the Mn$_2$O$_3$ phase according to [27]. We note that the signal of the substrate is more evident in samples deposited at higher pressure. This may be due to the fact that films deposited at higher pressure are intrinsically more porous and the annealing treatment further increases the porosity of the film [47, 53, 68–73]. Moreover, no phase change was found to occurs when the temperature is increased from 500 to 900°C. The only difference observed is that the Raman peaks for the sample annealed at 900°C (not shown) are more defined, indicating a better crystalline quality. On the other hand, it has been shown that changing the annealing atmosphere can lead to the formation of a new phase. The Raman spectra of the MnO$_x$ films annealed in vacuum at 500°C are shown in Figure 4.3b. It should be noted that the spectra of the samples deposited at 50 and 100 Pa are not reported as they were highly damaged by the absorption of carbon (detected by Raman spectroscopy) during the annealing treatment due to some technical problems. This turned out to be an issue only for samples deposited at high pressures, as they are more porous and therefore more prone to absorb any impurities present in the atmosphere. In any case, we can state that annealing in vacuum at 500°C leads to the formation of the Mn$_3$O$_4$ phase, whose Raman spectrum is characterized, as previously discussed, by a very intense peak at about 660 cm^{-1} and two less intense peaks at low wavenumbers (i.e., 321 cm^{-1} and 375 cm^{-1}) [27].

Lastly, we observe that the Raman spectrum of Mn$_3$O$_4$ obtained by annealing in vacuum shows better definition of the peaks (reduced FWHM and better signal-to-noise ratio) compared to Mn$_3$O$_4$ as-deposited at 1 Pa O$_2$ (see Figure 4.4). In particular, the main peak at ~ 665 cm^{-1} "loses" its shoulder at ~ 630 cm^{-1}, shifts to ~ 660 cm^{-1}, and becomes narrower (the FWHM reduces from 23.3 cm^{-1} to 14.2 cm^{-1}). This further confirms the
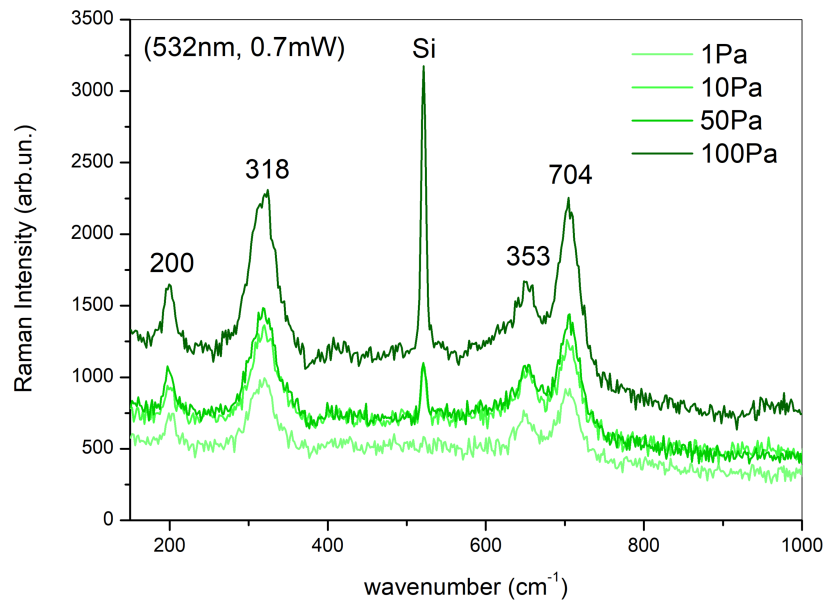
(a)
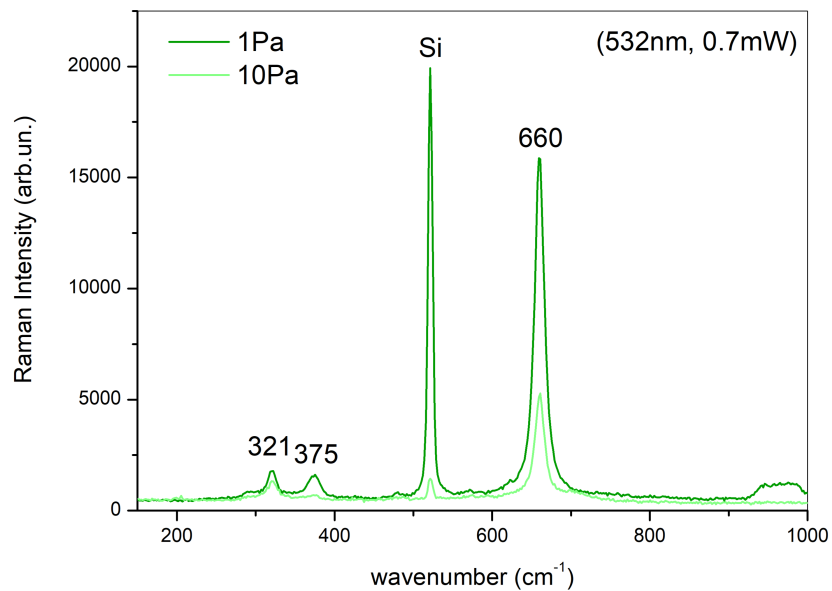
(b)

Figure 4.3: Raman spectra of annealed MnO$_x$ (substrate: Si): annealing at 500°C in air (a) and in vacuum (b).

hypothesis according to which the deposition at an oxygen pressure of 1 Pa results in an amorphous matrix with small dispersed crystals of Mn_3O_4.
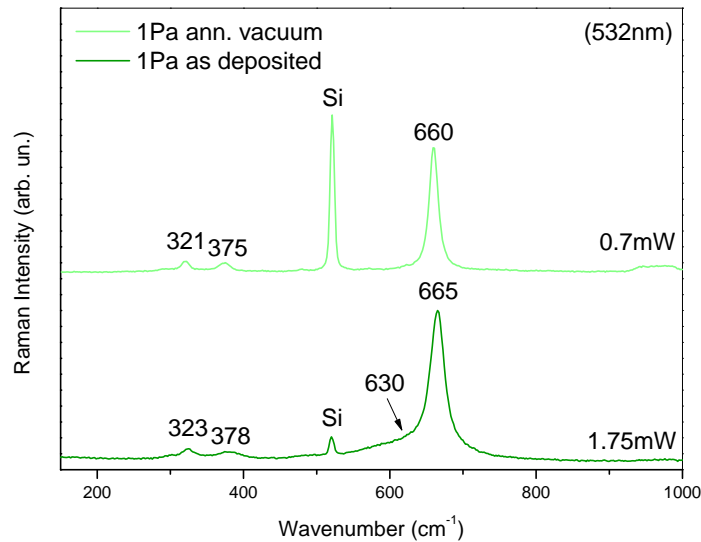

Figure 4.4: Raman spectra of Mn_3O_4 (substrate: Si): as deposited at 1 Pa O_2 pressure and after annealing in vacuum at 500°C.
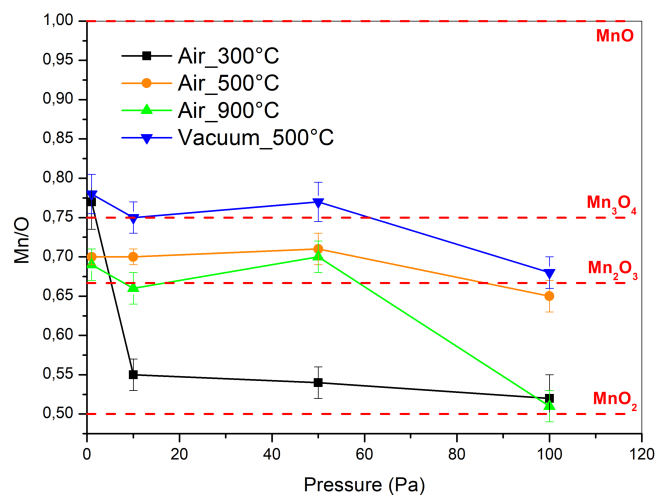
4.3.2. EDX analysis

Figure 4.5: Mn/O ratio of annealed MnO_x films at different O_2 pressures, normalized to the target Mn/O ratio.

As well as the as-deposited films, the annealed samples were also subjected to EDX analysis in the same manner previously discussed (see subsection 3.3.2). The results, normalized to the target Mn/O ratio, are shown in Figure 4.5. Also in the case of annealed

films, EDX data are consistent with the results from Raman analysis: the as-deposited situation remain unchanged until the temperature of 500°C, for which the Mn$_2$O$_3$ phase forms; the same phase is obtained also at 900°C. After vacuum annealing, the Mn$_3$O$_4$ phase results. It must be noted that the values related to the samples deposited at 100 Pa deviate significantly from the expected value probably due to its high porosity. Anyway, please note that these considerations must be interpreted in the context of the limitations of this technique previously discussed (see subsection 3.3.2).

4.3.3. GI-XRD analysis

To complete the characterization of annealed films, some representative samples of all phases were selected for XRD analysis. The diffraction patterns of annealed (in air and vacuum at 500°C) MnO$_x$ films, deposited at 1 Pa, 10 Pa and 50 Pa, compared with the reference patterns of Mn$_3$O$_4$ (card n° 1876, Mincryst database [74]) and Mn$_2$O$_3$ (card n° 5956, Mincryst database [77]) are shown in Figure 4.6.

First, by looking at the diffraction patterns of the samples deposited at 1 Pa O$_2$ pressure before and after the annealing in vacuum at 500°C, we can see that after the thermal treatment the sample exhibits an improved crystalline quality confirmed by the fact that the XRD pattern is characterized by very defined peaks. Moreover, the diffraction pattern is perfectly in agreement with the reference of the Mn$_3$O$_4$ phase. On the other hand, considering the XRD pattern of the sample deposited at 10 Pa of oxygen and annealed in vacuum at 500°C, it partially disagrees with the reference (even if the Raman spectrum is coherent with Mn$_3$O$_4$ phase, see Figure 4.6a) and it is also characterized by a lot of noise. Since, XRD is sensitive to the orientation of crystalline grains and to the long range order, this could be index of a different preferential orientation of the crystalline grains and/or a bad crystalline quality at long range, maybe due to the fact that, in vacuum, the crystallization process is more difficult than in air. Therefore, Raman and XRD analysis are not in accordance due to the fact that they are sensitive to different levels of order: probably what we obtain is a set of tiny crystalline domains of Mn$_3$O$_4$ randomly oriented. Anyway, further investigations are needed in order to validate this hypothesis.

Conversely, there is no doubt that the annealing in air at 500°C leads to the formation of the Mn$_2$O$_3$ phase. In fact, the XRD patterns for the samples deposited at 10 Pa and 50 Pa (the sample at 1 Pa was not tested), annealed in air at 500°C, are perfectly in agreement with the XRD reference (see Figure 4.6b). As highlighted in the figure, almost all the peaks of interest are present, with no shift (or negligible shift) with respect to the reference.
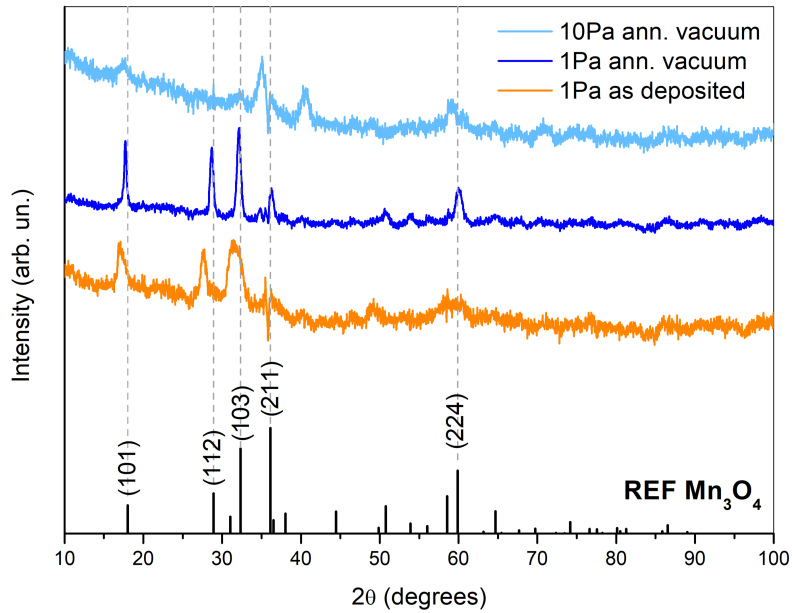
(a) Comparison between XRD patterns of 1 Pa as-deposited sample and vacuum annealed samples deposited at 1 Pa and 10 Pa.
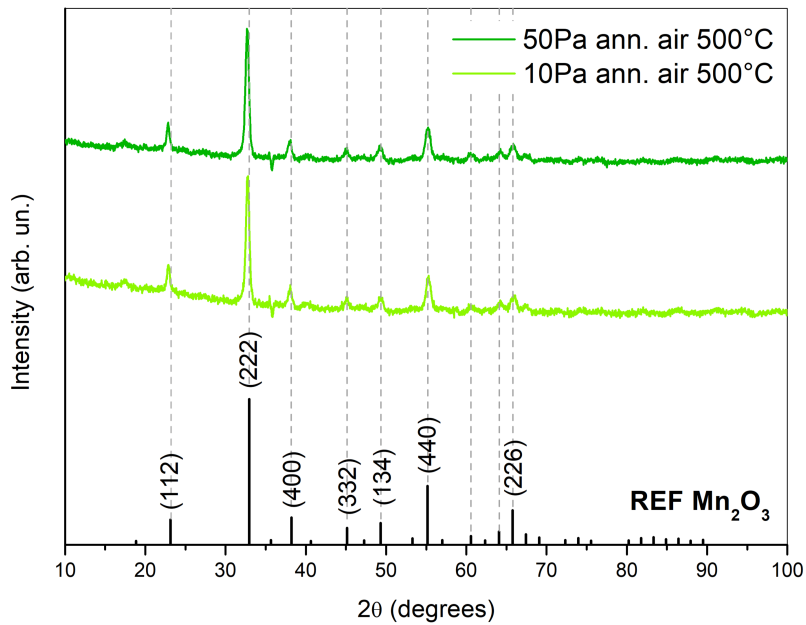
(b) XRD patterns of air annealed samples deposited at 10 Pa and 50 Pa.

Figure 4.6: XRD patterns of annealed MnO$_x$ films compared with the reference.

4.4.   Annealing on glass substrate: a peculiar case

The same analyses that were carried out on films deposited on silicon substrate were also performed on selected films deposited on glass and FTO-coated glass. Although the results obtained for the films deposited on FTO (here not shown) were consistent with what was just described, the same could not be said for the depositions on glass. In fact, Raman analysis conducted after the thermal treatment in air at 500°C on the film deposited on glass at 10 Pa O$_2$ revealed the appearance of a new MnO$_x$ phase. The comparison of Raman spectra of the samples deposited on silicon and glass substrates, at 10 Pa O$_2$ pressure, and annealed in air at 500°C is reported in Figure 4.7.
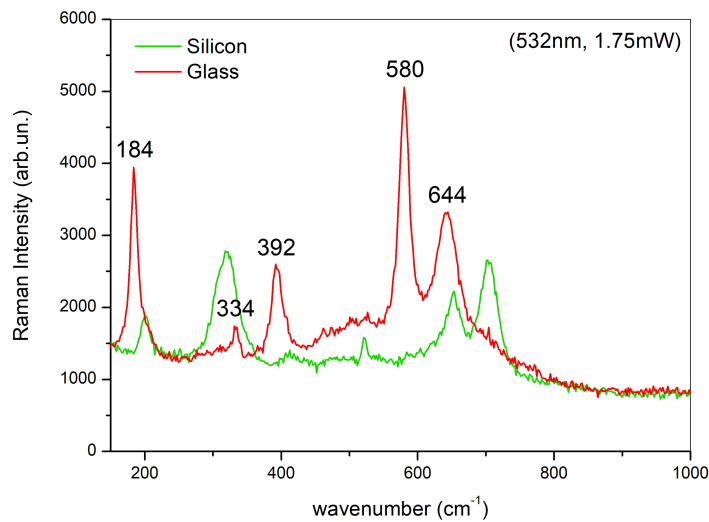
Figure 4.7: Comparison between MnO$_x$ films deposited on silicon (green) and glass (red) substrate at 10 Pa O$_2$ pressure and annealed in air at 500°C.

The Raman spectrum of the sample deposited on glass exhibits five well defined peaks at $\sim$ 184 cm^{-1}, $\sim$ 334 cm^{-1}, $\sim$ 392 cm^{-1}, $\sim$ 580 cm^{-1}, and $\sim$ 644 cm^{-1} which are perfectly in accordance with the ones reported by Xin et al. [27] for the $\alpha-$MnO$_2$ phase. Further proof of the appearance of this new phase comes from XRD measurement. The XRD pattern of the film deposited on glass at 10 Pa oxygen pressure and annealed in air at 500°C, shown in Figure 4.8, was compared with the powder reference pattern of $\alpha-$MnO$_2$ (AMCSD 0016237, American Mineralogist Crystal Structure Database [78]). Indeed, the reference pattern corresponds to cryptomelane-hollandite, i.e., the $\alpha-$MnO$_2$ phase containing K$^+$ cations in the large 2 $\times$ 2 tunnels.
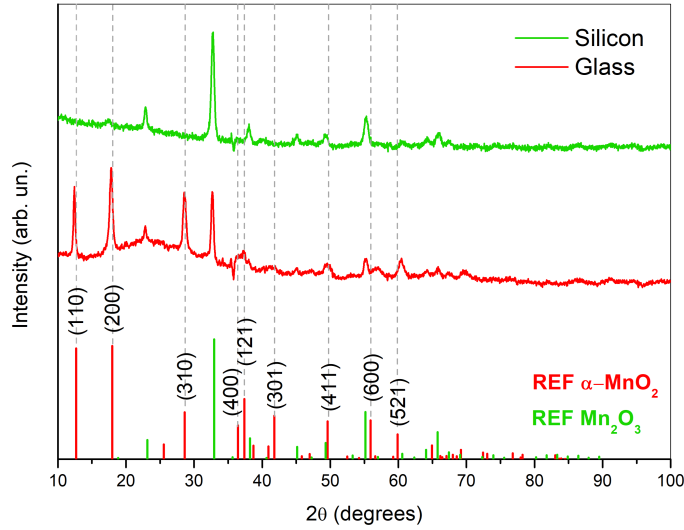
Figure 4.8: XRD patterns of MnO$_x$ films deposited on silicon (green) and on glass (red) at 10 Pa O$_2$ and annealed in air at 500°C, compared with the reference. The most important peaks for the $\alpha-$MnO$_2$ phase are highlighted.

The XRD pattern confirms the hypothesis of formation of $\alpha-$MnO$_2$ but further suggests that the film is actually a mixture of two phases. In fact, the pattern exhibits most of the peaks related to the most important reflections of the $\alpha-$MnO$_2$ phase (i.e., (110), (200), (310), and (411)) but also other peaks that can be assigned to some reflections of the Mn$_2$O$_3$ phase (this latter phase was not detected by Raman probably because of its lower Raman activity compared to $\alpha-$MnO$_2$).

Anyway, it is clear that MnO$_x$ films deposited on silicon and glass, do not exhibits the same phase after annealing in air at 500°C. Since the $\alpha-$MnO$_2$ exists predominantly as an ion-intercalated form, the hypothesis is that, as a result of the annealing temperature, elements such as potassium (K) and/or sodium (Na), present in the glass substrate, act as dopant elements to the film and lead to the formation of the ion-intercalated $\alpha-$MnO$_2$ phase. The hypothesis that the substrate may influence the film phase is also reported in a work done by Nilsen et al. [79] in which MnO$_x$ thin films are obtained by atomic layer deposition on many different substrates, which also provide dopant elements to the growing film. To complete the discussion, we also mention that the co-presence of the Mn$_2$O$_3$ and $\alpha-$MnO$_2$ phases could be due to the fact that this "doping effect" actually occurs only in the region of the film in contact with the substrate and therefore, the further away from it, the more the film becomes independent of the substrate and crystallizes in the usual Mn$_2$O$_3$ phase. However, these hypotheses need further experiments and investigations to be validated. For this reason, optical measurements on annealed films

(that must be conducted on glass substrates) will not be included in this work since the phase cannot be accurately controlled.

4.5. Phase control by PLD and annealing: summary

In this work, we have investigated the influence of oxygen pressure and annealing temperature on the formation of different MnO$_x$ phases obtained by PLD depositions. The result is that these two parameters were discovered to be key parameters for the formation of three different MnO$_x$ phases, that can be obtained with different morphologies at the nanoscale, to some extent. Based on Raman, EDX and XRD analysis, we have found that by room-temperature PLD depositions at different oxygen pressure, ranging from 1 Pa to 100 Pa, we are able to obtain two different phases: nanocrystalline Mn$_3$O$_4$ from deposition at 1 Pa of O$_2$ and amorphous $\delta-$MnO$_2$ from depositions at higher pressures. This condition remains unchanged after thermal treatment at low temperature in air (i.e., 300°C), while a new phase arises after annealing at higher temperatures (i.e., 500°C and 900°C): Mn$_2$O$_3$. By changing the annealing atmosphere, i.e, after annealing in vacuum at 500°C, the Mn$_3$O$_4$ phase is obtained. The following Table 4.3 summarizes the results for each investigated condition.

	Pressure [Pa]			
	1	10	50	100
As-deposited	nanocrystalline Mn$_3$O$_4$	amorphous $\delta-$MnO$_2$	amorphous $\delta-$MnO$_2$	amorphous $\delta-$MnO$_2$
Air ann. 300°C	nanocrystalline Mn$_3$O$_4$	amorphous $\delta-$MnO$_2$	amorphous $\delta-$MnO$_2$	amorphous $\delta-$MnO$_2$
Air ann. 500°C	Mn$_2$O$_3$	Mn$_2$O$_3$	Mn$_2$O$_3$	Mn$_2$O$_3$
Air ann. 900°C	Mn$_2$O$_3$	Mn$_2$O$_3$	Mn$_2$O$_3$	Mn$_2$O$_3$
Vacuum ann. 500°C	Mn$_3$O$_4$	Mn$_3$O$_4$	Mn$_3$O$_4$	Mn$_3$O$_4$

Table 4.3: Overwiev of MnO$_x$ phases we are able to obtain combining PLD and thermal treatments.

These results are valid for depositions on silicon and FTO-coated glass substrate. For depositions on glass the situation is still unclear and further investigations are needed in order to provide a detailed and clear description of the obtainable MnO$_x$ phases.

5 | Electrochemical characterization of MnO$_x$ films

In this chapter, after a brief introduction on the current research situation on manganese oxides electrochemistry, the preliminary electrochemical measurements performed on some selected MnO$_x$ samples will be presented.

5.1. Electrochemistry of MnO$_x$ materials

As already mentioned in the first chapter (see subsection 1.3), manganese oxides have been extensively studied in the last decades, due to their numerous applications. In particular, the electrochemical properties of manganese oxides have been investigated in the last years, due to their potential use in electrical energy storage devices which have become increasingly attractive in recent years. For this reason, having a good knowledge of electrochemical properties of MnO$_x$ materials is extremely important. Among the great variety of MnO$_x$ phases, the most extensively studied is MnO$_2$. In fact, several literature works report the use of MnO$_2$ in many electrochemical devices, such as supercapacitors [2, 3], batteries [6–14] and electrocatalysts [4–6]. Despite the huge number of work devoted to the study of these materials, their general electrochemical behaviour is still not fully clarified. In fact, MnO$_x$ electrochemistry is quite complex and varied, depending on specific crystallographic type, pH, and electrolyte composition. Moreover, as depicted in the following Figure 5.1, it involves multiple oxidation states of Mn as well as formation of intermediate compounds and phase transformations [80].

A detailed investigation on the electrochemistry of MnO$_x$ materials is beyond the scope of this thesis project and it can be found in other literature works [13, 80, 81]. My work, predominantly focused on the synthesis (and characterization) of MnO$_x$ thin films via PLD and subsequent thermal treatments, provides a method to obtain pure MnO$_x$ films with controlled morphology and phase depending on the deposition O$_2$ pressure and annealing temperature. Therefore, the films produced can be used as model systems to study the basic electrochemical behavior of MnO$_x$ materials in simple half-cell configuration.
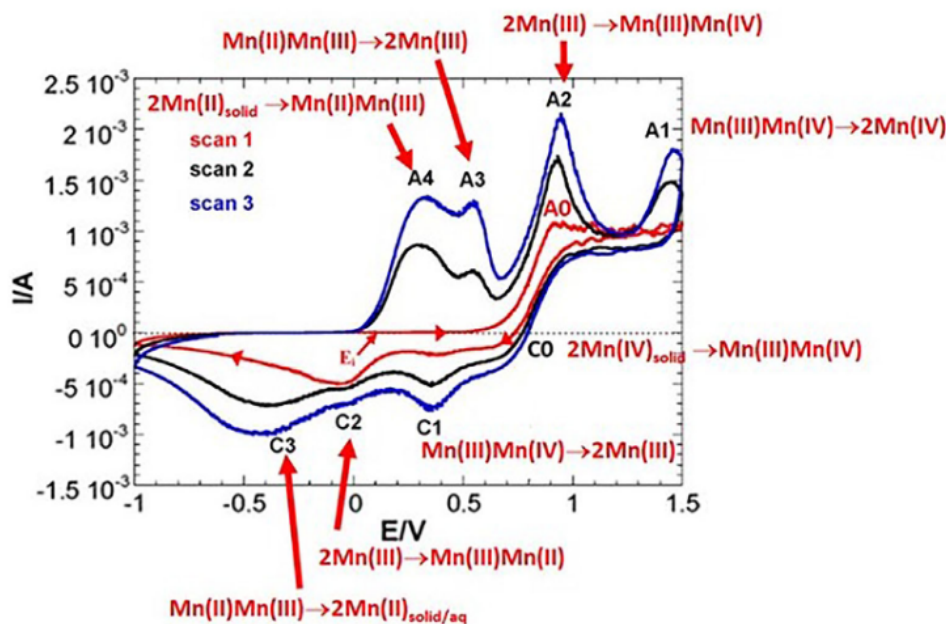
Figure 5.1: Prototypical case of the CV of birnessite electrodeposition onto SnO$_2$ from a neutral, deaerated Na$_2$SO$_4$ 0.4 M, MnSO$_4$ 4 mM solution. Taken from [80].

In the following, the preliminary electrochemical measurements performed on some selected MnO$_x$ samples will be presented.

5.2.   Electrochemistry setup

The setup used in this work for the electrochemical measurements is shown in Figure 5.2. At the base of the cell, the working electrode (the MnO$_x$ film, WE) is pressed by a Teflon cell, made available by SoLINano-Σ lab (Department of Physics of Politecnico di Milano). Between the two, there is an O-ring which, if the setup is properly mounted, will seal the cell and prevent electrolyte leakages. Inside the central well (with a diameter of 5 mm), the liquid electrolyte can be inserted ($\sim$ 1 mL). The cell is equipped with channels, which were used to insert the two platinum wires acting as the counter electrode (CE) and the quasi-reference electrode (Pt-QRef., RE). The potential shift of the Pt-QRef. with respect to the Ag/AgCl reference electrode was previously measured to be + 445 mV in the investigated electrolytes.

The electrolytes used for the measurements are composed of deionized water with zinc, sodium, and manganese sulfates dissolved. The chemical products employed for the electrolytes were: Sodium sulphate anydrous Na$_2$SO$_4$ (Sigma Aldrich, $\geq$ 99.0%), Zinc sulphate heptahydrate ZnSO$_4 \cdot 7$ H$_2$O (Sigma Aldrich, $\geq$ 99.0%), and Manganese(II) sulphate
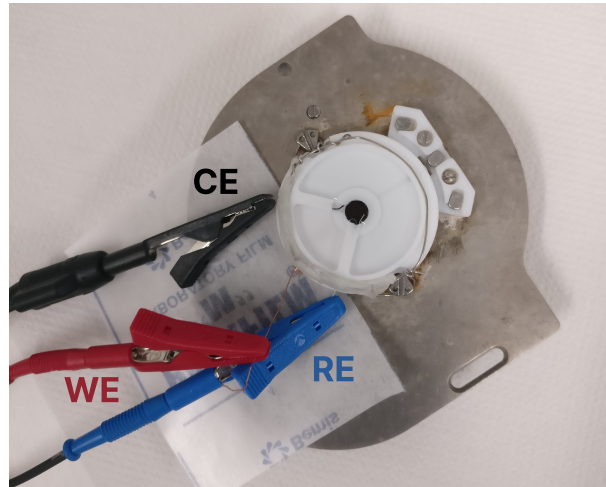
Figure 5.2: Electrochemistry setup used for electrochemical measurements on MnO$_x$ films.

monohydrate MnSO$_4 \cdot$ H$_2$O (Sigma Aldrich, $\geq 98\%$). The electrolytes used were: Na$_2$SO$_4$ 0.2 M (NS electrolyte) and ZnSO$_4$ 2 M + MnSO$_4$ 0.1 M (ZMS electrolyte). Since the electrochemistry behaviour of MnO$_x$ is rather complex and depends on many experimental parameters (MnO$_x$ phase, electrolyte composition and pH), the NS electrolyte was chosen due to its inertness in the investigated potential ranges (see below). In fact, such electrolyte would not interact with the MnO$_x$ film, thus allowing to study the fundamental electrochemical behaviour of the film itself. The only possible interaction may be the intercalation of Na$^+$ ions into the tunnels or interlayer spacings of the different MnO$_x$ phases. Further experiments were then performed with the ZMS electrolyte, which is the common electrolyte used in the ZIBs field, in order to study the effect of the presence of Zn^{2+} ions on the electrochemical behaviour of MnO$_x$ films. In addition to Zn^{2+}, such electrolyte contains Mn^{2+} active species, which can directly participate in the electrochemical reactions (in the real ZIB practice, Mn^{2+} ions are required to compensate for the cathodic dissolution).

The films used for electrochemical tests were produced by PLD at different O$_2$ pressures (i.e., 1 Pa, 10 Pa, and 50 Pa) and then subjected to annealing treatments in air and vacuum atmosphere at 500°C. Both as-deposited and annealed samples were tested. Deposition time at any oxygen pressure was set in order to obtain a film thickness of $\sim$ 500 nm. The films exhibit poor electronic conductivity (i.e., $\sim 10^{-5}-10^{-8}$ S cm^{-1} [13]) and require a conductive substrate to be used in electrochemical tests. Therefore, all the films were deposited on fluorine-doped tin oxide (FTO) coated on soda-lime glass slides produced by Sigma Aldrich (total thickness: 2.2 mm, FTO thickness: 550 nm, sheet resistance: $\sim$ 7 Ω/sq, composition: SnO$_2$: F $\sim$ 1.85). The substrate was properly masked during the deposition in order to make sure that part of FTO remains available for contacts
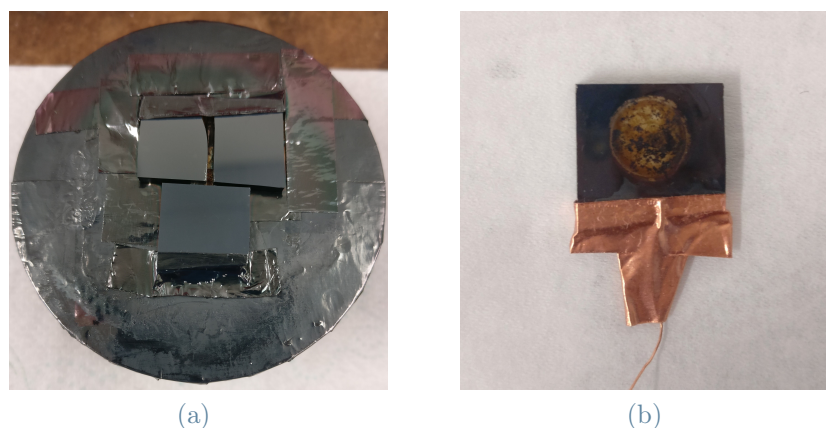
Figure 5.3: Samples for electrochemical tests: MnO$_x$ samples after PLD deposition (a); sample with contacts after electrochemical test (b).

made via copper tape and copper wire (Figure 5.3). Before electrochemical tests, all samples were characterised by Raman and SEM analysis (not shown) which confirm that the FTO substrate, unlike glass, did not affect the phase and morphology of the films. In fact, the MnO$_x$ films deposited on FTO exhibit the same phase and morphology of the films deposited on Si in the same conditions.

5.3. Electrochemical tests in NS electrolyte

The first electrochemical tests were performed with the NS electrolyte on MnO$_x$ films deposited at 1 Pa, 10 Pa, and 50 Pa of oxygen. Both as-deposited, annealed in air (500°C for 2 h) and annealed in vacuum (500°C for 1 h) samples were tested. Cyclic voltammetry (CV) was performed with the potential scanning in a range of -1.45 V to +1.05 V vs. Pt-QRef., starting at 0 V, proceeding in anodic direction, and adopting a scan rate of 10 mV/s for ten cycles. These values were chosen based on previous tests and discussed with Professor B. Bozzini (Battery Materials Engineering Laboratory (BMEL), Energy Department, Politecnico di Milano), who led the work about the electrochemistry part.

The CV curves obtained for the as-deposited and air annealed samples are shown in Figure 5.4. First it can be noticed that by increasing the deposition pressure, i.e., the porosity of the film, the exchanged charge increases. This is evidenced by the progressive increase of the area of the CV curves with the pressure. Reasonably, higher porosity means higher surface area and so, enhanced area available for the electrochemical reactions. However, this effect of porosity is visible only on as-deposited samples. Another visible
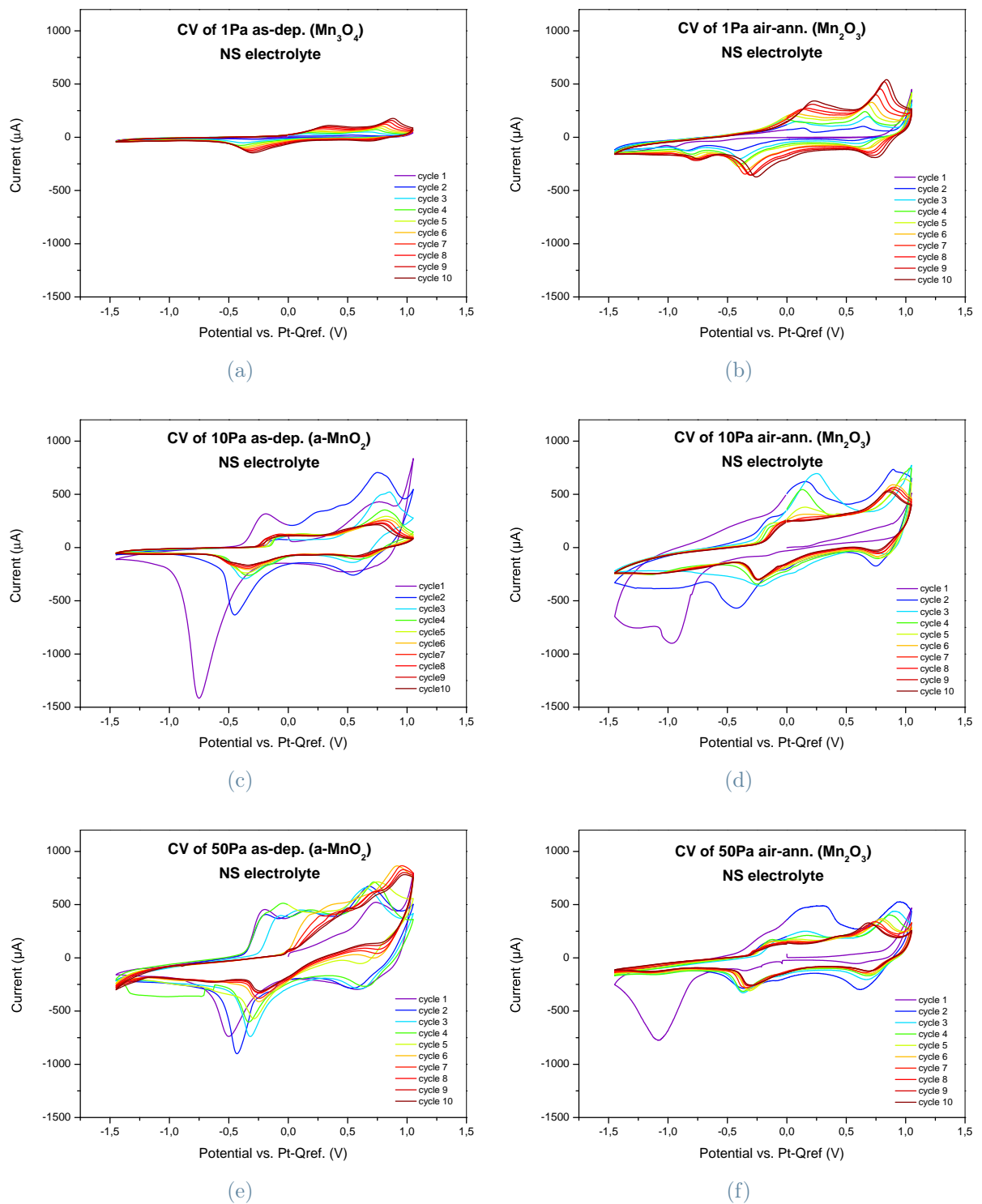
Figure 5.4: CV curves for as-deposited (on the left) and air annealed (500°C for 2 h) samples (on the right) in NS electrolyte: MnO$_x$ films deposited at 1 Pa (a-b), 10 Pa (c-d), and 50 Pa (e-f) of oxygen.

characteristic of these curves is that the shape of the CV curves seems to stabilise after a certain number of cycles (i.e., 5/6 cycles) for all samples. This may mean that the MnO$_x$ films, after some "settling cycles", reach a stable condition. The first cycles may be due to the activation of the starting material which progressively transforms in a new phase, whose electrochemical behaviour is the one observed in the following cycles. The SEM images of the samples post-electrochemistry reveal the formation of *electrodeposited manganese oxide* (EDM), which is a mix of MnO$_x$ in which some forms of MnO$_2$ (e.g., $\delta-$, $\gamma-$ and $\epsilon-$ MnO$_2$ [13, 80, 82]) are mainly present. It must be emphasized that the NS electrolyte does not contain manganese, therefore, what is electrodeposited necessarily comes from the film which is modified. As an example of the typical fibrous morphology of EDM [83], the SEM image of the as-deposited MnO$_x$ film at 50 Pa of oxigen after the electrochemical test is shown in Figure 5.5b. The morphology of the sample before the electrochemical test is reported in Figure 5.5a. It must be emphazised that independently on the starting phase (Mn$_3$O$_4$, MnO$_2$, or Mn$_2$O$_3$) and morphology, the final phase is always EDM. In fact, all samples show similar morphology and Raman spectra after the electrochemical tests. As representative case, the Raman spectra of the pristine and aged sample deposited at 50 Pa of O$_2$ and annealed in air at 500°C, are reported in Figure 5.6. As we can see, the spectrum of EDM displays some peaks at $\sim$ 278 cm^{-1}, $\sim$ 407 cm^{-1}, $\sim$ 478 cm^{-1}, $\sim$ 513 cm^{-1}, and $\sim$ 584 cm^{-1}, compatible with several forms of Mn dioxides and hydroxides according to [28]. However, in some cases (not shown), peaks related to the starting material are present in the post-electrochemistry Raman spectrum as indicating that the MnO$_x$ film only partially reacted.

(a)   (b)
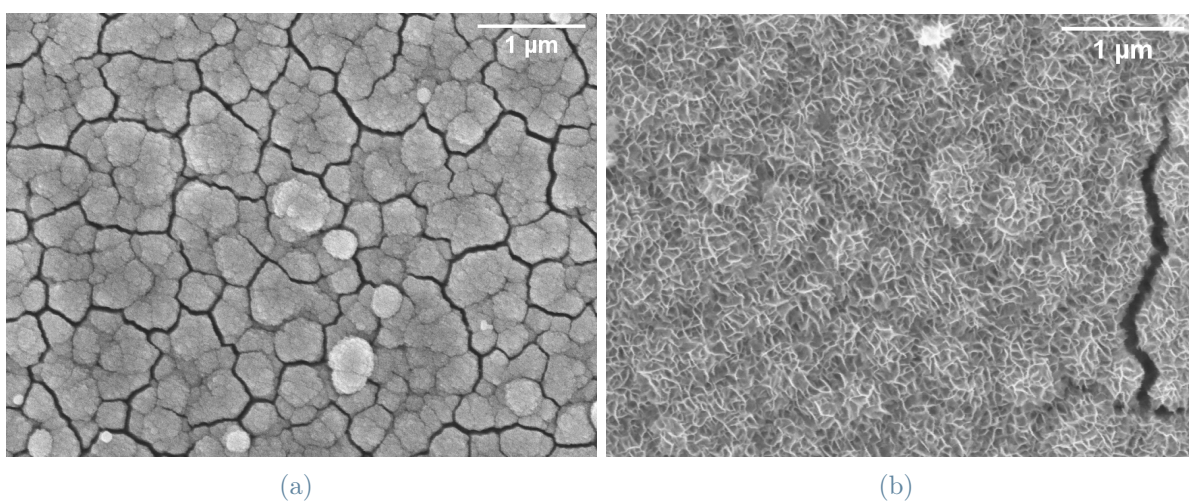
Figure 5.5: Top view SEM images of as-deposited MnO$_x$ film at 50 Pa (MnO$_2$) pre- (a) and post- (b) electrochemistry (EDM).
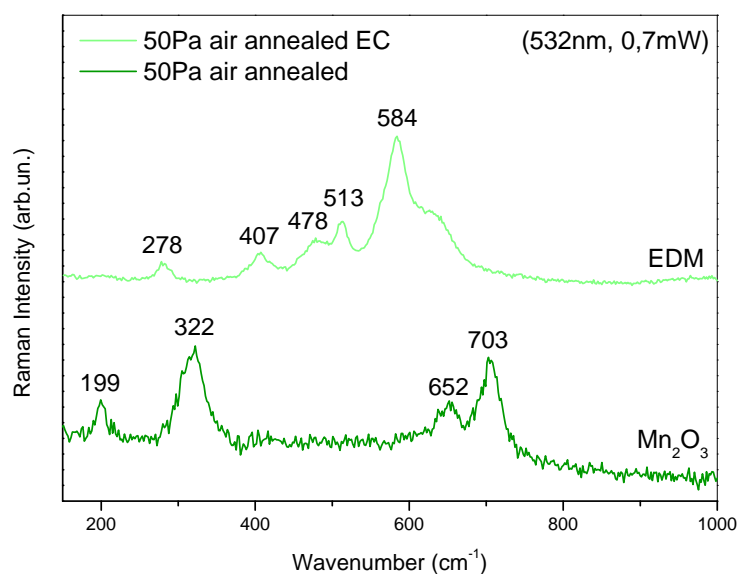
Figure 5.6: Raman spectra of the pristine and aged sample deposited at 50 Pa of O$_2$ and annealed in air at 500°C.

Further considerations can be done by normalizing the CVs. In Figure 5.7 the final cycles (10th cycle) of the samples are reported, both as-deposited and annealed in air (500°C, 2 h), normalized to the cathodic (negative current) minimum. As we can see, all the curves exhibit a sequence of anodic peaks (upper part of the graph), related to the progressive oxidation of Mn^{2+} to Mn^{3+} and Mn^{4+}, and at least two cathodic peaks (lower part of the graph) related to reduction of Mn^{3+} to Mn^{4+} and to Mn^{2+} dissolution.
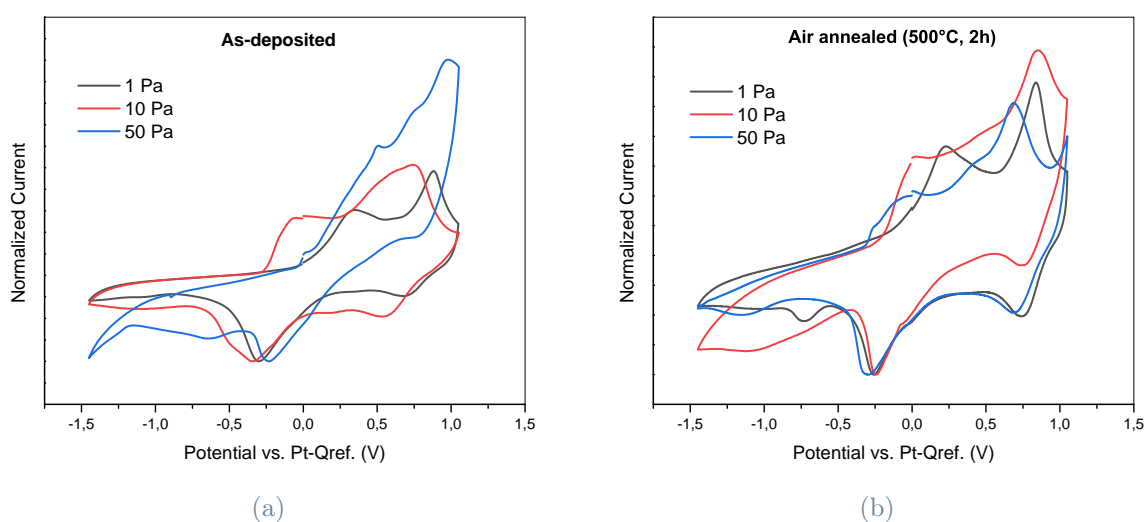
Figure 5.7: Normalized CVs (10th cycle) for as-deposited (a) and air annealed (500°C for 2 h) samples (b) in NS electrolyte.

Moreover, the as-deposited samples exhibit CV curves very different from each others and the effect of porosity is mainly visible in the anodic part of the curves. Interestingly, not only the area but also the position of the peaks varies with pressure (and therefore porosity). On the other hand, annealed samples show much more similar CV curves, even if not identical, but the effect of porosity is lower. This similarity may be due to the same starting Mn$_2$O$_3$ phase, and to the sintering effect coming from the annealing treatment which contributes to homogenize the porosity differencies.

Lastly, any hypothesis of Na$^+$ ions intercalation was excluded since no related characteristics was observed in the CV curves [80]. Intercalation is a cathodic process and so, if occuring, a cathodic "tail" around 0 V (vs. Pt-QRef.) should be present when starting the CV test. However, no sample shows such a feature in its CV curves.

Results regarding the samples annealed in vacuum are not reported since it was not possible to perform CV measurements due to their extremely low electronic conductivity. In fact, the only sample which was tested (MnO$_x$ deposited at 1 Pa and annealed in vacuum at 500°C for 1 h) did not show any electrochemical activity and the CV curves (not shown) were flat. This is due to the fact that the film was not conductive enough to allow the current to flow. This issue further indicate that the as-deposited sample grown at 1 Pa of oxygen (whose electrochemical activity was previously reported) is actually different from the vacuum-annealed samples. On FTO-coated glass, also the colour is a clear indication: the as-deposited sample is dark brown, while the vacuum-annealed one has a more amber and transparent color. The two samples are shown in Figure 5.8.

(a)   (b)
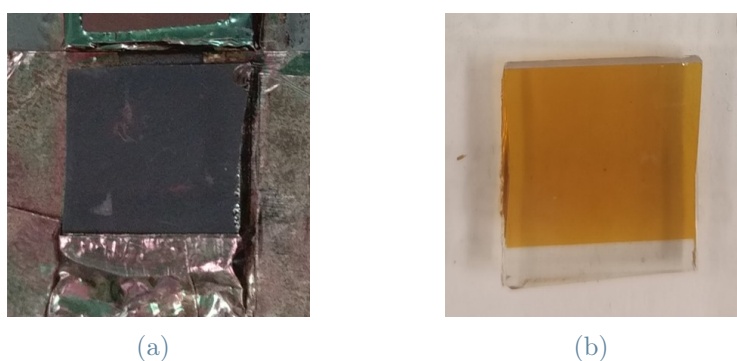
Figure 5.8: Comparison between the as-deposited sample (a) and the vacuum-annealed sample (b) both deposited at 1 Pa oxygen pressure.
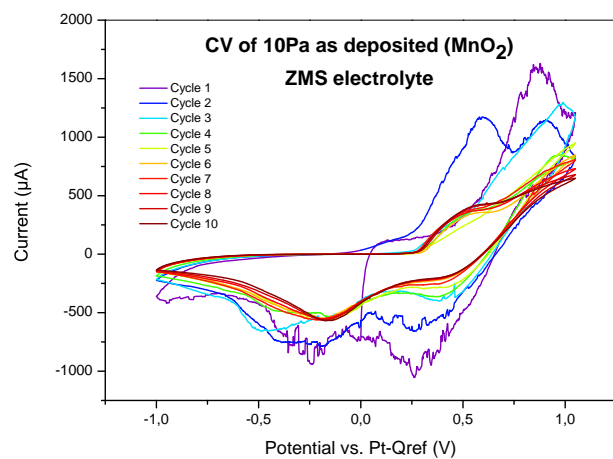
5.4.   Electrochemical tests in ZMS electrolyte

In order to investigate the effect of Zn^{2+} ions on the electrochemical behaviour of MnO$_x$ films, CV measurements were also performed in the ZMS electrolyte. The CV parameters are the same as for the case of NS electrolyte (scan rate of 10 mV/s, 10 cycles) except for the potential range which was reduced between -1 and 1.05 V in order to avoid the plating/stripping of Zn at very low cathodic potentials. CV tests were performed only on three selected samples representative of all the phases: as-deposited MnO$_x$ at 1 Pa for the Mn$_3$O$_4$ phase, as deposited MnO$_x$ at 10 Pa for the MnO$_2$ phase and the sample deposited at 10 Pa and annealed in air at 500°C for 2 h for the Mn$_2$O$_3$ phase.

The resulting CV curves are reported in Figure 5.9. In general, the presence of Zn^{2+} and Mn^{2+} ions in the electrolyte leads to a qualitative change of the shape of the curves both in the general behaviour and on the final result. This is also confirmed by SEM and Raman analysis. In particular, the SEM images (shown in Figure 5.10) of the aged samples, reveal the formation of zinc hydroxide sulfate (ZHS) on the surface of the films, easily recognisable by its characteristic and well-known flake-like structure [10, 43, 81] (see Figure 5.10c and 5.10d). The ZHS formation is also confirmed by the Raman analysis (see Figure 5.11). In particular, in the Raman spectrum of the as-deposited sample at 1 Pa, whose Raman peaks are highlighted in Figure 5.11, two small peaks are visible at ~ 967 cm^{-1} and ~ 1007 cm^{-1} which are commonly attributed to the vibrations of sulphate groups in the ZHS phase [81]. On the other hand, in the left part of the spectrum we found a strutctured band, with peaks at ~ 392 cm^{-1}, ~ 488 cm^{-1} and ~ 639 cm^{-1}, which are difficult to be assigned to a specific phase and can be related to a mix of manganese oxides and hydroxides maybe containing also zn^{2+} ions and/or water molecules [1, 28, 80, 84]. It is important to stress that both in the case of NS and ZMS electrolyte, the final product is a mixture of MnO$_x$ probabily corresponding to some form of birnessite (Figures 5.10e and 5.10f), but the two forms are different (even though the expected electrochemical reactions involve the same transitions between multiple oxidation states of manganese) as confirmed by the two different Raman spectra (see Figure 5.6 for the NS case and Figure 5.11 for ZMS). Anyway, Raman and SEM analysis reveal that independently of the starting MnO$_x$ phase, the electrochemistry of any MnO$_x$ film in the ZMS electrolyte leads to the same final morphology and compound.
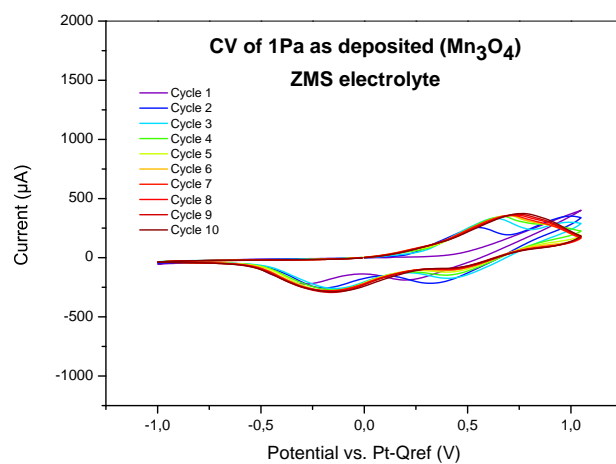
(a)

(b)
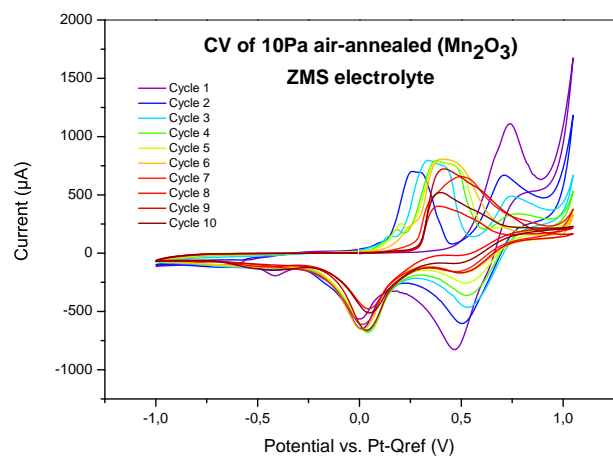
(c)

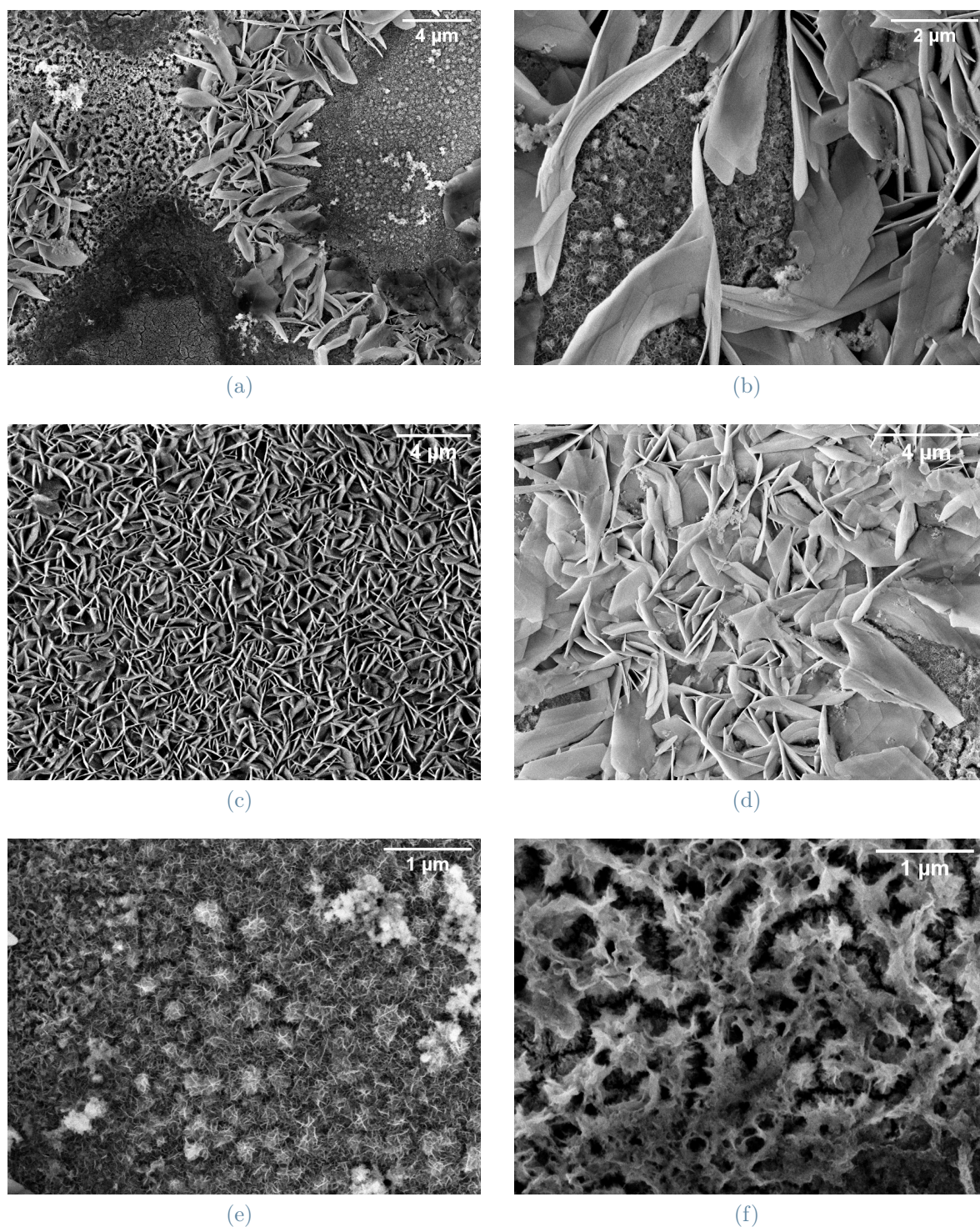Figure 5.9: CV curves for Mn$_3$O$_4$ (a), MnO$_2$ (b) and Mn$_2$O$_3$ (c) in ZMS electrolyte.

Figure 5.10: Top view SEM images of the samples post-electrochemistry in ZMS electrolyte: different morphologies coexists on the as-deposited MnO$_x$ film at 10 Pa after electrochemistry (a); co-presence of EDM and ZHS in the same region (b); comparison between ZHS flakes formed on the as-deposited film at 1 Pa (c) and 10 Pa (d); magnification of different EDM morphologies present on the as-deposited film at 10 Pa (e-f).
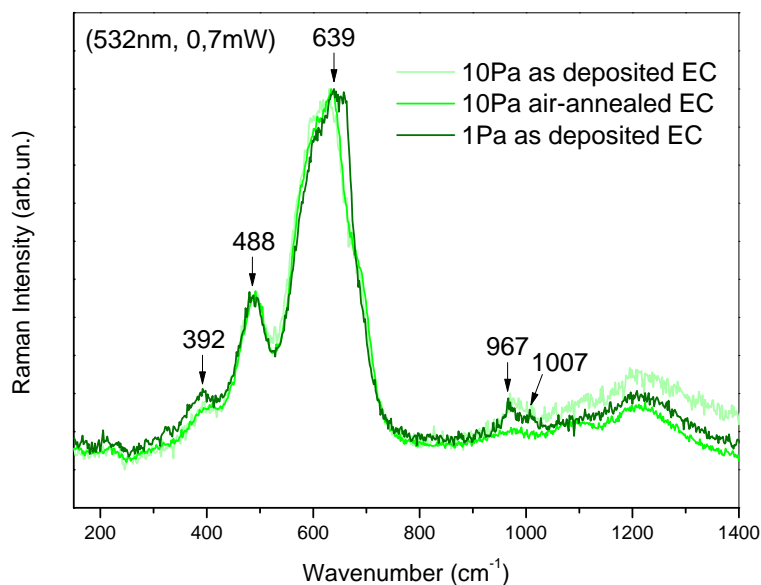
Figure 5.11: Raman spectra (normalised to the tallest peak) of electrochemically aged samples in ZMS electrolyte.

Comparing the CV curves obtained from electrochemical tests in the NS electrolyte and the ones obtained from tests in the ZMS electrolyte, it can be noticed that when the ZMS eletrolyte is used, in the CV of the sample deposited at 10 Pa, a strong "tail" at negative currents appears when starting the CV measurement (around 0 V vs. Pt-QRef.). This may be index of a possible intercalation of Zn^{2+} ions [80]. The same feature is not present in the CVs of the other two samples (Mn$_3$O$_4$ and Mn$_2$O$_3$). This may be due to the fact that the structure of Mn$_3$O$_4$ and Mn$_2$O$_3$ is less favorable to the intercalation of Zn^{2+} ions compared to the tunnel/layer structure of MnO$_2$.

To conclude, also in this case the last cycles of the CV curves were normalised to the cathodic minimum in order to compare the behaviour of the different samples. The results are reported in Figure 5.12. In this case, no particular similarities can be observed except for a rapid rise at the beginning of the anodic part of the CVs ($\approx$ 0.2 V vs. Pt-QRef.) highlighted also by Rossi et al. [80] when Zn^{2+} ions are present in the electrolyte. This can be considered as a further evidence that the electrochemical behaviour of MnO$_x$ materials in presence of Zn^{2+} ions is rather complex and further experiments are needed to completely understand the specific electrochemical process of each MnO$_x$ phase. In particular, the contributions of morphology, phase, and electrolyte should be decoupled to have a detailed picture.
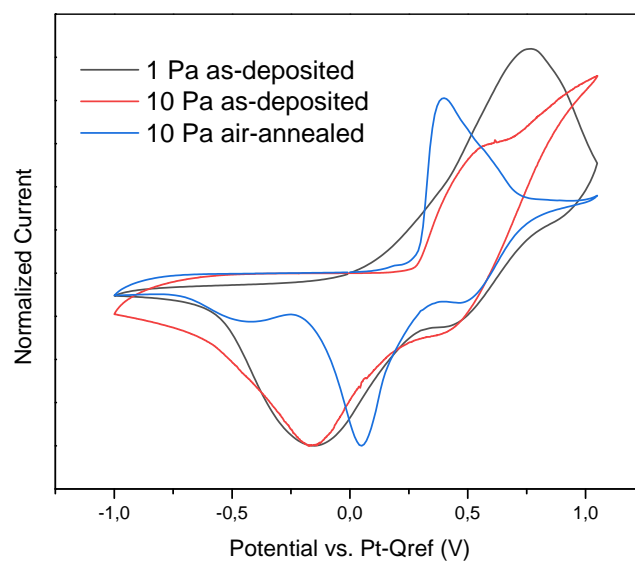
Figure 5.12: Normalised CVs (10th cycle) of electrochemically aged samples in ZMS electrolyte.

6 | Conclusions and future developments

This thesis has focused on the synthesis and characterization of MnO_x thin films. In the following, the main results obtained and future developments will be presented.

The first part of this study was focused on the optimization of the PLD parameters for the synthesis of films with targeted characteristics. MnO_x films with desired thickness and uniformity were obtained, at room temperature, by varying the background O_2 pressure and the target-substrate misalignment. The effect of the O_2 pressure on the films morphology was investigated by SEM analysis and phase characterization was performed by means of Raman, EDX and XRD measurements. It was shown that by increasing the O_2 pressure the deposited MnO_x films exhibit a porous nanostructure more and more similar to a forest of trees, which is usually referred to as a "nano-forest". Given the well-known problems related to the stability of MnO_x materials under the laser beam, a detailed investigation of the effect of laser power and wavelength on the MnO_x films was conducted and the green laser 532 nm resulted to be the correct choice for the Raman characterization of the films. The agreement between Raman, EDX and XRD analysis suggests that two different MnO_x phases can be obtained by PLD depositions: amorphous MnO_2 and nanocrystalline Mn_3O_4. The characterization was conducted on films deposited on a Silicon substrate but depositions on glass were also performed with the aim to studying the optical properties of the MnO_x films obtained. The optical transmittance, reflectance and absorbance of as-deposited MnO_x films were measured, and a basic optical characterization was accomplished.

In the next part, different thermal treatments were performed in order to investigate the effect of the annealing temperature and atmosphere on the films morphology and phase. The MnO_x films were annealed in air at temperatures ranging from 300 to 900°C for different time durations (4 or 2 hours) and in vacuum at 500°C for 1 hour. SEM analysis revealed how the annealing temperature and atmosphere affect the morphology of the films. In particular, regarding the annealing in air, higher temperatures lead to coarse

grains and better crystalline quality. On the other hand, the annealing atmosphere was discovered to have a stronger influence on the MnO_x phase of the films. In fact, Raman analysis on annealed films showed that from different annealing atmospheres two MnO_x phases can be obtained: Mn_2O_3 from the annealing in air and Mn_3O_4 from the annealing in vacuum. However, the Mn_2O_3 phase, was found to appear only for temperatures $\geq 500°C$. For lower temperatures, the MnO_x phase coming from the PLD deposition is preserved. These results are also confirmed by EDX and XRD analysis. Moreover, from Raman and XRD analysis, I was able to notice that the Mn_3O_4 phase obtained directly from PLD and the Mn_3O_4 phase obtained from the annealing in vacuum were different. In particular, the PLD may produce a dispersion of nanocrystals of Mn_3O_4 in an amorphous matrix while after the thermal treatment in vacuum a single Mn_3O_4 phase is obtained.

During my project, I also discovered that the substrate can have an influence on the MnO_x phase obtained and such effect is somehow activated by temperature. Raman analysis on the film deposited on glass at 10 Pa of O_2 and annealed in air at $500°C$ revealed the appearance of a new MnO_2 phase different from the one directly obtained by PLD and from the Mn_2O_3 phase resulting from air-annealing on silicon: the $\alpha-MnO_2$ phase. Since more extensive experiments are needed to completely understand the effect of the glass substrate on the resulting MnO_x phase, optical properties on annealed films are not reported in this study.

In the last part of this work, the electrochemical behaviour of MnO_x films was investigated by means of Cyclic Voltammetry conducted on selected MnO_x samples deposited on FTO-coated glass. The electrochemical tests were performed in two different electrolytes: the NS electrolyte, chosen for a basic characterization of the electrochemical behavior of the films, and the ZMS electrolyte to simulate a more realistic situation of a ZIB. Both as-deposited and air-annealed ($500°C$ for 2 h) films obtained at different O_2 pressures (1 Pa, 10 Pa, and 50 Pa) were tested in the NS electrolyte, while only one sample representative of each MnO_x phase was selected for electrochemical tests in the ZMS electrolyte. The electrochemical investigation conducted in this thesis involves only preliminary experiments and a more detailed analysis should be carried out in order to draw comprehensive conclusions on the electrochemical behaviour of MnO_x materials. However, some interesting points are highlighted in the following:

- a correlation between the O_2 deposition pressure and the amount of charge exchanged during the electrochemical process can be observed in as-deposited samples tested in the NS electrolyte. This is reasonable in view of the fact that films deposited at higher O_2 pressures are more porous and therefore exhibit a greater surface area for electrochemical reactions;

- independently of the starting phase and morphology the electrochemical process leads to the formation of electrodeposited manganese oxide (EDM), consisting in a mix of manganese oxides and hydroxides, characterized by a fibrous morphology. However, Raman and SEM analysis conducted on the aged samples suggest the possibility that two different forms of EDM are obtained in the two electrolytes. In particular, in the case of ZMS electrolyte we have also formation of "flake-like" ZHS precipitates;

- no Na^+ ions intercalation was observed when testing the films in the NS electrolyte, while possible Zn^{2+} ions intercalation was hypothized for the amorphous MnO_2 phase tested in the ZMS electrolyte;

- lastly, no electrochemical activity was observed for the Mn_3O_4 phase obtained from the annealing in vacuum due to its too low electronic conductivity.

This thesis work can be taken as a starting point for future developments in two different directions:

1. the further production and characterization of other MnO_x phases by combining different deposition parameters and thermal treatments;

2. the study of the electrochemical behaviour of MnO_x materials through extensive electrochemical measurements.

In particular, these two paths can include:

- a complete XRD characterization on all the samples produced in this work;

- a more comprehensive study of the combined effect of the glass substrate and the annealing temperature on the resulting MnO_x phase;

- a more in-depth study of the optical properties of the MnO_x films;

- the exploration of new PLD conditions including the gas atmosphere, the background gas pressure, the fluence, the substrate temperature, etc.;

- a more systematic electrochemical investigation on samples deposited at different pressures, annealing temperatures and atmospheres;

- the study of the electrochemical behaviour of MnO_x films in additional electrolytes;

- in-situ measurements combining Raman spectroscopy with CV measurements, thus monitoring in real time the material evolution during electrochemical polarization;

- complementary techniques, such as X-ray photoelectron spectroscopy (XPS), and

Fourier-transform infrared spectroscopy (FTIR), can be employed before and after electrochemical measurements;

To conclude, even though a complete understanding of the subject has not been achieved, some important results have been accomplished and this work can be considered as a starting point for further research on the synthesis and characterization of MnO_x films by PLD and on the electrochemistry of MnO_x materials.

Bibliography

[1] Jeffrey E. Post. Manganese oxide minerals: Crystal structures and economic and environmental significance. *Proc. Natl. Acad. Sci. U.S.A.*, 96(7):3447–3454, March 1999. ISSN 0027-8424, 1091-6490. doi: 10.1073/pnas.96.7.3447.

[2] Daniel Bélanger, Thierry Brousse, and Jeffrey Long. Manganese Oxides: Battery Materials Make the Leap to Electrochemical Capacitors. *Electrochem. Soc. Interface*, 17(1):49–52, March 2008. ISSN 1064-8208, 1944-8783. doi: 10.1149/2.F07081IF.

[3] Dan Wu, Xiubo Xie, Yuping Zhang, Dongmei Zhang, Wei Du, Xiaoyu Zhang, and Bing Wang. MnO2/Carbon Composites for Supercapacitor: Synthesis and Electrochemical Performance. *Frontiers in Materials*, 7, 2020. ISSN 2296-8016.

[4] Yaoqin Zhu, Mengnan Shen, Yonggen Xia, and Ming Lu. Au/MnO2 nanostructured catalysts and their catalytic performance for the oxidation of 5-(hydroxymethyl)furfural. *Catalysis Communications*, 64, April 2015. doi: 10.1016/j.catcom.2015.01.031.

[5] Edy Saputra, Syaifullah Muhammad, Hongqi Sun, H. M. Ang, M. O. Tadé, and Shaobin Wang. Different crystallographic one-dimensional MnO2 nanomaterials and their superior performance in catalytic phenol degradation. *Environ Sci Technol*, 47 (11):5882–5887, June 2013. ISSN 1520-5851. doi: 10.1021/es400878c.

[6] Niklas Borchers, Simon Clark, Birger Horstmann, Kaushik Jayasayee, Mari Juel, and Philippe Stevens. Innovative zinc-based batteries. *Journal of Power Sources*, 484: 229309, February 2021. ISSN 03787753. doi: 10.1016/j.jpowsour.2020.229309.

[7] Wei Sun, Fei Wang, Singyuk Hou, Chongyin Yang, Xiulin Fan, Zhaohui Ma, Tao Gao, Fudong Han, Renzong Hu, Min Zhu, and Chunsheng Wang. Zn/MnO$_2$ Battery Chemistry With H$^+$ and Zn^{2+} Coinsertion. *J. Am. Chem. Soc.*, 139(29):9775–9778, July 2017. ISSN 0002-7863, 1520-5126. doi: 10.1021/jacs.7b04471.

[8] Xiaoxiao Jia, Chaofeng Liu, Zachary G. Neale, Jihui Yang, and Guozhong Cao. Active Materials for Aqueous Zinc Ion Batteries: Synthesis, Crystal Structure, Morphology,

and Electrochemistry. *Chem. Rev.*, 120(15):7795–7866, August 2020. ISSN 0009-2665, 1520-6890. doi: 10.1021/acs.chemrev.9b00628.

[9] Guozhao Fang, Jiang Zhou, Anqiang Pan, and Shuquan Liang. Recent Advances in Aqueous Zinc-Ion Batteries. *ACS Energy Lett.*, 3(10):2480–2501, October 2018. ISSN 2380-8195, 2380-8195. doi: 10.1021/acsenergylett.8b01426.

[10] Jun Ming, Jing Guo, Chuan Xia, Wenxi Wang, and Husam N. Alshareef. Zinc-ion batteries: Materials, mechanisms, and applications. *Materials Science and Engineering: R: Reports*, 135:58–84, January 2019. ISSN 0927796X. doi: 10.1016/j.mser.2018.10.002.

[11] Baozheng Jiang, Chengjun Xu, Changle Wu, Liubing Dong, Jia Li, and Feiyu Kang. Manganese Sesquioxide as Cathode Material for Multivalent Zinc Ion Battery with High Capacity and Long Cycle Life. *Electrochimica Acta*, 229:422–428, March 2017. ISSN 00134686. doi: 10.1016/j.electacta.2017.01.163.

[12] Jianwu Hao, Jian Mou, Jingwen Zhang, Liubing Dong, Wenbao Liu, Chengjun Xu, and Feiyu Kang. Electrochemically induced spinel-layered phase transition of Mn3O4 in high performance neutral aqueous rechargeable zinc battery. *Electrochimica Acta*, 259:170–178, January 2018. ISSN 00134686. doi: 10.1016/j.electacta.2017.10.166.

[13] Christian M. Julien and Alain Mauger. Nanostructured MnO2 as Electrode Materials for Energy Storage. *Nanomaterials*, 7(11):396, November 2017. ISSN 2079-4991. doi: 10.3390/nano7110396.

[14] Muhammad H. Alfaruqi, Vinod Mathew, Jihyeon Gim, Sungjin Kim, Jinju Song, Joseph P. Baboo, Sun H. Choi, and Jaekook Kim. Electrochemically Induced Structural Transformation in a γ-MnO2 Cathode of a High Capacity Zinc-Ion Battery System. *Chem. Mater.*, 27(10):3609–3620, May 2015. ISSN 0897-4756. doi: 10.1021/cm504717p.

[15] H Jamil, M Khaleeq-ur-Rahman, I M Dildar, and Saima Shaukat. Structural and optical properties of manganese oxide thin films deposited by pulsed laser deposition at different substrate temperatures. *Laser Phys.*, 27(9):096101, September 2017. ISSN 1054-660X, 1555-6611. doi: 10.1088/1555-6611/aa7cc8.

[16] Dongfang Yang. Pulsed laser deposition of manganese oxide thin films for supercapacitor applications. *Journal of Power Sources*, 196(20):8843–8849, October 2011. ISSN 03787753. doi: 10.1016/j.jpowsour.2011.06.045.

[17] Dongfang Yang. Pulsed laser deposition of cobalt-doped manganese oxide thin films

for supercapacitor applications. *Journal of Power Sources*, 198:416–422, January 2012. ISSN 03787753. doi: 10.1016/j.jpowsour.2011.10.008.

[18] Dongfang Yang. Pulsed laser deposition of vanadium-doped manganese oxide thin films for supercapacitor applications. *Journal of Power Sources*, 228:89–96, April 2013. ISSN 03787753. doi: 10.1016/j.jpowsour.2012.11.067.

[19] Zhiqiang Wang, Dongfang Yang, and Tsun-Kong Sham. Effect of oxidation state of manganese in manganese oxide thin films on their capacitance performances. *Surface Science*, 676:71–76, October 2018. ISSN 00396028. doi: 10.1016/j.susc.2017.12.011.

[20] Lauren M. Garten, Praneetha Selvarasu, John Perkins, David Ginley, and Andriy Zakutayev. Phase formation of manganese oxide thin films using pulsed laser deposition. *Mater. Adv.*, 2(1):303–309, 2021. ISSN 2633-5409. doi: 10.1039/D0MA00417K.

[21] S. Isber, E. Majdalani, M. Tabbal, T. Christidis, K. Zahraman, and B. Nsouli. Study of manganese oxide thin films grown by pulsed laser deposition. *Thin Solid Films*, 517(5):1592–1595, January 2009. ISSN 00406090. doi: 10.1016/j.tsf.2008.09.097.

[22] Hui Xia, Yunhai Wan, Feng Yan, and Li Lu. Manganese oxide thin films prepared by pulsed laser deposition for thin film microbatteries. *Materials Chemistry and Physics*, 143(2):720–727, January 2014. ISSN 02540584. doi: 10.1016/j.matchemphys.2013.10.005.

[23] M. Abi-Akl, M. Tabbal, and W. Kassem. Crystalline phase control and growth selectivity of β-MnO2 thin films by remote plasma assisted pulsed laser deposition. *Thin Solid Films*, 612:450–455, August 2016. ISSN 00406090. doi: 10.1016/j.tsf.2016.06.034.

[24] Debasis Nayak, Sudipto Ghosh, and Venimadhav Adyam. Thin film manganese oxide polymorphs as anode for sodium-ion batteries: An electrochemical and DFT based study. *Materials Chemistry and Physics*, 217:82–89, September 2018. ISSN 02540584. doi: 10.1016/j.matchemphys.2018.06.065.

[25] Malek Tabbal, Maya Abi-Akl, Samih Isber, Elisar Majdalani, and Theodore Christidis. Synthesis of nano-grained MnO 2 thin films by laser ablation. In Michel Meunier, Andrew S. Holmes, Hiroyuki Niino, and Bo Gu, editors, *SPIE LASE: Lasers and Applications in Science and Engineering*, page 720104, San Jose, CA, February 2009. doi: 10.1117/12.808967.

[26] Paul F. Ndione, Erin L. Ratcliff, Suhash R. Dey, Emily L. Warren, Haowei Peng, Aaron M. Holder, Stephan Lany, Brian P. Gorman, Mowafak M. Al-Jassim, Todd G.

Deutsch, Andriy Zakutayev, and David S. Ginley. High-Throughput Experimental Study of Wurtzite Mn $_{1-x}$ Zn $_x$ O Alloys for Water Splitting Applications. *ACS Omega*, 4(4):7436–7447, April 2019. ISSN 2470-1343, 2470-1343. doi: 10.1021/acsomega.8b03347.

[27] Yanqing Xin, Haijun Cao, Changqing Liu, Jian Chen, Ping Liu, Yingbo Lu, and Z.C. Ling. A systematic spectroscopic study of laboratory synthesized manganese oxides relevant to Mars. *Journal of Raman Spectroscopy*, August 2021. doi: 10.1002/jrs.6231.

[28] Simone Bernardini, Fabio Bellatreccia, Annalaura Casanova Municchia, Giancarlo Della Ventura, and Armida Sodo. Raman spectra of natural manganese oxides. *J Raman Spectrosc*, page jrs.5583, March 2019. ISSN 0377-0486, 1097-4555. doi: 10.1002/jrs.5583.

[29] N. N. Greenwood and A. Earnshaw. *Chemistry of the Elements*. Butterworth-Heinemann, Oxford ; Boston, 2nd ed edition, 1997. ISBN 978-0-7506-3365-9.

[30] A. F. Wells. *Structural Inorganic Chemistry*. Clarendon Press, Oxford, 4th edition, 1975. ISBN 978-0-19-855354-0.

[31] C.M Julien, M Massot, and C Poinsignon. Lattice vibrations of manganese oxides. *Spectrochimica Acta Part A: Molecular and Biomolecular Spectroscopy*, 60(3):689–700, February 2004. ISSN 13861425. doi: 10.1016/S1386-1425(03)00279-8.

[32] Henri Ailas. Manganese(ii) oxide, 2018. URL `https://wiki.aalto.fi/display/SSC/MnO`. URL: https://wiki.aalto.fi/display/SSC/MnO.

[33] Jeffrey E. Post, David A. McKeown, and Peter J. Heaney. Raman spectroscopy study of manganese oxides: Tunnel structures. *American Mineralogist*, 105(8):1175–1190, August 2020. ISSN 0003-004X, 1945-3027. doi: 10.2138/am-2020-7390.

[34] Marie-Claude Bernard, Anne Hugot-LeGoff, BichVu Thi, and Susanna Cordoba de Torresi. Electrochromic Reactions in Manganese Oxides. *J. Electrochem. Soc.*, 140(11):6, 1993.

[35] C M Julien and M Massot. Raman spectroscopic studies of lithium manganates with spinel structure. *J. Phys.: Condens. Matter*, 15(19):3151–3162, May 2003. ISSN 0953-8984, 1361-648X. doi: 10.1088/0953-8984/15/19/315.

[36] Zhi-gang Wei, Jia-hong Yan, Yang Wu, and Yue Liu. Importance of Metal Cations and Water for Stability of MnO $_2$ Crystals. *Chinese Journal of Chemical Physics*, 28

(6):711–715, December 2015. ISSN 1674-0068, 2327-2244. doi: 10.1063/1674-0068/ 28/cjcp1504068.

[37] Tao Gao, Helmer Fjellvåg, and Poul Norby. A comparison study on Raman scattering properties of α- and β-MnO2. *Analytica Chimica Acta*, 648(2):235–239, August 2009. ISSN 00032670. doi: 10.1016/j.aca.2009.06.059.

[38] Florina Buciuman, Florin Patcas, Radu Craciun, and Dietrich R. T. Zahn. Vibrational spectroscopy of bulk and supported manganese oxides. *Phys. Chem. Chem. Phys.*, 1:185–190, 1999. doi: 10.1039/A807821A. URL `http://dx.doi.org/10. 1039/A807821A`.

[39] Ouassim Ghodbane, Jean-Louis Pascal, Bernard Fraisse, and Frédéric Favier. Structural in Situ Study of the Thermal Behavior of Manganese Dioxide Materials: Toward Selected Electrode Materials for Supercapacitors. *ACS Appl. Mater. Interfaces*, 2(12): 3493–3505, December 2010. ISSN 1944-8244, 1944-8252. doi: 10.1021/am100669k.

[40] Reiner Korthauer, editor. *Lithium-Ion Batteries: Basics and Applications*. Springer Berlin Heidelberg, Berlin, Heidelberg, 2018. ISBN 978-3-662-53069-6 978-3-662-53071-9. doi: 10.1007/978-3-662-53071-9.

[41] Arumugam Manthiram. An Outlook on Lithium Ion Battery Technology. *ACS Cent. Sci.*, 3(10):1063–1069, October 2017. ISSN 2374-7943, 2374-7951. doi: 10. 1021/acscentsci.7b00288.

[42] Jurgen Garche, Chris Dyer, Patrick T Moseley, Zempachi Ogumi, David AJ Rand, and Bruno Scrosati. *Encyclopedia of electrochemical power sources*. Newnes, 2013.

[43] Dinesh Selvakumaran, Anqiang Pan, Shuquan Liang, and Guozhong Cao. A review on recent developments and challenges of cathode materials for rechargeable aqueous Zn-ion batteries. *J. Mater. Chem. A*, 7(31):18209–18236, 2019. ISSN 2050-7488, 2050-7496. doi: 10.1039/C9TA05053A.

[44] Chengjun Xu, Baohua Li, Hongda Du, and Feiyu Kang. Energetic Zinc Ion Chemistry: The Rechargeable Zinc Ion Battery. *Angew. Chem. Int. Ed.*, 51(4):933–935, January 2012. ISSN 14337851. doi: 10.1002/anie.201106307.

[45] G.Girish Kumar and S. Sampath. Electrochemical characterization of poly(vinylidenefluoride)-zinc triflate gel polymer electrolyte and its application in solid-state zinc batteries. *Solid State Ionics*, 160(3):289–300, 2003. ISSN 0167-2738. doi: 10.1016/S0167-2738(03)00209-1.

[46] Kexing Cai, Shao-hua Luo, Jie Feng, Jiachen Wang, Yang Zhan, Qing Wang, Yahui

Zhang, and Xin Liu. Recent advances on spinel zinc manganate cathode materials for zinc-ion batteries. *The Chemical Record*, 22(1):e202100169, 2022. doi: https://doi.org/10.1002/tcr.202100169. URL `https://onlinelibrary.wiley.com/doi/abs/10.1002/tcr.202100169`.

[47] Carlo S Casari and Andrea Li Li Bassi. PULSED LASER DEPOSITION OF NANOSTRUCTURED OXIDES: FROM CLUSTERS TO FUNCTIONAL FILMS. page 36.

[48] Robert Eason, editor. *Pulsed Laser Deposition of Thin Films: Applications-Led Growth of Functional Materials*. Wiley-Interscience, Hoboken, N.J, 2007. ISBN 978-0-471-44709-2.

[49] Andrea Pazzaglia. Produzione e caratterizzazione di bersagli multistrato per l'accelerazione di ioni mediante laser superintensi. Master's thesis, School of Industrial and Information Engineering, Politecnico di Milano, 2016.

[50] Angela De Bonis and Roberto Teghil. Ultra-Short Pulsed Laser Deposition of Oxides, Borides and Carbides of Transition Elements. *Coatings*, 10(5):501, May 2020. ISSN 2079-6412. doi: 10.3390/coatings10050501.

[51] Cristina Mancarella. Development of plasmonic gold nanostructures with tunable optical and electrical properties. Master's thesis, School of Industrial and Information Engineering, Politecnico di Milano, 2019.

[52] P. R. Willmott and J. R. Huber. Pulsed laser vaporization and deposition. *Rev. Mod. Phys.*, 72(1):315–328, January 2000. ISSN 0034-6861, 1539-0756. doi: 10.1103/RevModPhys.72.315.

[53] Marco Olivieri. Synthesis and Characterization of Zinc Manganite Thin Films for Zinc-Ion Battery Applications. Master's thesis, School of Industrial and Information Engineering, Politecnico di Milano, 2022.

[54] Beatrice Roberta Bricchi. *Engineering of Titanium Oxide and Nitride Nanostructures for Plasmonic Applications*. PhD thesis, School of Industrial and Information Engineering, Politecnico di Milano, 2020.

[55] C Richard Brundle and Charles A Evans. *Encyclopedia of Materials Characterization*. . ISBN 0-7506-9168-9. Chapter 2.2 "SEM - Scanning Electron Microscopy".

[56] Samapti Kundu. Synthesis and characterizations of some nanocrystalline metal oxide semiconductors and composites with different morphologies. Master's thesis, Department of physics, University of Burdwan, West Bengal-713104, 2018.

[57] Winson C. H. Kuo, Martha Briceno, and Dogan Ozkaya. FINAL ANALYSIS: *Characterisation of Catalysts Using Secondary and Backscattered Electron In-lens Detectors*. *platin met rev*, 58(2):106–110, April 2014. ISSN 00321400, 14710676. doi: 10.1595/147106714X680113.

[58] Oxford Instruments. Silicon drift detectors explained. page 28, 2012.

[59] C Richard Brundle and Charles A Evans. *Encyclopedia of Materials Characterization*. . ISBN 0-7506-9168-9. Chapter 3.1 "EDS - Energy-Dispersive X-Ray Spectroscopy".

[60] C Richard Brundle and Charles A Evans. *Encyclopedia of Materials Characterization*. . ISBN 0-7506-9168-9. Chapter 4.1 "XRD - X-RayDiffraction".

[61] Simona Garattoni. Synthesis of titanium nitride thin lms with tunable optical and electrical properties. page 146.

[62] Andrea Li Bassi. *X-ray and Light Scattering from Nanostructured Thin Films*. PhD thesis, University of Durham (UK), 2000.

[63] P Brüesch. *Phonons: theory and experiments II*. Springer. Chapter 3.

[64] Andrea Macrelli. Development of Paper-Based SERS Sensors for the Detection of Drugs. Master's thesis, School of Industrial and Information Engineering, Politecnico di Milano.

[65] Zhebo Chen, Huyen N. Dinh, and Eric Miller. *Photoelectrochemical Water Splitting: Standards, Experimental Methods, and Protocols*. SpringerBriefs in Energy. Springer, New York, 2013. ISBN 978-1-4614-8297-0. doi: 10.1007/978-1-4614-8298-7.

[66] Xuming Yang and Andrey L. Rogach. Electrochemical Techniques in Battery Research: A Tutorial for Nonelectrochemists. *Adv. Energy Mater.*, 9(25):1900747, July 2019. ISSN 1614-6832, 1614-6840. doi: 10.1002/aenm.201900747.

[67] Kosuke Izutsu. *Electrochemistry in Nonaqueous Solutions*. Wiley-VCH Verlag GmbH & Co. KGaA, Weinheim, FRG, February 2002. ISBN 978-3-527-30516-2 978-3-527-60065-6. doi: 10.1002/3527600655.

[68] Roberto Matarrese, Isabella Nova, Andrea Li Bassi, Carlo S. Casari, Valeria Russo, and Simonetta Palmas. Preparation and optimization of TiO2 photoanodes fabricated by pulsed laser deposition for photoelectrochemical water splitting. *Journal of Solid State Electrochemistry*, 21(11):3139–3154, November 2017. ISSN 1433-0768. doi: 10.1007/s10008-017-3639-7.

[69] P. Gondoni, P. Mazzolini, V. Russo, M. Diani, M. Amati, L. Gregoratti, V. De Renzi,

G.C. Gazzadi, J. Martí-Rujas, A. Li Bassi, and C.S. Casari. Tuning electrical properties of hierarchically assembled Al-doped ZnO nanoforests by room temperature Pulsed Laser Deposition. *Thin Solid Films*, 594:12–17, 2015. ISSN 0040-6090. doi: 10.1016/j.tsf.2015.09.066.

[70] A. Bailini, F. Di Fonzo, M. Fusi, C.S. Casari, A. Li Bassi, V. Russo, A. Baserga, and C.E. Bottani. Pulsed laser deposition of tungsten and tungsten oxide thin films with tailored structure at the nano- and mesoscale. *Applied Surface Science*, 253(19): 8130–8135, 2007. ISSN 0169-4332. doi: 10.1016/j.apsusc.2007.02.145.

[71] Beatrice R. Bricchi, Luca Mascaretti, Simona Garattoni, Matteo Mazza, Matteo Ghidelli, Alberto Naldoni, and Andrea Li Bassi. Nanoporous Titanium (Oxy)nitride Films as Broadband Solar Absorbers. *ACS Appl. Mater. Interfaces*, 14(16):18453–18463, April 2022. ISSN 1944-8244. doi: 10.1021/acsami.2c01185.

[72] F. Di Fonzo, C. S. Casari, V. Russo, M. F. Brunella, A. Li Bassi, and C. E. Bottani. Hierarchically organized nanostructured TiO2 for photocatalysis applications. *Nanotechnology*, 20(1):015604, December 2008. ISSN 0957-4484. doi: 10.1088/0957-4484/20/1/015604.

[73] Rudresh Ghosh, M. Kyle Brennaman, Tim Uher, Myoung-Ryul Ok, Edward T. Samulski, L.E. McNeil, Thomas J. Meyer, and Rene Lopez. Nanoforest Nb2O5 Photoanodes for Dye-Sensitized Solar Cells by Pulsed Laser Deposition. *ACS Appl. Mater. Interfaces*, 3(10):3929–3935, October 2011. ISSN 1944-8244. doi: 10.1021/am200805x.

[74] WWW-MINCRYST. Crystallographic and crystallochemical database for minerals and their structural analogues, . URL `http://database.iem.ac.ru/mincryst/s_carta.php?1876`. Card n°1876.

[75] AMCSD. American mineralogist crystal structure database, . URL `http://rruff.geo.arizona.edu/AMS/amcsd.php`. AMCSD database code 0001302 (K-birnessite).

[76] J. Tauc, R. Grigorovici, and A. Vancu. Optical Properties and Electronic Structure of Amorphous Germanium. *physica status solidi (b)*, 15(2):627–637, 1966. ISSN 1521-3951. doi: 10.1002/pssb.19660150224.

[77] WWW-MINCRYST. Crystallographic and crystallochemical database for minerals and their structural analogues, . URL `http://database.iem.ac.ru/mincryst/s_carta.php?5956`. Card n°5956.

[78] AMCSD. American mineralogist crystal structure database, . URL `http://rruff.`

`geo.arizona.edu/AMS/amcsd.php`. AMCSD database code 0016237 (cryptomelane-hollandite).

[79] O. Nilsen, S. Foss, H. Fjellvåg, and A. Kjekshus. Effect of substrate on the characteristics of manganese(IV) oxide thin films prepared by atomic layer deposition. *Thin Solid Films*, 468(1-2):65–74, December 2004. ISSN 00406090. doi: 10.1016/j.tsf.2004.04.055.

[80] Francesca Rossi, Emanuele Marini, Marco Boniardi, Andrea Casaroli, Andrea Li Bassi, Andrea Macrelli, Claudio Mele, and Benedetto Bozzini. What Happens to MnO $_2$ When It Comes in Contact with Zn $^{2+}$? An Electrochemical Study in Aid of Zn/MnO $_2$ -Based Rechargeable Batteries. *Energy Tech*, 10(8):2200084, August 2022. ISSN 2194-4288, 2194-4296. doi: 10.1002/ente.202200084.

[81] Jie Yang, Jianyun Cao, Yudong Peng, Wenji Yang, Suelen Barg, Zhu Liu, Ian A. Kinloch, Mark A. Bissett, and Robert A. W. Dryfe. Unravelling the Mechanism of Rechargeable Aqueous Zn–MnO2 Batteries: Implementation of Charging Process by Electrodeposition of MnO2. *ChemSusChem*, 13(16):4103–4110, 2020. ISSN 1864-564X. doi: 10.1002/cssc.202001216.

[82] Chang-Hoon Kim, Zentaro Akase, Lichun Zhang, Arthur H. Heuer, Aron E. Newman, and Paula J. Hughes. The structure and ordering of ϵ-MnO2. *Journal of Solid State Chemistry*, 179(3):753–774, March 2006. ISSN 0022-4596. doi: 10.1016/j.jssc.2005.11.042.

[83] Roberto Cestaro, Peter Schweizer, Laetitia Philippe, Xavier Maeder, and Albert Serrà. Phase and microstructure control of electrodeposited Manganese Oxide with enhanced optical properties. *Applied Surface Science*, 580:152289, April 2022. ISSN 0169-4332. doi: 10.1016/j.apsusc.2021.152289.

[84] Jeffrey E. Post, David A. McKeown, and Peter J. Heaney. Raman spectroscopy study of manganese oxides: Layer structures. *American Mineralogist*, 106(3):351–366, March 2021. ISSN 0003-004X. doi: 10.2138/am-2021-7666.

List of Figures

List of Tables

Acknowledgements

In questi mesi ho avuto la fortuna di lavorare ad un progetto al quale mai avrei creduto di poter prendere parte. Per questo devo ringraziare il Professor Li Bassi; ricorderò sempre la felicità del momento in cui mi arrivò la sua mail con la proposta di tesi. Grazie anche per avermi seguito e consigliato durante il percorso e per essere sempre stato disponibile nei momenti di bisogno. Un enorme grazie anche al mio tutor, Andrea Macrelli, per avermi guidato durante questi mesi e per avermi insegnato davvero un sacco di cose. Grazie infinite per la tua pazienza e per avermi aiutato a superare ogni difficoltà sia in laboratorio che durante la stesura della tesi. Ci tengo anche a ringraziare tutti coloro che hanno contribuito ad arricchire questo progetto con consigli e suggerimenti. In particolare, vorrei ringraziare il Professor Bozzini per le sue "dritte" sulla parte relativa allo studio dell'elettrochimica; il Professor Bussetti e tutto lo staff del SoLINano per avermi accolto e assistito nelle misure elettrochimiche; il Professor Dellasega per i suoi preziosi consigli sul SEM (e non) e per aver sempre visto del gran potenziale nel mio progetto; la Professoressa Russo per i suoi consigli riguardo alla Spectroscopia Raman e Alessio Lamperti del CNR per avermi ospitato nel suo laboratorio per le misure XRD. Ringrazio infine tutti i membri del NanoLab che non mi hanno mai fatto sentire di troppo e hanno contribuito a rendere ancora più bella questa esperienza.

Grazie ai miei genitori, che nonostante non fossero pienamente d'accordo, mi hanno sempre permesso di studiare senza dover rinunciare a nulla. Un grazie va anche a mio fratello Armando che mi ha assistito nei momenti di blackout, e a mio fratello Alessandro al quale ho rubato i pennarelli per fare gli schemi durante questi cinque anni.

Grazie a tutti coloro che anno condiviso con me questi cinque anni, perchè solo voi sapete cosa vuol dire. Grazie ai miei "amici di Bergamo" con i quali ho condiviso innumerevoli viaggi (o meglio, avventure) in treno e non solo. Grazie ai miei amici del "Polipranzo" con i quali ho condiviso cibo, risate, ansie e preoccupazioni.

Infine, un immenso grazie al mio fidanzato, Luca, che non ha mai smesso di credere in me ed è sempre rimasto al mio fianco anche nei momenti di maggior difficoltà. Mi hai sempre spinto a non mollare e a superare i miei limiti, per questo te ne sarò per sempre grata.